NANOCONSTRUCTS FOR TARGETING, IMAGING, AND PHOTOTHERMAL THERAPY OF CANCER

A Dissertation

Presented to the Faculty of the Graduate School

of Cornell University

In Partial Fulfillment of the Requirements for the Degree of

Doctor of Philosophy

by

Dickson Kiprono Kirui

August 2011

NANOCONSTRUCTS FOR THE TARGETING, IMAGING, AND PHOTOTHERMAL THERAPY OF CANCER

Dickson Kiprono Kirui, Ph.D.

Cornell University 2011

Nanomaterials are becoming attractive for a variety of medical applications with over 250 nanotechnology-based products in U.S. pharmaceutical pipelines. Nanoparticle-based targeting has the potential to improve upon the limitations of conventional pharmaceuticals and increase the efficacy of drug delivery, therapy and imaging systems while reducing the side effects to healthy tissues. Due to the unique properties at nanometer scale, metallic nanomaterials have increasingly garnered interest as potential agents for selective molecular targeting, imaging, therapy, drug delivery and therapeutic applications. Research efforts that initially focused on rational design of passively delivered therapeutic system have recently progressed to the development of "second-generation" systems that can actively seek out cell markers and specific organs or cells based on over-expressed surface markers such as antigens expressed on cancer cells. This thesis reports on the development of second-generation targeted metallic-based therapy and diagnostic agents for potential heat-induced therapy and for magnetic resonance-based (MR) imaging.

Here, we have developed selectively targeted metallic nanostructures that are conjugated to antibodies and have demonstrated their uses in molecular targeting, multimodal imaging, and in thermotherapy (photothermal therapy) applications both using *in vitro* as well as in animal

models. Initially, we have synthesized and designed iron oxide-gold hybrid nanoparticles (HNPs) to make stabile water-soluble particles with suitable end functional groups that allow attachment of targeting antibodies. Next, the HNPs have been tested for cytotoxicity using targeted colorectal cancer cell lines. Further experiments were used to test the potential uses of these hybrid nanoparticles for dual functions for photothermal therapy as well as for MRI.

On the basis of promising *in vitro* results, HNPs were tested in xenograft mice to illuminate the ability to achieve localized particle delivery following systemic injection. Particle localization was visualized by optimal fluorescence imaging and corroborated by non-invasive MR imaging and by histological tissue staining. After local particle delivery, effective photothermal therapy application has been demonstrated where tumor damage was observed posttreatment. Gold nanorods have become attractive for deep tissue *in vivo* photothermal therapy applications. We have demonstrated a novel method of coating with polyacrylate, resulting in stabile water-soluble nanorods. Further, the heating capacity of nanorods solution and selective *in vitro* photothermal therapy applications has been demonstrated.

BIOGRAPHICAL SKETCH

Dickson Kiprono Kirui was born in Kericho, Kenya, on October 16, 1980 as a first born to a family of four. He completed his elementary school as well as high school education back in Kenya before coming to the United States to begin his undergraduate studies. Although he was initially matriculated to Texas Southern University in Houston, TX, he immediately transferred to Millersville University of Pennsylvania to be close to his family where he earned Bachelor's of Science in Chemistry. During his senior year at Millersville, he participated in an internship research program at the Cornell Center of Material research (CCMR) in the summer of 2005 which he thoroughly enjoyed and later became a decisive factor in choosing Cornell for a graduate school program. In the fall of 2006, he joined Materials Science of engineering program at Cornell University with the goal of pursuing graduate studies in biomaterials. After one year, he transferred to Biomedical engineering which he found to be a better match for his research and career goals.

Shortly after joining Professor Carl Batt's laboratory in the Food science Department (current lab), he became more interested in pursuing his graduate studies in the interface of nanotechnology and biotechnology. He learned more about nanotechnology that included initially working in the microfabrication facility to design features on silicon chips with the mentorship of a senior graduate student (Parijat Bhatnagar). At the same time, he became more acquainted with molecular biology taking place in the lab which is developed more research interest. Eventually, he ended pursuing a research project in the rational design of nanostructured materials with the goal of using them for biomedical applications with the particular focus for therapy and imaging applications.

His near-term goal is to gain experience in translational research by postdoctoral training to prepare myself for a career in a clinically-relevant field, in industry or in a research institution. In the longer term goal, after obtaining requisite experience on medical industry, he would like to be involved (in some way) in improving medical technology particularly in his native country (Kenya) and even Africa in general.

ACKNOWLEDGMENTS

I feel very fortunate to be where I am today (particularly reminiscing on the journey that has been travelled), and there are people who have supported and have paved my journey that I would like to acknowledge. First, I would like to start by thanking my late Mother whose inspiration and sense of hard work is continue to be a driving force and is embodied in my education as well as in my daily life. I also thank my Aunt, Esther Yegon, who has been constant source of love and encouragement that have sustained me through most difficult hurdles in life. The rest of the family, my Dad (David Yegon), siblings (Irene, Monica and Leonard), and the entire of extended family have also been a powerful force and to them all I am very grateful. For an invaluable mentor, I would like to thank Professor Edward Rajaseélan for his wise counsel in pertaining educational goals as well as his encouragement and believe in my capabilities.

I am greatly indebted to my Advisor, Professor Carl Batt, under whose direction I acquired foundational skills as a scientist and gained deep appreciation for emerging field in life science and its multidisciplinary field in nanomedicine. In his Laboratory, I developed the skills for scientific query, problem solving skills, and multidisciplinary skill sets in biotechnology and nanotechnology, and the ability to work collaboratively – all these skills will enable me to pursue a career in translational medicine. Most importantly, I thank him for his patience, for believing in me and for providing guidance especially during my nascent years in graduate school when I appeared overwhelmed and hardly possessed what it takes to obtain a Ph.D. My Thesis committee members, Professors Lara Estroff and Gerald Feigenson, have been invaluable advisors whom I have greatly benefited from their counsel and guidance in my research efforts and in making career choices. I am very grateful for both of them.

Working in the Batt Research Group has been a very enjoyable experience and where I have built great working relationships with my fellow colleagues. They have been friendly and willing to share scientific expertise in various multidisciplinary areas and even share some light moments with jokes, etc. This has made acquiring various multidisciplinary skill sets possible. First, I am greatly thankful to Pari Bhatnagar for taking me under his wing when I first joined the lab. He worked hard to expose me to many experiences not only on the lab bench but also taught me how to navigate through the various facilities and equipment trainings at Cornell. Secondly, I thank Kyle Anderson for his mentorship which was instrumental in acquiring biochemistry background and learning the various protein expression and purification techniques. He was always willing to share his experiences, mentor and train on new skills and for that I am very grateful.

During my time in the Lab, I had countless opportunities to work in teams. Besides Carl, Diego Rey was very good in organizing and getting others involved in team projects. I am thankful that he worked hard to establish contacts and collaborations with preeminent clinicians, such as Alexi Tei and Richard Lee, from Weill Cornell Medical College, whom I have greatly benefited from working them and through their financial support. Diego also played a role in establishing collaboration with Prof Moonsoo's lab with which I have used their Animal protocol in my research. I am also grateful for Cameron Bardliving's friendship, his willingness to share in bad and humorous times and also our shared scientific experiences. I have also worked with Adam Lowe and I am grateful for sharing his scientific expertise and making the lab an enjoyable place to work.

I would like to also thank Andrew Melnychenko for his prompt response and the diligence he puts in placing our orders for laboratory supplies. He made life a little easier for all

use. In addition, I cannot forget the unceasing ways Andy made me laugh, narrating his weekend adventures in ways that helped take the edge off and made the day a little bit brighter and less groomer days especially when experiments were not working.

Through my graduate studies I have fortunate to collaborate with other scientists and have contribution of my scientist success. First, I would like to thank Professor Moonsoo Jin for his guidance and for including me onto his UICAC Animal protocol which enabled me to gain valuable experience with animal experimentation. Without him, it would have been difficult to perform *in vivo* experiments. I am also grateful for the assistance of Professor Yi Wang, Department of Radiology at Weill College of Cornell University, for his assistance with MR animal imaging.

TABLE OF CONTENTS

LIST OF FIGURES

TABLE OF CONTENTS

Chapter 1

Introduction

1.1. Introduction

When the size of a material is reduced to the nanometer length scale (which is the length scale of the electronic motion that determines the material's properties), its electronic and chemical properties change tremendously. In metals, the larger surface-to-volume ratio that arise from size reduction makes the surface properties more dominant, giving rise to new nanoparticle properties. In semiconductor nanoparticles, the property change results from quantum confinement of the electronic motion [1]. In noble metals the coherent collective oscillation of electrons in the conduction band induces large surface electric fields which significantly enhance the radiative properties of gold and silver nanoparticles when they interact with resonant electromagnetic radiation [2]. This makes the nanoparticles' absorption crossection several orders of magnitude stronger than the strongest absorbing molecules [3] and the scattered light becomes orders of magnitude more intense than the fluorescence of organic dyes [4]. For transition metals such as iron oxide, the reduction of their size to nanometer scale drastically changes to material properties, resulting in superparamagnetic behavior. Nanomaterials with these unique properties have found myriad of potential applications such as uses in catalysis owing to the high surface-to-volume ratios [5], uses for biochemical sensing [6], and in making medical therapeutics [7]. This thesis will focus on the various biomedical applications specifically as it pertains to the uses of gold and iron oxide nanoparticles for imaging and therapy applications.

Since the seventeenth century metallic nanomaterials, although not well understood, have been used to decorate glass cathedrals windows giving rise to brilliant rose colors throughout Europe [8]. They were also used by ancient Chinese to color vases and other ornaments [9]. The first scientific preparation of nanoparticles is traced back to the nineteenth century where Faraday reported colloids of relatively monodispersed gold nanoparticles. In past

several decades there has been an exponential worldwide growth of activities in this field driven by the excitement of understanding new science, the invention of powerful investigative tools such as the electron microscope, and by the potential industrial applications and the resulting economic impact. Indeed, great research efforts have been devoted to the synthesis, characterization, and application of nanomaterials for various uses ranging from industrial-scale catalysis to the development of novel clinical medical technologies. In general, nanomaterials are classified into three groups which are: zero-dimensional materials (commonly referred to as nanoparticles), with variations in shape and diameter, one-dimensional materials, (e.g. nanorod and nanowire), and two-dimensional materials, (e.g. nanodisks, nanobelts, and films, nanosheets). The focus of this review will be on the one-dimensional materials, specifically on metallic nanoparticles (NPs) and their potential medical applications.

1.2. Noble Metallic Nanoparticles

Noble metals, particularly gold, have been considered to be mystical material for its supposed ancient medicinal value and for its ornamental values for centuries now [10]. "Red-gold" used to stain glass was known to medieval artisans to be "finely-divided" gold dispersed in plain glass [11]. In recent decades, nanoscale gold particles have generated great excitement due to the potential uses in medical diagnostics, as tracers, and other biological and biomedical applications. For instance, the intriguing colors and properties of gold NPs are derived from their unique chemical and electronic properties arising from the high surface-to-volume ratio and the separation in the electronic energy levels. These properties at the nanoscale, compared to their bulk counterparts, not only arise from the scaling factors but are also material-dependent properties that vary for different materials. In semiconductor NPs, these unique properties are

derived from the confinement electrons to smaller dimension to nanometer scale which is of the same order of magnitude as electron Bohr radius -which determines the material properties. Herein, several properties that make gold nanostructures unique for biomedical applications will be reviewed.

1.3. Radiactive properties

The intriguing optical properties of metal nanoparticles, as reflected by their intense color, are attributed to their unique interaction with incident visible light. In the presence of the oscillating electromagnetic field of light, the conduction band electrons of a metal nanoparticle undergo a collective coherent oscillation in resonance with the frequency of light, which is known as surface Plasmon resonance (SPR) [12]. This oscillation induces a charge separation between the free electrons and the ionic metal core, which exerts a restoring Coulomb force to make the electrons oscillate back and forth on the particle surface resulting in a dipole oscillation (see Figure **1-1**). The SPR oscillation induces a strong absorption of light, as seen on the UV–vis spectrum, which is the origin of the intense color in noble metal colloidal solution and was first explained by Mie theory [13]. Spherical gold, silver, and copper nanoparticles show a strong SPR band in the visible region while other metals such as iron oxide show broad and weak bands in the UV region [14, 15]. The origin of the red color of gold nanoparticles and surface plasmon resonance behavior of the spherical metal nanoparticles was first explained by Mie [13]. He solved Maxwell's equation for an electromagnetic light wave interaction with a small sphere. For nanoparticles much smaller than the wavelength (< 20 nm), only the dipole oscillation contributes significantly to the extinction cross section and thus Mie's theory reduced to the following equation:

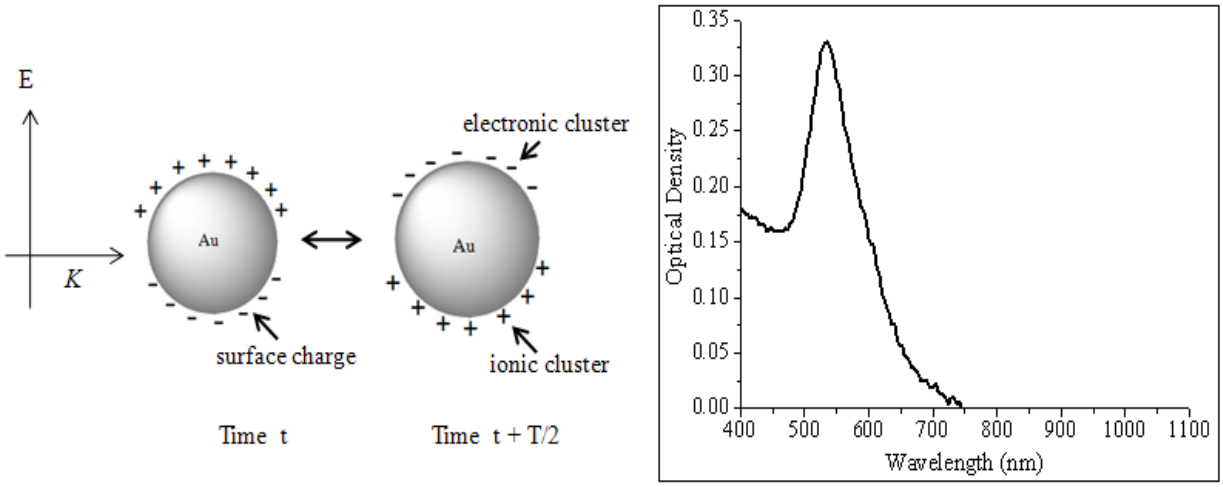

Figure 1-1: A schematic illustration of the interaction of polarized light with gold nanospheres to form electronic coherent surface Plasmon resonance (SPR) oscillation. The electric field (E) of incident light propagating along the *K* direction induces coherent collective oscillation of band electrons with respect to positively charged metallic core (ionic cluster). Gold nanospheres show one SPR band in the visible region [15].

$$\sigma_{ext}(\omega) = 9\frac{\omega}{c}\varepsilon_m^{3/2}V\frac{\varepsilon_2(\omega)}{[\varepsilon_1(\omega)+2\varepsilon_m]+\varepsilon_2(\omega)^2} \qquad \textbf{(1.1)}$$

where V is the particle volume, x is the angular frequency of the exciting light, c is the speed of light, and ε_m and $\varepsilon(\omega) = \varepsilon_1(\omega) + i\ \varepsilon_2(\omega)$ are the dielectric functions of the surrounding medium and the material itself respectively. The resonance condition is fulfilled when is $\varepsilon_1(\omega) = -2\ \varepsilon_m$ if ε_2 is small or weakly dependent on ω. But for larger nanoparticles, the light cannot polarize the nanoparticles homogeneously and retardation effects lead to the excitation of higher-order modes [16]. From equation (**1.1**), it can be seen that the peak intensity and the position absorption band is dependent on the size and shape of the metal nanoparticles as well as the dielectric constants of the metals and the medium surrounding the particles [17]. As the size increases, the absorption maximum is red shifted slightly (see Figure **1-2**). The bandwidth also changes when the size changes. The intriguing colors of noble metals, reflected in the UV-Vis absorption spectrum, are related to their size and shape [18]. For example gold nanospheres that

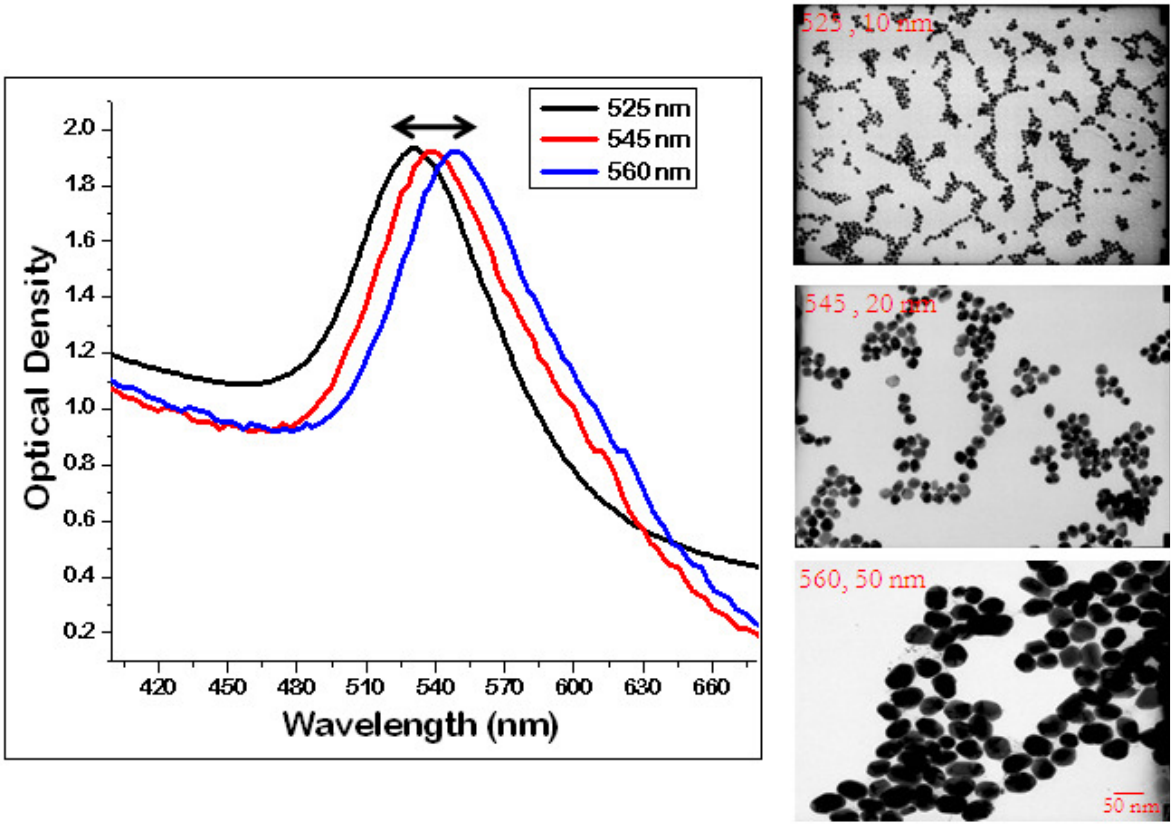

Figure 1-2: Surface Plasmon absorption spectra (left) and TEM (right) of gold nanospheres of different sizes. The surface Plasmon absorption is maximum is weakly dependent on particle size.

re

10 nm in diameter have a maximum absorbance at 520 nm and appear red in color whereas 50-nm gold NPs with absorbance at 560 nm appear blue in color. The fact that colloidal gold NPs present different shades of color that depends on the particle size and shape have not only created many aesthetical applications, but have more importantly generated great interest in applications where tunable optical properties are desirable.

Further, Link and El-Sayed [3] have shown that the peak bandwidth decreases with increasing size when the particles are less than 20 nm in diameter while bandwidth increases with increasing nanoparticle size for particles larger than 20 nm (Figure **1-3**, left). They also found that the absorption coefficient is linearly dependent on the volume of the nanoparticles

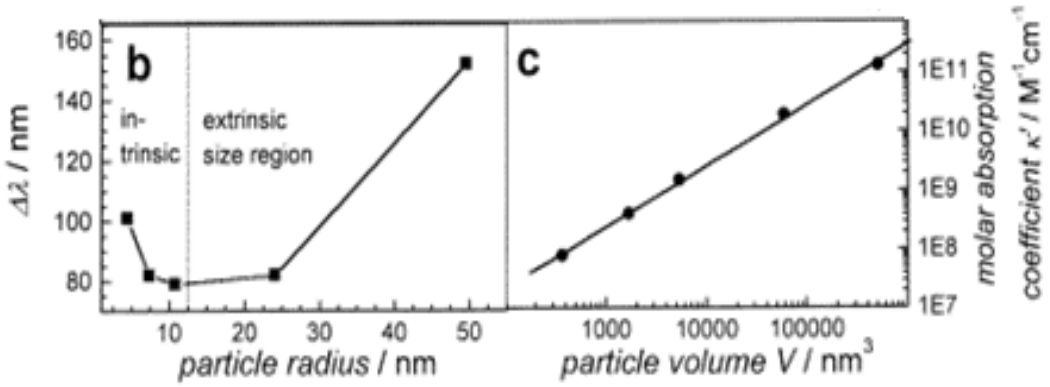

Figure 1-3: Left: the relationship of the absorption bandwidth with the size of the nanoparticles; Right: the relationship of the absorption coeffiecient with the size of the nanoparticles]. The bandwidth increases with decreasing nanoparticle radius in the intrinsic size region and also with increasing radius in the entrinsic size region as predicted by Mie theory. The extinction coefficients of these gold nanoparticles against their volume show a linear dependence [3].

which is in agreement with the Mie theory [13] . When the shape of the nanoparticles changes from nanosphere to nanorods, the surface plasmon absorption spectrum also changes. In the case of gold nanorods, electron oscillation can occur in one of the two directions depending on the polarization of incident light: the short and long axes. The excitation of the surface plasmon oscillation along the short axis induces an absorption band in the visible region at wavelength similar to that of gold nanospheres (referred to as transverse band) while excitation along the long axis induces a much stronger absorption band in the longer wavelength region (known as longitudinal band) (see Figure **1-4**). Figure **1-4** shows a typical absorption spectrum of nanorods. The transverse band is insensitive to the size of nanorods and the longitudinal band is red-shifted from the visible to near-infrared region with increasing aspect ratio (length/width). This optical behavior has been explained by Gans theory [19] which explains the optical properties of ellipsoid particles based on a dipole approximation. In

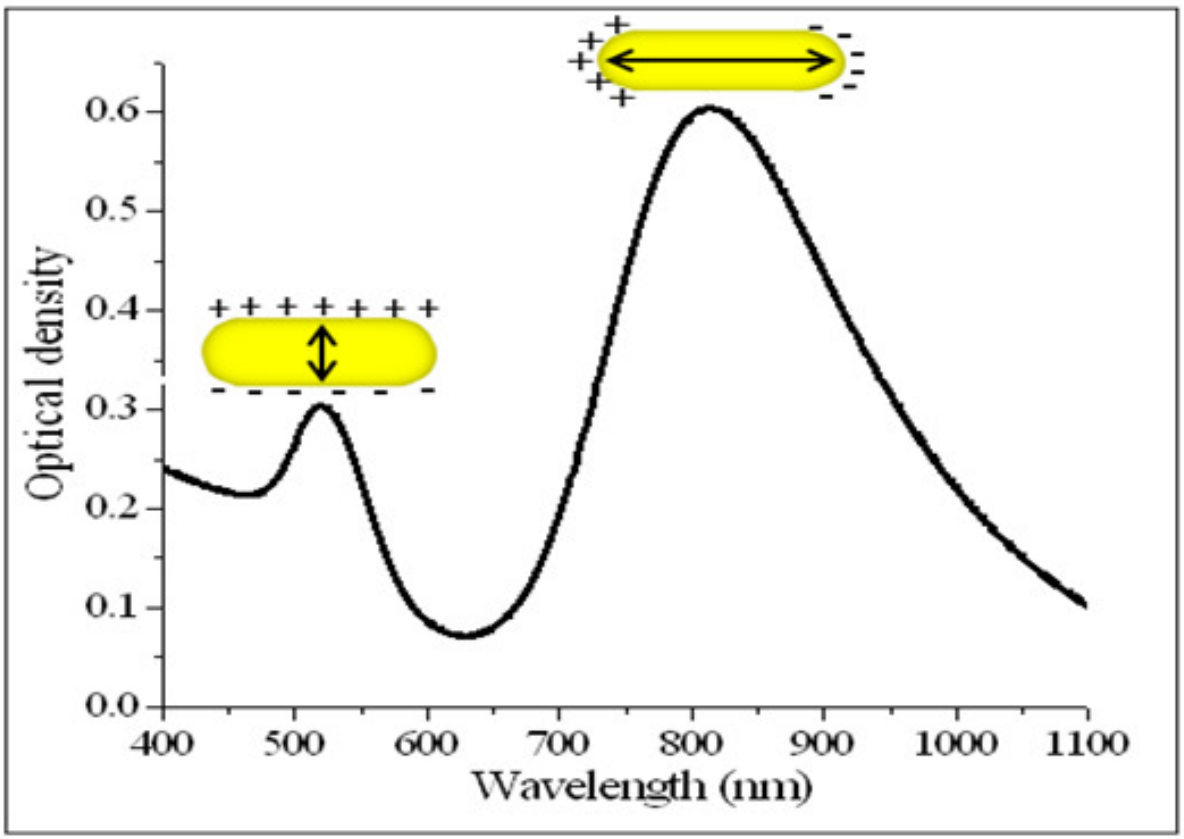

Figure 1-4: Typical surface plasmon absorption spectrum of gold nanorods. The strong long wavelength band in the near infrared region around 800 nm is due to the longitudinal oscillation of electrons while the weak short wavelength band in the visible region around 520 nm is due to the transverse electron oscillation.

aqueous solution, the SPR absorption maximum (λ_{max}) is linearly proportional to the aspect ratio (R) by the following relationship [20]:

$$\lambda\text{max} = 95R + 420 \qquad (\mathbf{1.2})$$

This provides a means of optically tuning gold nanorods by simply varying the aspect ratio of the particles. The ability to tune the absorption of nanorods is different from nanospheres for which the SPR only slightly red-shifts with increasing particles. Figure **1-5** shows how the absorption maximum of the nanorods shifts with varying aspect ratios. As the aspect ratio increases, the absorption maximum of the longitudinal band is red-shifted. The absorption difference of the

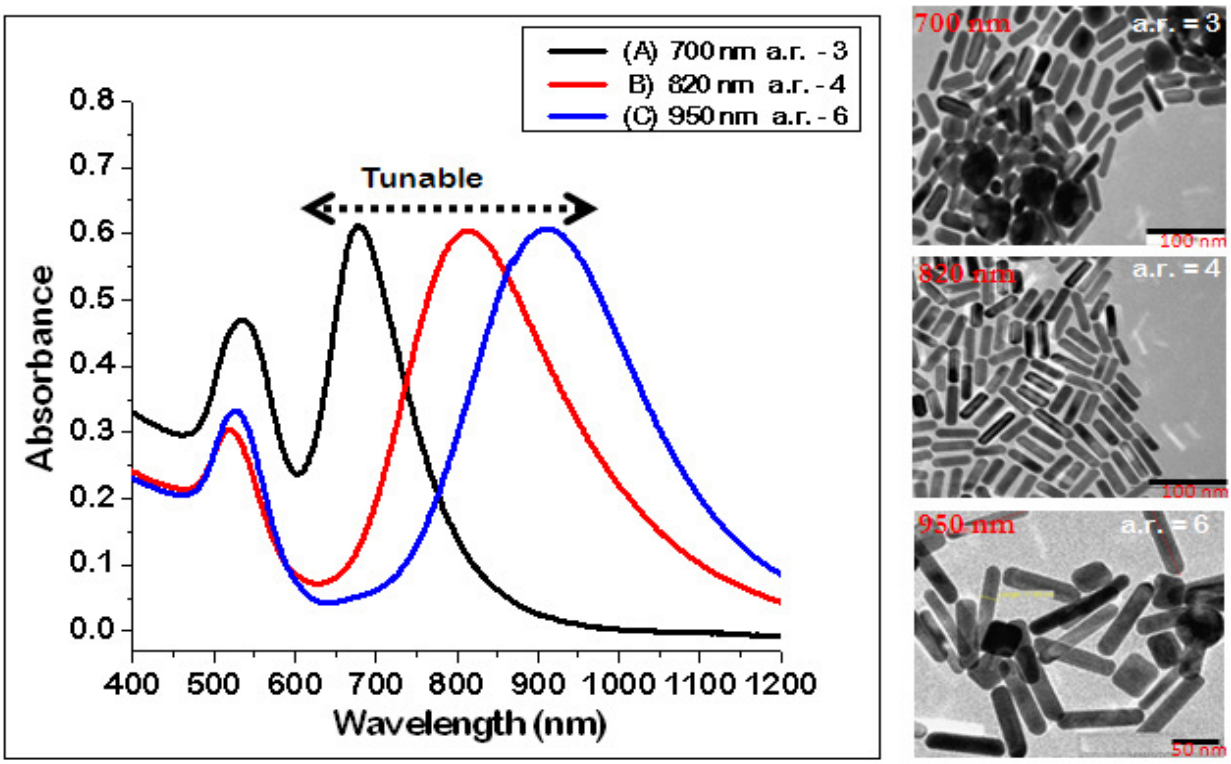

Figure 1-5: The absorption spectra of gold nanorods of different aspect ratios (left) and corresponding TEM images of the rods with aspect ratios (a.r.) at 3, 4 and 6.

longitudinal band causes the color difference of the nanorod solution. For short nanorods with the longitudinal maximum lower than 700 nm, the nanorods appear blue in color. When the longitudinal maximum is in the range 700-800 nm, the nanorod solution are gray-greenish in color while a solution with longitudinal band longer than 800 nm appear pink-brownish in color.

Biomedical medical application of Au nanostructures originate from their surface plasmon resonance (SPR) effect, a strong enhancement of absorption and scattering of light resonant with the SPR frequency, which has been utilized for photothermal ablation treatment and optical imaging. It has been reported that the strongly absorbed radiation is converted efficiently into heat on a picosecond time domain due to electron-phonon and phonon-phonon processes [21]. Thus, upon the laser irradiation at the surface plasmon absorption band, the nanoparticles absorb photon energy and then immediately transfer into heat energy. One of the

potential applications is to selectively cause a sharp increase on the local temperature in biomolecules, cells or tissues and therefore causing heat-induced damage of the surrounding materials or cells. This photothermal destruction can be used for disease treatment or cancer therapy. The ability to tune the SPR wavelength of Au nanorods, nanoshells and nanocages to the NIR region, which is commonly regarded as a 'clear window' for deep tissue light penetration, have provided additional impetus to the use of gold nanostructures for *in vivo* medical applications. In this thesis report, the use of gold nanorods will be explored as it relates to cancer therapy.

1.4. Magnetic Nanoparticles

In contrast to gold nanostructures with strong optical properties, transition metals such as iron, cobalt, gadolinium, and nickel have minimal absorption and SPR in the visible region but possess uniquely strong magnetic properties at the nanometer scale. Compared to their counterparts in bulk, oxides of these metals display superparamagnetic behavior, a phenomenon that stems from presence of single magnetic domain when particle size is reduced to the nanometer scale. In magnetic bulk materials such as ferromagnets and paramagnets, there exists multidomain structures that consist of regions of uniform magnetization separated by domain walls meant to minimizes the sum energy of external magnetic field (magnetostatic energy) and the energy of the domain walls (see Figure **1-6**). As the volume of magnetic particle decreases, the size of the domains and the width of the walls are reduced until the energy cost required to make a domain is greater than the corresponding reduction in magnetostatic energy. Consequently, the small magnetic nanoparticle is no longer divided into domains but instead exists in a single domain, which is referred to as superparamagnetism [22]. Ferromagnetic and superparamagnetic materials have shown potential for various applications because can be

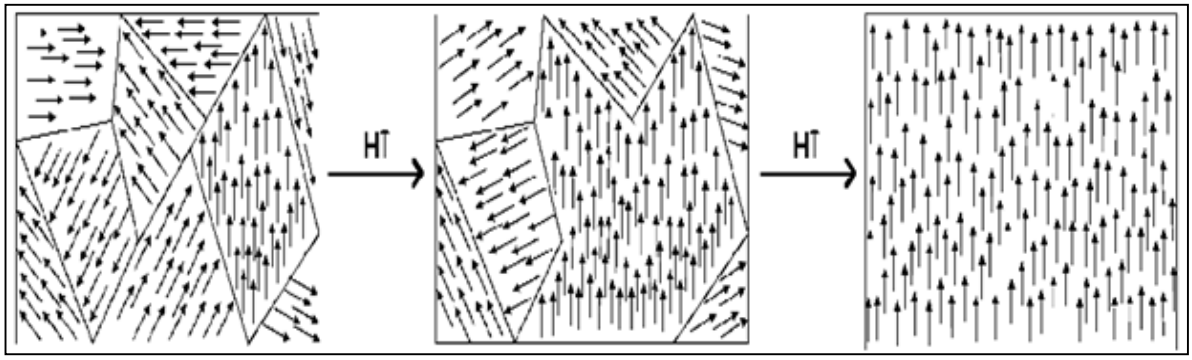

Figure 1-6: Schematic Representation of the reorientation of domain walls and alignment of magnetic moments under an externally applied magnetic field. (Wikimedia Commons)

magnetized in presence in an applied magnetic field. For ferromagnets, when an external field is applied the initially un-magnetized sample (M = 0 at H = 0), gradually becomes magnetized as applied field (H). This magnetization process is due to the motion and growth of the magnetic domains; areas with the same direction of the local magnetization (see Figure **1- 7 (a)**). When the sample is fully magnetized in the direction of M along H, a saturation point is reached, and magnetization curve will not retrace along the original dashed curved when the applied field (H) is reduced because the domain wall displacements are irreversible. Instead, a degree of magnetization is retained as domains are still aligned in the original direction of applied magnetic field and this is known as remnant magnetization (M_r) shown on Figure **1-7 (a)**. To reduce magnetization M back to zero (origin), a reverse field is required, known as coercive field or coercivity. Superparamagnetic materials are similar to paramagnets except that their single domain allows reversible wall displacements (see Figure **1-7 (b)**). When applied field (H) is reduced, the materials becomes fully demagnetized (magnetization, M, comes back to zero) without expending extra coercivity energy; materials that display this characteristic have no coercivity and known to be superparamagnetic. Superparamagnetism is a size-dependent phenomenon. As particle size decreases the coercivity decreases to reach a minimum at a

threshold particle size (typical values are 15 and 35 nm for iron and cobalt metallic particles) which describes the transformation from multi domain structure to single domain nature [23].

As consequent of this unique property, superparamagnetic nanoparticles have garnered interest for various applications because they have no remnant magnetic field once an external magnetic field is removed. While cobalt, manganese, and nickel nanoparticles exhibit good superparamagnetic properties, their use for bioapplication has been limited because they have shown poor biocompatibility. The superparamagnetic iron oxide nanoparticles (SPIONs) composed of iron oxides; magnetite (Fe_3O_4) and maghemite (γ-Fe_2O_3) are the commonly used magnetic materials because of their low toxicity and the advantage that our body is designed to process excess iron. Hemoglobin in our blood, for example, is an iron complex and is magnetic in nature. Biocompatible SPIONs have been widely used for *in vivo* biomedical applications

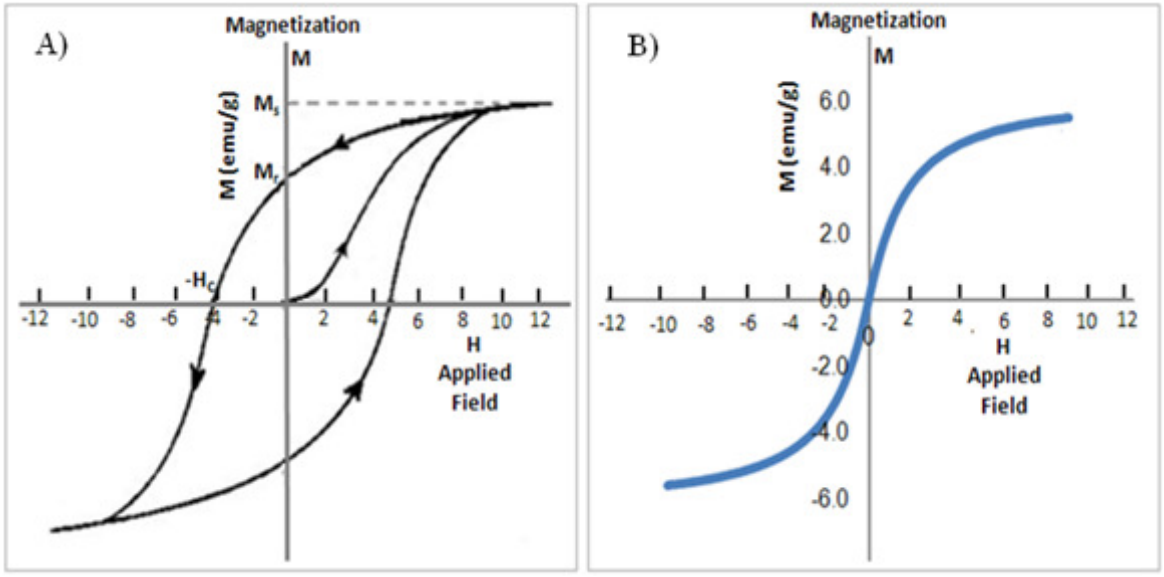

Figure 1-7: Hysteresis curves of (A) ferromagnetic; (B) superparamagnetic nanoparticles. Comparison shows the presence of coercivity or remnant magnetism for ferromagnetic after applied field is reduced to zero while superparamagnets such as iron oxide show no remnant coercivity.

including uses in magnetic resonance imaging (MRI) for contrast enhancement [24, 25], tissue specific release of therapeutic agents [26], hyperthermia, and magnetic field assisted radionuclide therapy [27]. Since the pioneering of work of *Freeman et al.* on the use of external magnetic field coupled with magnetic carriers, a variety of magnetic SPIONs carriers have been employed for drug delivery to specific target sites [28, 29]. The optimization of these carriers continues today with the objectives (i) to reduce the amount of systemic distribution of the cytotoxic drug, thus reduce the associated side effects, and (ii) to reduce the dosage required for more efficacious and localized therapy.

Besides uses as MRI contrast agents, SPIONs are commonly used for hyperthermia applications where they are used as heating agents to induce cell death in tumor cells. The use of hyperthermia (heat) to treat malignant tumors is an old art that has been used since ancient times. In cancer thermotherapy, when particles (SPIONs) are subjected to variable magnetic field heat is generated due to magnetic energy losses. SPIONs embedded around a tumor site and placed within an oscillating magnetic field can heat up to a temperature dependent on the magnetic properties of the material, the strength of the magnetic field, and the frequency of oscillation and the cooling capacity of the blood flow in the tumor site. Cancer cells are destroyed at temperature higher than 43^{o}C, whereas the normal cells can survive at higher temperatures. Heat could be generated applying an appropriate alternating magnetic field. An applied magnetic field can provide the energy to repeatedly reorient particles' magnetic moments which results in magnetic energy losses (due to Néel relaxation and Brownian motion relaxation). These energy losses are converted to thermal energy. For very small magnetic particles such as SPIONs, heating using alternating magnetic field is primarily due to magnetic moment relaxation effect (Néel relaxation) which is expressed by the following equation:

$$M_r = M_i e^{-t/\tau} \quad (\mathbf{1.3})$$

where $\boldsymbol{\tau}$ is magnetic relaxation time, M_i is remanence of particles not affected by relaxation. Because of superparamagnetic materials do not have hysteresis curve (losses), the power losses in SPIONs are only due to relaxation losses (both Brownian and Néel). Néel relaxation, magnetic relaxation time is determined by the ratio of anisotropy energy KV (K is magnetic anisotropy energy density, V is volume of magnetic particle core) to thermal energy kT (k is the Boltzmann's constant and T is absolute temperature and is expressed as:

$$\tau = f_o \exp\left[\frac{KV}{kT}\right] \quad (\mathbf{1.4})$$

where f_o (frequency factor) ~ 10^9 s^{-1}. Néel relaxation is due to the reorientation of the magnetic moment inside a particle while Brownian relaxation is due to reorientation of magnetic particle itself in the fluid. The Néel relaxation time is controlled by the anisotropy barrier while Brownian's relaxation is determined by viscous friction.

The use of SPIONs for hyperthermia have been shown to enhance cytotoxicity of radiation and drug treatment with brain tumor cell lines, which were then confirmed in hyperthermia studies in rat, rabbits and dogs [30]. Hyperthermia treatment has become common for the treatment of the insidious brain tumors such as glioblastoma multiforme whose feasibility was recently demonstrated in a phase II clinical study. The therapy was shown to promote uptake of nanoparticles with no adverse effects resulting from the therapy [31].

In addition to the two applications already discussed, SPIONs have found widespread biomedical applications. Figure **1- 8** shows a maze of potential SPIONs uses which span areas in diagnosis, therapeutic, and cell and biomolecule magnetic labeling. For these applications,

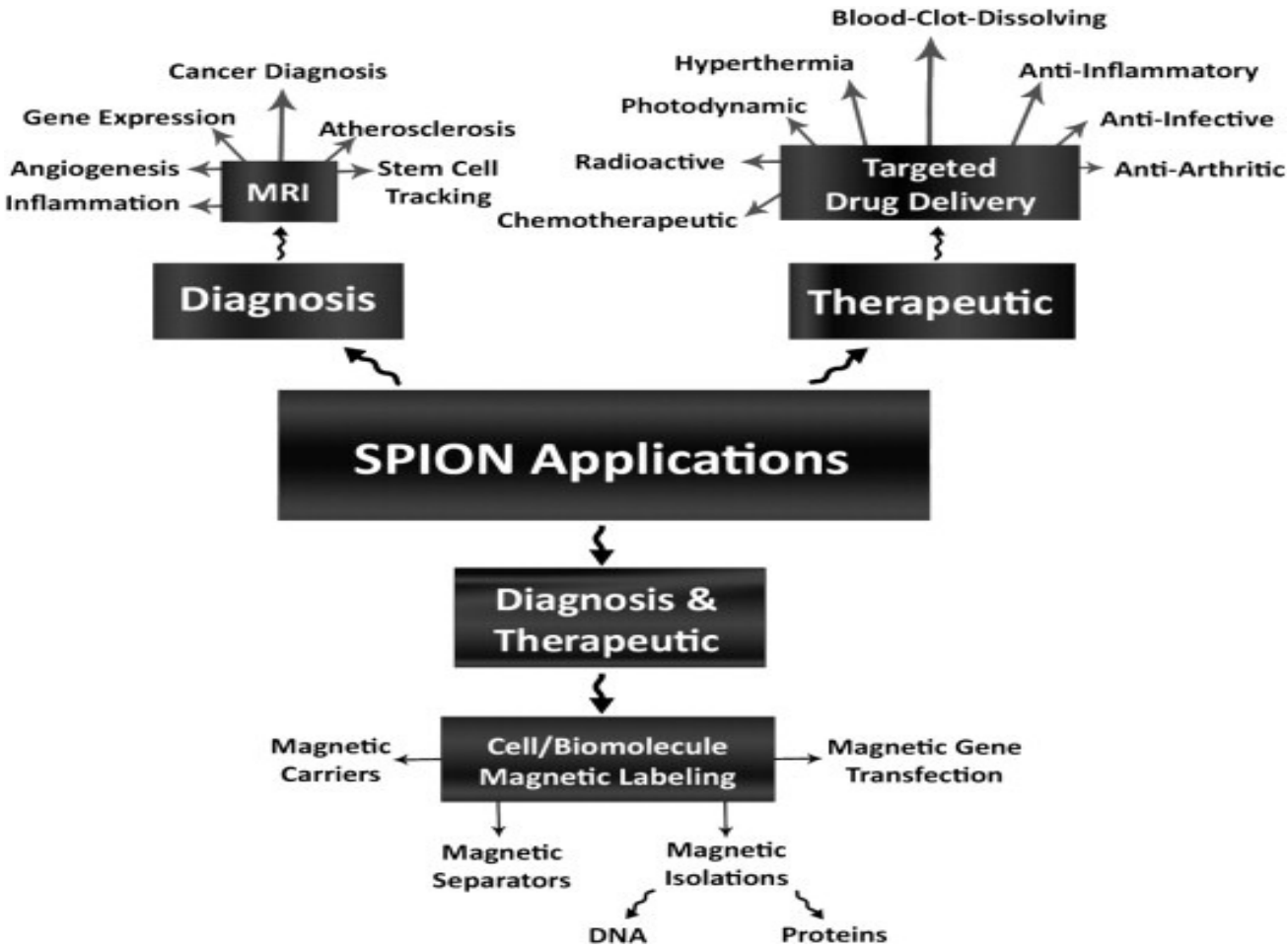

Figure 1- 8: Recent diagnostic and therapeutic applications of SPIONs [76]

SPIONs are rationally designed to exhibit desired size and properties and then functionalized with various types of biomolecules, making them suitable for the intended applications. While the focus of the thesis review dwells on the SPIONs MR imaging application, they can be easily designed for other applications as illustrated on Figure **1- 8**.

1.5. Heterofunctional Nanoparticles

In recent years, combining SPIONs with Au to form composite multifunctional nanoparticles has attracted considerable attention for making platforms of therapy and

diagnostics (theranostics) application. The efforts were originally mostly focused on coating iron oxide particles with thin layer of Au, where the Au shell not only provides convenient anchorage sites for functionalization of biomolecules through well-established Au-thiol conjugation procedure but also protects SPIONs from dissolution and aggregation [32]. However, using this approach makes it difficult to tune the SPR wavelengths to the near-IR region which would limit their uses *in vivo*. Reported core/shell particles usually have their SPR in the visible light range (from 500 to 600 nm) which limits their optical functions for *in vivo* applications [33]. More recent efforts have included the rational design of dumbbell-like heterofunctional nanoparticles with ability to tune the properties of the individual nanoparticles where the SPR absorption can be tuned by changing the size and shape of Au. Examples of bifunctional nanocomposites include CdSe rods surrounded by Au nanoparticles (to form CdSe-Au) which have been used for catalysis. Another example is iron oxide (SPION) nanoparticle surrounded by size-tunable Au NPs, forming SPIONs-Au with strong magnetic and optical properties. These dumbbell-like SPIONs-Au nanoparticles have great potential for dual applications for MR imaging as well as for tunable photothermal therapy that may include *in vivo* therapy applications [34]. Other efforts have also included syntheses of individual nanoparticles followed by chemical conjugations to form bifunctional nanocomposites such as the formation of Au nanorods coated with SPIONs [35]. Figure **1-9** illustrates bifunctional SPION-Au nanoparticles that combine the MR imaging and photothermal therapy functions in a single device for theranostic applications. Additional chemical covalent conjugations to the bifunctional particle composites have also been used to make dual functional particles. For instance, the corona of SPIONs have been conjugated to radionuclides (^{18}F and ^{11}C) and used for combined thermotherapy and radiotherapy of recurrent and deadly glioblastoma multiforme brain

malignancy [36]. Other research efforts have included the attachment of near-IR fluorescent molecules (dye or quantum dots) to make dual imaging probes for MR and NIR imaging (MR imaging and optical properties). The conjugation of molecular specific targeting agents to nanoparticle surface are now ubiquitous and used to make the particle as molecular probes that target specific cells.

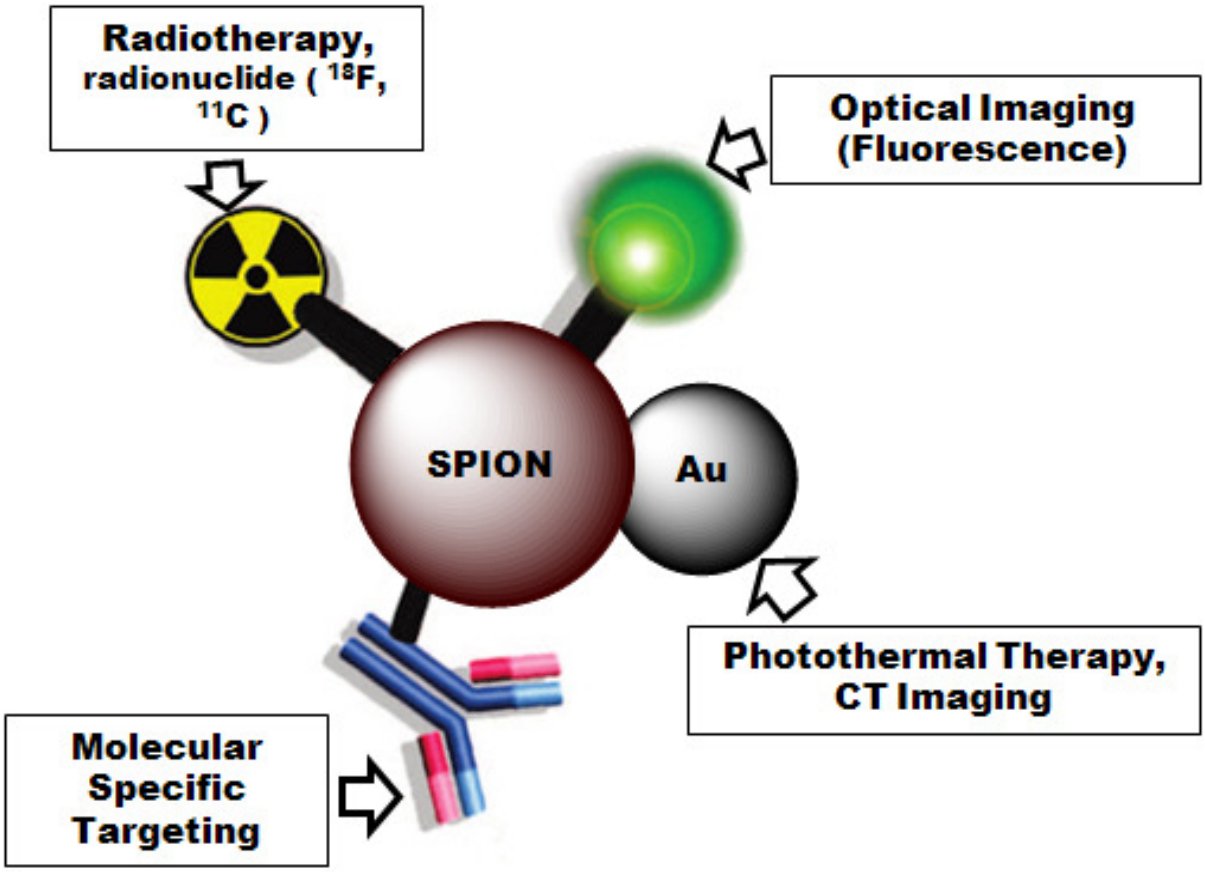

Figure 1-9: Bifunctional nanoparticles illustrating the preparation of multifunctional probes that encompass uses in MR Imaging, molecular targeting, radiotherapy, photothermal therapy and for X-ray based CT imaging.

1.6. Cancer

Cancer is the second killer in the United States under the age of 85, only behind heart disease in 2010 [37]. Currently, one in four deaths in the United States is due to cancer. Nearly half of all men and a little over one third of all women in the United States will develop cancer during their lifetime. Cancer can strike people of any age; although about 77% of all cancers are diagnosed in people age of 55 and older [37]. Cancer arises as a result of DNA mutation or change which alters the normal cell replication cycles and functions. Most of the time when DNA becomes damaged, the body is able to repair it. In cancer cells, the damaged DNA is not repaired [38]. People can inherit damaged DNA, which accounts for inherited cancers. More often, though, a person's DNA becomes damaged due to exposure to carcinogenic toxins through ingestion or repeated contact with toxins. Cancer usually forms as a tumor, however, some cancer such as leukemia, does not form solid tumors. Instead these cancer cells involve blood and blood-forming organs and circulate through other tissues where they grow. Benign (non-malignant) tumors are considered the least deadly form of cancer as they do not spread (metastasize) to other parts of the body while malignant (cancerous) tumors are metastized tumor cells that have entered the blood stream. Cancer develops when cells in the body begin to grow out of control. Although there are many kinds of cancers, they all start because of the out-of-control growth of abnormal cells. Under normal physiological conditions, cells divide and grow in an orderly and controlled fashion. Instead of dying as part of a normal cell cycle, they outlive normal cells and continue to form new abnormal cells [39].

1.7. Colorectal cancer

Colorectal cancer is the third most common cancer in the United States and the second cause of cancer death [40]. The incidence in the United States is approximately 130,000 cases per year and over 50,000 deaths per year result; both incidence and outcome in Europe are similar [41]. Approximately one in every four patients is diagnosed with metastatic disease while the rest are treated surgically to remove benign tumors. However even with complete tumor resection, 50% of all cases will develop recurrence after treatment and die within 5 years of diagnosis. Standard therapies for metastatic colorectal cancer is by chemotherapy using fluororacil modulated by calcium folinate which prolongs the survival time between 10-14 months [42]. Colorectal carcinoma cells have shown high resistance to conventional therapies and as a result the development of novel therapies remains an active area of research. Recent advances in the understanding of the molecular mechanisms underlying the development and progression of cancer have resulted in the discovery of new therapeutic interventions that target specific molecular abnormalities. The development of novel and more efficacious technologies to better treat metastatic colorectal cancer are currently underway. In fact several targeted therapies using humanized, less immunogenic antibodies that selectively target surface biomarkers expressed on the cancer cells are currently under clinical testing [43, 44]. Some examples of these novel therapies currently in clinical trials include: murine IgG2a which targets Ep-CAM, humanized IgG1 which targets VEGF and chimeric IgG1 which targets EGFR [41]. Recent studies have shown that colorectal cancers express high expression of A33 antigen which is a transmembrane glycoprotein and a novel member of the immunoglobulin superfamily that is expressed in normal colonic and small bowel epithelium and in > 95% of human colon cancers. Immunohistochemical testing of normal and malignant tissues has shown A33 antigen expression to be restricted to the epithelia of the lower gastrointestinal tract and to carcinoma

lesions. This antigen system has been selected as a target for clinical studies because the A33 is expressed homogeneously and at higher levels in 95% of metastatic colorectal cancer [45]. It is absent from most other human tissues and tumor types. Owing to the fact the A33 antigen is primarily expressed and restricted human epithelial colon cancers, clinical efforts have identified A33 antigen as a potential biomarker for the selective targeting and treatment of colorectal cancer. This thesis will focus on use of A33 antigen as the colorectal cancer biomarker and its targeting using A33 single chain antibody as used to design novel nanomaterial therapies.

1.8. Cell Receptors and Targeting

Signal transduction "talking" between cells is essential for cell growth. The communication between two cells involves a molecular messenger (referred as a ligand) from the sender and a site (called a receptor) on the membrane surface of the cell receiving the signal. When the signal reaches the surface receptor, the message is passed along from the outer surface of the cell to the cell's nucleus [46]. One of the most common signaling pathways involves receptor tyrosine kinases, which have three components: An extracellular ligand-binding domain receptor that is located on the cell surface and receives incoming signals; a transmembrane domain that crosses the cell membrane and conveys information across the cell membrane; an intracellular tyrosine kinase that phosphorylates (adds a phosphate group) to tyrosine [39]. In cancer targeting, the most important tyrosine kinase signaling networks is a group of receptors belonging to the "HER" family, also known as the ErbB signaling network [47]. The HER family of receptors consists of four main members commonly known as HER1/EGFR (ErbB1), HER2 (ErbB2), HER3 (ErbB3) and HER4 (ErbB4), which demonstrate homology in their kinase

domains, but diverge in their extracellular regions [48]. These receptors are widely expressed in all tissues where they regulate diverse functions such as mitogenesis, differentiation, and cell survival. Different ligands and protein-protein interactions contribute to the diverse signaling networks that characterize each receptor which are involved, in some way, in the development of malignant tumors. Some of these receptors are overexpressed and more involved than others in different cancers. In all cells, some level of growth-signal transduction is normal and is part of the regular growth cycle. The over-expression or activation of these signals leads to uncontrollable cell proliferation and thus leads to cancer. For example, in the case of the HER2, over-expression results from a genetic alteration that generates multiple copies of a gene that encodes a growth receptor. For colorectal adenocarcinoma, A33 surface receptor is over-expressed and thus has become important in the development of novel therapies.

1.9. Antibodies (mAbs) in Cancer therapy

Antibodies are important components of the immune system, yet they have also found applicability in the treatment of a number of diseases, including cancers. In particular, monoclonal antibodies (mAbs) belong to a class of molecules that are specifically engineered to bind to targets of interest with high affinity. Their specificity and the potential to preferentially bind to receptors over-expressed on tumor cells make them an attractive therapeutic approach. For many years, research efforts have focused on the identification of cell-surface antigens whose expressions are restricted to tumor cells and can be used as specific targets for engineering antibodies. Originally, an ideal antigen was considered one that is preferentially expressed in high copies on the surface membrane of tumor cells, plays a causal role in tumor development, stable, and not shed or secreted to the bloodstream. Now, recent efforts have

expanded to the development of antibodies that can attach to tumor vasculature by targeting antigens associated with the formation of new blood vessel, angiogenesis, which plays a major role in the development of tumors [41].

The first mAbs engineering were derived from mouse but the immunoglobulin immune response in the majority of patients have limited their clinical applications. Alternative strategies of producing less immunogenic mAbs have been underway. The chimeric mAbs engineered by replacing the mouse constast domains of the antibody with human constant domains was the second generation of mAbs. Further improvement came with the creation of humanized

Table 1-1: Monoclonal antibodies as therapy for colorectal cancer [41]

Name	Antibody Type	Target	Phase of Development
Edrecolomab(Centocor/GlazoSmithKline)	Murine IgG2a	Ep-CAM	Phase III
Bevacizumab(Genentech)	Humanized IgG1	VEGF	Phase III
Cetumixab (Imeclone/Bristol Myers Squibb)	Chimeric IgG1	EGFR	Phase III
ABX-EGF (Abgenix/Amgen)	Fully Human IgG2	EGFR	Phase II
EMD 72000 (Merck)	Humanized IgG1	EGFR	Phase 1

Ep-CAM, 17-1A antigen, VEGF, vascular endothelial growth factor, EGFR, epidermal growth factor receptor

antibodies that are derived from human cells or genetically engineered mice in which murine immunoglobulin genes have been replaced with human antibody genes [49]. The treatment colorectal carcinoma has benefited from the development of mAbs, many of which are currently in various stages of clinical testing (Table **1-1**). For instance, five antibodies are currently in different stages of development namely: edrecolomab (mAb 17-1A), bevacizumab (Avastin), cetuximab (IMC-C225), ABX-EGF and EMD 72000.

Immunogenicity and the bulky sizes of antibodies are two main challenges with the use of mAbs for cancer therapy. To overcome these drawbacks, recent efforts have expanded to the engineering of single chain antibodies (scFv), composed of variable heavy and light chains of immunoglobulin (IgG) linked by a peptide linker. A typical molecular weight of scFv is M_r ~ 27,000 and M_r ~ 150,000 for a whole IgG antibody. The low molecular weight of scFv is advantageous because it results in rapid plasma clearance and faster tumor penetration, resulting in high tumor: blood ratios at early time points in animals and in humans. The use of scFv could be lead to the development of more efficacious therapies as compared to mAbs [50]. Example of the various scFv that have been developed for the targeting and treatment of colorectal carcinoma cells include: Anti-CEA scFv genetically engineered for use in radioimmunoguided surgery [51], and A33scFv which an analog of murine IgG2a (mAb3 A33) currently in phase III trials [52]. We have recently prepared A33scFv using Pichia *pastoris* [53] in our Laboratory and have tested their efficacy for targeting in colorectal cancer cells both *in vitro* and recently in xenograft murine models.

1.10. Nanotechnology in cancer Therapy

The tremendous developments in nanotechnology have enabled the syntheses of a variety of nanostructures with different shapes and structures of different composites [54-56]. These nanostructures demonstrate unique electronic, photonic, catalytic, highly controlled and interesting properties as a consequence of size reduction from bulk to nanometer scale, as detailed in the following reviews [57, 58]. These nanoparticles exhibit similar size dimensions to many common biomolecules such as proteins and DNA, thus offer great possibilities for the integration of nanotechnology with biotechnology. Typical applications include contrast agents

for disease diagnostics and therapies [58], biological labeling [59], optoelectronics [60], and surface-enhanced Raman scattering (SERS) [61]. The use of nanoparticles in medicine is currently one of most exciting developments in nanotechnology. Their applications in drug delivery [62, 63], cancer cell diagnostics [64, 65] and therapeutics [66, 67] are active fields of research. Advances in this field have further sparked interest in the development of multifunctional devices with combinatorial use for therapy and diagnostics which has been referred to as theranostics. For instance, drug-loaded iron oxide nanoparticles can be used as contrast agents for magnetic resonance imaging as well as drug delivery systems. The applications of nanomaterials as it relates to various biotechnological uses geared towards improving the efficacy of disease diagnosis and therapy will be further reviewed in this thesis.

1.11. Nanomaterials in Cancer Imaging

1.11.1. Magnetic resonance based Imaging

Imaging plays a critical role in overall cancer management: in diagnostics, staging, radiation planning, and evaluation of treatment efficiency. Standard clinical imaging modalities such as CT, MRI, and ultrasound are considered structural imaging modalities that can identify anatomical patterns and thus provide basic information regarding tumor localization, size, and spread based on endogenous contrast [68]. Magnetic resonance imaging (MRI) has become a valuable modality in cancer detection due to its high soft tissue contrast, spatial resolution and penetration depth. It is a non-invasive technique that involves the disturbance of aligned nuclear protons spins in a strong magnetic field; and their realignment following an application strong magnetic field is used to create spatial image of soft tissue. The MR image acquisition is performed by obtaining the relaxation times of sample classified as T_1 or T_2 relaxation times. Two types of relaxation times T_1, or spin-lattice (longitudinal) and T_2, or spin-spin (transverse),

determine the signal for a particular tissue. T_1-weighted images are a result of longitudinal relaxation time while T_2-weighted images rely on the rate of transverse relaxation to give positive and negative contrast enhancement in the MR image, respectively [57]. MR imaging require the use contrast agents because the imaging modality alone is not efficient in detecting tumors and metastases that are smaller than 0.5 cm and they can barely distinguish between benign and cancerous tumors.

Significant research in the field of medical MRI has focused on the development of contrast agents to improve imaging signal intensity and reduce noise. Contrast agent research has focused on gadolinium (Gd)-based MRI agents due to their ability to decrease the T1 relaxation time, thus increasing (brightening) the MR signal. These Gd chelates are also referred to as T1 contrast agents because they shorten the proton relaxation time, resulting in bright images as compared to the surrounding tissues. In fact there are several FDA approved products that are currently for medical imaging. Some examples of FDA-approved gadolinium-based contrast agents for clinical applications include: gadodiamide (*Omniscan*®), gadobenic (*Multihance*®), and gadopentetic acid (*Magnevist*®). They have been utilized to enhance blood vessels in brain tumor imaging [69]. However, one potential drawback of using paramagnetic Gd chelates is that relatively high concentrations are needed to achieve a sufficient increase in contrast signal which increases chances of acute toxicity.

Recent efforts have focused on developing superparamagnetic iron oxide (SPIONs) as alternative negative contrast enhancers for MRI due to their ability to shorten T2 relaxation times. SPIONs are predominantly used as MR contrast agents because of their low toxic and good biocompatibility. In fact, a number of SPIONs contrast agents are used clinically such as Endorem (*Feridex*®), *Resovist*®, *Sinerem*®, and *Combidex*® which are all referred to as T_2

contrast agents [70]. These contrast agents reduce the T_2 signals of absorbing tissues, resulting in darker MR images. With the aim of increasing the specificity and selectivity of these contrast agents, the emerging field in molecular imaging seeks to integrate various targeting agents (mAbs, scFv, aptamers) in order to design more selective molecular probes with a broader applications in medicine. Research and the development of antibody-conjugated SPIONs are intended for imaging solid tumors [71], drug delivery [72], hyperthermia cancer treatment [73], and can also be used to monitor progression of disease treatment. For example, targeted SPIONs have been used in therapeutic strategy to deliver siRNA and also to image the accumulation in the targeted tumors *in vivo* [74]. The assessment of the biocompatibility, bio-distribution and *in vivo* clearance of superparamagnetic iron oxide nanoparticles (SPIONs) are well documented [75-79]. For example, dextran-coated SPIONs have no measurable cytotoxocity index LD_{50} in animal models [80]. In general, SPIONs are typically synthesized and coated in surfactants and are subsequently functionalized to make them biocompatible and allow the encapsulation and/or attachment specific targeting or therapeutic drug [81].

1.11.2. Fluorescence Imaging

Fluorescence imaging involves the detection of light emitted from molecules or materials subsequent to their excitation at a specific wavelength. Fluorescence imaging of cancerous tissue can be traced back to the mid 1900's where fluorescein was used to improve the detection of brain tumors [82]. More recent discoveries of near-infrared (NIR) fluorophore capable of penetrating into heterogeneous biological samples has helped improve limitations of fluorescent imaging and has led to an increase in biological applications of NIR fluorophores. To allow biological cellular labeling and tracking, small fluorescent molecules (such as fluorophore dyes

and quantum dots) have been conjugated or encapsulated with metallic NPs to build multifunctional composites. It has been shown that nanoparticle scaffolds allow the multivalent attachment of dyes to increase their effective local concentration. Some of these materials have found applications in multimodal imaging uses depending upon the particle composition or modification. For example, iron oxide nanoparticle-NIR fluorophore conjugates have been shown to be useful in tumor imaging with the aid of targeting ligands such as plasma clotting peptides that lead to enhanced tumor uptake [83] and hepsin-targeted peptides for prostate cancer [84]. Quantum dots (QDs) are highly fluorescent particles that have found recent use in cancer imaging because of their versatility and brightness that can be easily tuned to different emission wavelengths [85]. Hybrid magnetic-fluorescent QD nanoparticles have been shown to detect tumors in mice by both MRI as well as fluorescent imaging allowing for enhanced resolution as well as anatomical information [86]. Fluorescence imaging has become increasingly popular over the past decade and is now a highly valuable resource in biological imaging.

1.11.3. X-ray based computed tomography (CT Imaging)

The other imaging modality that has gained more interest for biomedical imaging is X-ray based computed tomography (CT) imaging. CT imaging is one of the most useful diagnostic tools in hospitals today in terms of availability, efficiency, and cost. CT distinguishes between different tissues based on the fact that different tissues provide different degrees of X-ray attenuation, where the attenuation coefficient is determined by the atomic number and electron density of the tissue; the higher the atomic number and electron density, the higher the attenuation coefficient. Currently, it is not molecular imaging modality since relevant targeted and molecular specific contrast agents have yet to be approved for clinical use. Present CT contrast agents are predominantly based on iodine containing molecules, which are effective in

absorbing X-rays; however they are nonspecific because they cannot be conjugated to biological components or cancer markers and allow only very short imaging times due to rapid renal clearance [87]. Recent advances in nanotechnology-based CT imaging have demonstrated the feasibility of using gold nanoparticles to induce *in vivo* vascular contrast enhancement. The atomic number and electron density of gold (79 and 19.32 g/cm^3, respectively) are much higher than those of the currently used iodine (53 and 4.9 g/cm^3) and are being developed as CT contrast agents. Gold provides about 2.7 times greater contrast per unit weight than iodide [88]. Additionally, gold nanoparticles provide a high degree of flexibility in terms of functional groups for coating and attachment of specific targeting agents. Additionally, gold nanostructures have been shown to be nontoxic and biocompatible *in vivo* [89]. Most recent efforts on the development of targeted gold nanoparticles for molecular CT imaging have shown promising results. For example, *in vitro* proof of principle experiments using head and neck cancer have shown 5 times higher attenuation coefficient for targeted cells as compared to untargeted cancer cells or normal cells [87]. Other hybrid nanoparticles such as PEG-coated nanoparticles, antibiofouling polymer-coated gold nanoparticles, gadolinium-coated gold nanoparticles [90], and polymer-coated Bi_2S_3 nanoparticles [91] are currently under investigation as vascular CT contrast agents.

Recently, *Hainfeld et al* and coworkers, demonstrated successful use of 1.9 nm gold nanoparticles in vivo imaging in mice following intravenously injection [88]. As compared to commercially available CT imaging agents, such as (Acepaque® ans Visipaque®, Amersham Health (now GE healthcare)), the gold nanoparticles were shown to have stronger CT signal as well as longer blood retention times allowing for extended imaging durations. Improved contrast may allow enable non-invasive detection of small tumors (< 1 cm).

1.12. Gold Nanostructures in Photothermal Therapy

1.12.1. Gold Nanoparticles

Au NPs absorb light millions of times stronger than the organic dye molecules. Nearly 100% absorbed light is converted to heat via the nonradiative properties, as discussed previously (**sections 1.3** and **1.4**). Au gold nanostructures also are photostable and biocompatible [92]. These features make them novel agents for photothermal therapy, in which photon energy is converted to heat sufficient to induce cellular damage via thermal effects such as hyperthermia, coagulation and evaporation. Phothermal therapy (PTT) using gold nanospheres can be achieved with pulsed or continuous-wave (cw) lasers in the visible range (500- 600 nm) which is coherent with the SPR absorption of these particles. This therapy is suitable for hyperthermic treatment of shallow cancer such as skin cancer. Lin and co-workers et al. reported the first extensive study of gold nanospheres with pulsed laser where selective and highly localized photothermolysis of targeted lumphocytes cells was achieved [93]. Lumphocytes incubated with antibody-conjugated Au NPs were exposed to nanosecond laser pulses (Nd: YAG laser, 565 nm wavelength, 20 ns duration) showed cell death with 100 laser pulses at an energy of 0.5 J/cm^2. In contrast, adjacent cells just a few micrometers away but without nanoparticles remained viable. Since then, numerous studies have demonstrated the use of gold nanospheres in combination with laser irradiation (with excitation coherent with the SPR absorption) as a highly selective method of cell killing with broad applications in targeted cancer therapy [94, 95]. The localized cell damage is controllable from a few nanometers to tens of micrometers depending on the laser pulse duration and particle size. The treatment using CW lasers is time consuming (minutes) compared to pulsed laser (single pulse time). Another example of using CW lasers for PTT includes selective cancer cell killing and targeted macrophage destruction [96].

1.12.2. Gold Nanorods and Photothermal Therapy (PTT)

The use of gold nanoparticles for PTT has been limited by the depth of penetration of visible light which has been shown to be effective only up to a few micrometers from the laser source. *In vivo* therapy of tumors under skin and deeply seated within tissue, has led to the utilization of nanostructures with SPR absorption in the near infrared region (NIR) because of its deep penetration owing to minimal NIR absorption by hemoglobin and physiological components (including water) in tissues at this spectral region. The advances in PTT therapy over the years have attributed to the emergence and use of gold nanorods (Au NRs) for photothermal therapy. El-sayed *et al* first demonstrated the use of gold nanorods for *in vitro* cell therapy in which NRs conjugated to anti-EGRF antibodies specifically bind to ENT cancer cells. In the PTT treatment with Ti: Sapphire laser 800 nm, it was found that cancer cells required half the laser energy (10 W/cm^2 for 4 min) to be photothermally damaged as compared to normal cells (20 W/cm^2, 4 min) [97]. Extensive research in the use of gold nanorods conjugated to various types of targeting moieties (e.g. peptides, proteins, antibodies) is currently underway in which numerous reports have proven their potential applications using *in vivo* PTT models [15, 98]. Gold nanorods have become a preferred for PTT modality as compared to gold nanoshells due to their wide and tunable absorption profile which can be easily adjusted by changing the nanorod aspect (700-1200 nm) to match the excitation of the laser source. Additionally, the easy of surface functionalization using thiol chemistries have made them much more attractive to form stabile nanorod antibody suitable for in vivo applications. In this thesis review, common the synthetic procedures for gold and iron oxide nanostructures that have been discussed by summarized.

1.13. Synthesis of Gold and Iron Oxide Nanostructures

1.13.1. Size-controlled Growth of Au NPs

Substantial research efforts have been devoted to the syntheses of monodisperse Au NPs, ranging of nanoparticles a few nanometers to hundred nanometers by various methods, as reviewed by several authors [99-101]. Au NPs have been prepared both by "top down" and bottom up strategies. Top down method is where Au bulk is broken down in into smaller particles using a strong irradiative force, for example, ion irradiation in air [102] or arc discharge in water which generates Au NPs [103]. These Au NPs are typically used in suspension and require addition stabilization with surfactants in order to prepare stabile nanoparticles suitable for a wide range of applications. However, the use of "top down" method has been limited because it is difficult to control size, shape, and the particle distribution. The "bottom up" method refers to wet chemical processes used to prepared nanoparticles which include: chemical reduction of Au salts, electrochemical pathways, and decomposition of organometallic compounds. Chemical reduction method is commonly preferred because it is simple and controllable; it has been used to prepare Au nanoparticles of various sizes and shapes. Figure **1-10** depicts a general chemical reduction mechanism method used to prepare various gold nanostructures ranging from nanoparticles (one-dimensional), nanorods, nanobelts, and nanokite (multi-dimensional) [104]. Many functional Au NPs are synthesized by a two-step procedure: (1) nucleation and (2) successive growth. Initially, nucleating centers of Au NPs are formed by reduction reaction of Au precursors or salts. Successive growth from the Au seed particles is performed under controlled and specific conditions of chemical concentration, surfactant, pH, temperature which leads to formation of the various types of Au nanostructures depicted on Figure **1-10**: (larger Au NPs, nanorods, nanocages, etc) which are largely dependent on the growth parameters and conditions.

A common method of preparing spherical Au NPs is by reduction Au precursor ($HAuCl_4$) in the presence of citrate which has been used to synthesize a wide range of NPs sizes, from ~ 10 to 150 nm. This procedure is modulated by changing the relative amounts of Au precursors to the amount of reducing reagents. For example, in a typical synthetic reaction an aqueous solution of tetrachloroauric acid is heated to boiling point and then trisodium citrate is added into the solution. Citrate acts as both reducing and stabilizing agent, adsorbed to the particle surface. The adsorption of citrate on the particles acts as particle stabilizer and significantly affects its size. In this stage, particle size decreases as the citrate/$HAuCl_4$ ratio increases because of the stabilizing process of citrate. Using a higher citrate concentration allows rapid and complete stabilization of Au NP, while lower citrate concentrations results in larger aggregated Au NPs due to incomplete citrate surface coverage [105].

Citrate plays multiple roles when used for as particle synthesis and consequently increases the complexity of the particle preparation process. As result of this complexity, recent synthetic efforts have used sodium borohydride, instead, as a reducing agent used to form small Au seeds. Larger Au NPs are then prepared by successive growth using a small amount of Au seeds as nucleation centers in a solution of mildly reduced tetrachloroauric acid ($HAuCl_4$) where ascorbic acid is used as a mildly reducing agent. Additionally, cetyltrimethylamonium bromide (CTAB) is now commonly used as a surfactant instead of citrate [106].

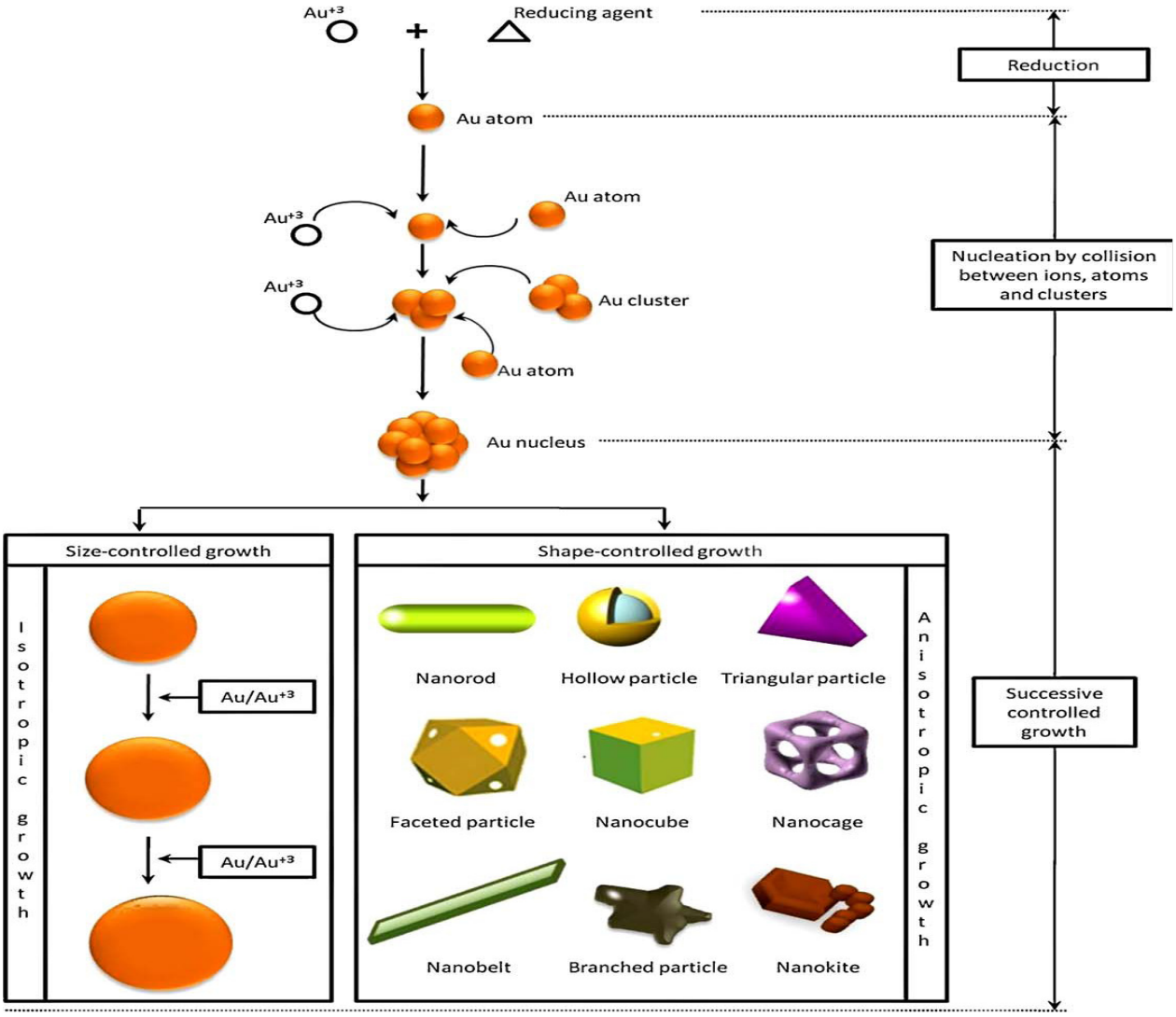

Figure 1-10: Illustration of Synthetic procedure involved in preparation of Gold nanostructures [103]

1.13.2. Gold Nanorods

Non-spherical Au NPs of different shapes are prepared from the anisotropic growth of Au seed particles which is facilitated by the addition of surfactants such as cetytrimethylammonium bromide (CTAB), sodium dodecysulfonate (SDS) and poly(vinylpyrrolidone) (PVP) [107-109]. This thesis review will focus on the synthetic preparatory methods of gold nanorods and gold

nanostars for which the applications have been discussed. While there have been numerous synthetic methods for the preparation of gold nanorods such as high-temperature seedless synthesis [110] , synthesis by microwave irradiation [111] , pH-triggered synthesis [112], and by photochemical strategies [113], a two-step seed-mediated method in the presence of CTAB remains the most facile and commonly for the preparation of finely-tuned gold nanorods. This method yields gold nanorods with controlled size and monodispersity that is dependent on the concentration of precursor salt, structure of seed particles, surfactant concentration, particles, temperature, pH and aging time [56, 114, 115]. A direct surfactant templating mechanism is the leading proposed mechanism for the rod formation in the presence of CTAB [116]. In brief, CTAB covers the seed particles to form a template with certain size which depends on CTAB concentration and over ionic strength of the solution. However, CTAB binds preferentially to the {110} facet of Au seed particles and retards the crystal growth on this face. The growth of seed particles is controlled by the diffusion of Au atoms onto nucleating Au template where diffusing Au atoms are preferentially deposited on {100}, and not on {110} facet. The rod aspect ratio is controlled by supplying Ag atoms (generated the reduction reduction of Ag ions) and preferentially deposited on the {110} facet fast than on the {100} facet. The seed particles, therefore, will favorably grow along {100} direction. Increasing Ag concentration results in more Ag deposition on the {110} facet will lead to the formation of Au nanorods with higher aspect ratio. Over the years, this seed-mediated method has been shown to be facile. It has been used to prepare rods of a wide variety of aspect ratios with absorbance ranging from 600 to 1200 nm. Modified synthetic method using binary surfactant mixture containing CTAB and benzyldimethylammoniumchloride (BDAC) has been proposed and used to prepared gold nanorods with larger aspect ratio (> 5)[56].

1.13.3. Au Nanostars

The use and synthesis of gold nanostars have garnered attention due to their strong scattering properties which have found various applications, most notably for surface enhanced resonance (SERs)-based imaging and detection of small molecules. The most commonly reported preparatory method for Au nanostars is by seed-mediated method using poly(vinylpyrrolidone) (PVP) as a surfactant instead of CTAB used in Au NRs synthesis [117]. PVP acts not only as a surfactant but also as a reducing agent and thus enables preparation of Au NPs from precursor without the addition of any other reducing agent. PVP blocks the {111} facet of Au NPs and prevents growth along this direction. For example, *Yamamoto et al* prepared star-shaped nanoplates of Au NPs using PVP as a single crystal of flat plate with {111} face and six symmetric horns extending in the [112] direction [54]. The amount of PVP used and water are the process variables that control the final particle shape where varying the amount of PVP can change the surface energy, crystallinity of PVP, and coverage of PVP on the initial Au nuclei. As shown, Figure **1-10** summarizes the synthetic procedures for the preparation of all types of gold nanostructures, including intricate two-dimensional structures such as nanobelts, nanocages, and nanokits.

1.14. Synthesis of Iron Oxide Nanoparticles

Superparamagnetic iron oxide nanoparticles (SPIONs) have been subjects of extensive research over the past decade owing to their promising uses as contrast agents in magnetic resonance imaging (MR) based imaging. While there are numerous synthetic methods for the preparation of SPIONs (e.g. gas phase deposition and lithographic methods), wet chemical routes methods have proven to be the easiest, facile, and offer appreciable size control [118]. Initially,

SPIONs have been prepared by a simple acid-base reaction by adding a base to an aqueous mixture of Fe^{2+} and Fe^{3+} chloride at a 1:2 molar ratio resulting in a black precipitate of magnetite (Fe_3O_4). The chemical reaction of Fe_3O_4 precipitation is given the overall reaction:

$$Fe^{2+} + 2\,Fe^{3+} + 8\,OH^- = Fe_3O_4 + 4\,H_2O \qquad (\mathbf{1.3})$$

According to the thermodynamics of this reaction, a complete precipitation of Fe_3O_4 should be expected between pH 9 and 14. This method and numerous variations of this procedure [119] have been used to prepare Fe_3O_4 nanoparticles soluble in aqueous medium and can allow rapid coating with biomolecules such as proteins. However, SPIONs prepared using these methods are prone to aggregation which limited their potential *in vivo* applications. Recent synthetic efforts to produce stabile and monodispersed SPIONs with narrow size distribution have been accomplished by organic-phase synthesis of thermal decomposition of iron precursors. Seminal research using this method was first reported by *Sun et al* where 4-nm SPIONs coated with oleic acid were synthesized. The preparation of SPIONs up to 20 nm is size were subsequently synthesized by seed-mediated method using smaller 4-nm SPIONs as nucleation seeds [120]. In brief, 4-nm SPIONs have been prepared by mixing iron precursor ($Fe(acac)_3$), reducing agent (hexedecanethiol), and ligand molecule (oleic acid) in organic solvent (phenyl ether). The mixture containing iron precursor is then reduced by heating to 375^{o}C for 1 hr which leads to reduction of brown iron ions, forming black SPIONs precipitate coated with oleic acid. Figure **1-11** shows TEM micrographs comparing the monodispersity of SPIONs resulting from different strategies. The preparation of biocompatible SPIONs suitable for biological applications has been carried by particle surface modification using methods such as ligand exchange reaction and polymer coating.

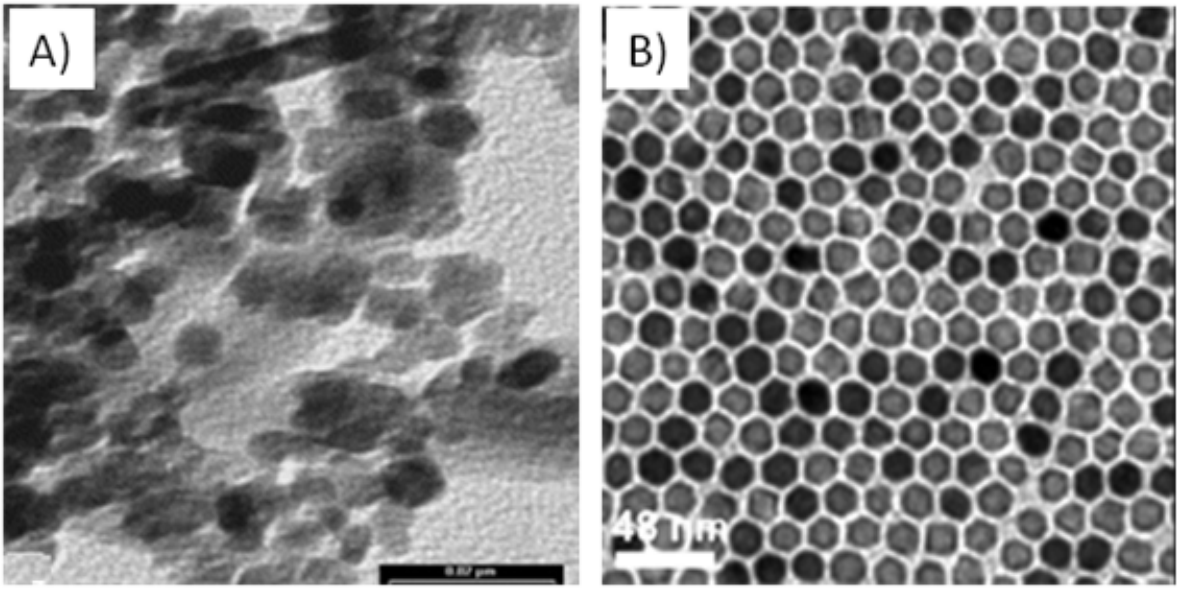

Figure 1-11: Transmission electron microscopy (TEM) micrographs of SPIONs prepared by; a) acid-base reduction of iron precursor in aqueous solution; b) organic-phase thermal decomposition method which shows monodispersed SPIONs [117, 119].

1.15. Functionalization of Nanoparticles

As synthesized, nanostructures are typically stabilized or coated with inert functional groups that do not allow the attachment of biomolecules. Additionally, these function groups are cytotoxicity and limit uses of nanostructruees in biological systems. Consequently, prior functionalization is required in order to increase biocompatibility, reduce cytotoxicity, and to introduce useful functional groups on which the biomolecules can be anchored. Various functionalization strategies used for the various types of nanostructures can be categorized into: ligand exchange reaction, phase transfers, and additional coating layers. This review will summarize some of the most commonly used methods for gold nanoparticles and for iron oxide particles functionalization.

1.15.1. Gold Nanostructures

Bare or surfactant-stabilized Au nanostructures are unstable and cytotoxic in physiological conditions and tend to aggregate forming large aggregates, which result in rapid clearance from the bloodstream. The shortened blood half-life reduces the efficacy of gold-based biomedical systems where longer organ contact time is required. Fortunately, the use of the facile Au-thiol chemistries have made gold nanostructures easy to functionalize and attractive for various bio-applications. Au nanostructures suitable for a wide variety of applications have been developed by attaching different functionalities and biomolecules onto the surface of Au NPs. After functionalization, gold nanostructures have been shown to retain the desired reactivities, biocompatibily properties, and native optical properties. Ligand-exchange reactions where molecules stabilizing the particles in the original first phase are replaced by other, more strongly binding ligands that improve particle stability and allow subsequent attachment of biomolecules. Examples of the different functional groups that have been reported for gold functionalization include: thiol (-SH)[121], hydroxyl (-OH) [122], phosphine ($-PH_2$) [123], and amino ($-NH_2$) [124] groups with a wide array of long and short chain alkyl groups. Thiol-containing ligands are predominant as the most effective functional group for Au NPs because of the strong Au-S covalent bond. Some examples of the thiolated ligands reported in the literature include: alkythiol [125], thiol-terminated dendrimers [126], peptide [127], polypeptide [128], and their derivatives. Additionally, to improve the biocompatibility and stability of Au NPs, ligand molecules on the surface have been exchanged with thiolated polymeric molecules which increase their solubility in aqueous conditions. Most commonly, thiolated polyethylene glycol moieties have been used as they provide "stealth" properties – a critical property for nanostructures used for *in vivo* applications.

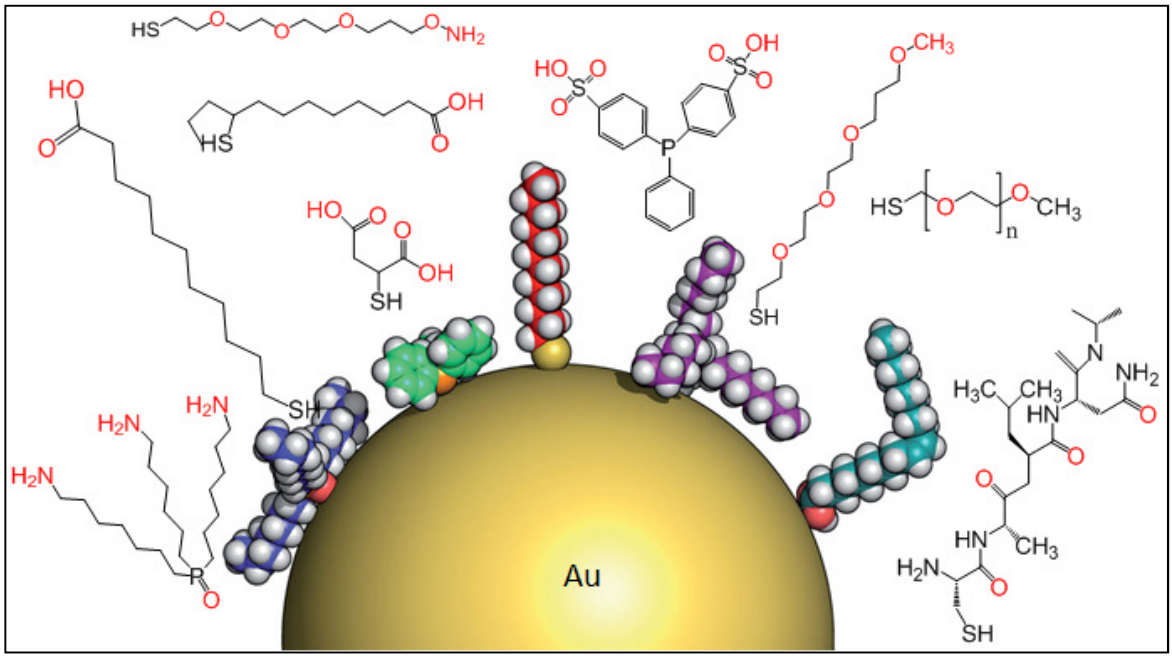

Figure 1-12: Au Nanoparticle core with different hydrophilic and hydrophobic ligand molecules used to prepare biocompatible nanoparticles suitable for bio-applications.

An alternative approach to ligand-exchange functionalization strategy is reverse-phase transfer: a hydrophobic ligand molecule stabilizing the nanoparticles in organic phase is coated with amphiphilic molecules/ polymers, resulting in water-soluble particles. For example phosphine-stabilized Au NPs [129] or oleic acid- coated Au NPs can be functionalized by reverse-phase micelle formation using amphiphilic phospholipids or block copolymers forming micelle-like particles that are less prone to destabilization in salt concentration[130]. Some examples of amphiliphilic polymers that have been used include: carboxylated phosphoethanolamine-polyethylene glycol (PL-PEG-COOH), thiolated phosphoethanolamine-co-polyethylene glycol (PL-PEG-SH), or aminated phosphoethanolamine-polyethylene glycol (PL-PEG-NH_2) (Avanti Polar lipids). For example, we have recently reported the use PL-PEG-COOH to prepared monodispersed Au NPs that were subsequently attached to PHA synthase[131].

Other efforts have coated Au with thin layers of mesoporous silica that allow subsequent attachment of other molecules such as drugs, antibodies, and molecular dyes [132] . Figure **1-12** illustrates some of derivatization strategies used to prepare biocompatible Au nanostructures. It shows representative hydrophobic and hydrophilic ligand molecules that have been used to prepare stabile water soluble Au nanostructures as template for designing multifunctional probes with potential applications in therapy and as well for imaging.

1.15.2. Surface of coating of SPIONs

Surface coatings are critical integral component when designing SPIONs for potential biomedical applications. Although not attracted magnetically, due to their superparamagnetic properties, SPIONs nanoparticles still have a significant tendency to agglomerate as a result of their high surface energy. Colloidal electrostatic stabilization arising from repulsion of surface charges on the nanoparticles is typically inadequate to prevent aggregation in biological solutions due to the presence of salts or other electrolytes that may neutralize this charge. In addition, particles used for in vivo are subject to various pressure change and plasma protein interactions. For example, it is has been shown that improperly functionalization SPIONs are rapidly adsorbed to plasma proteins (opsonized) and rapidly cleared through the liver kupfer cells which reduces the particle blood residence time. One of challenges is the use of particles for various biomedical applications is the is coating SPIONs with appropriate stealth moieties to achieve longer blood residence time as well as avoid reticuloendothelial (RES) particle clearance [133].

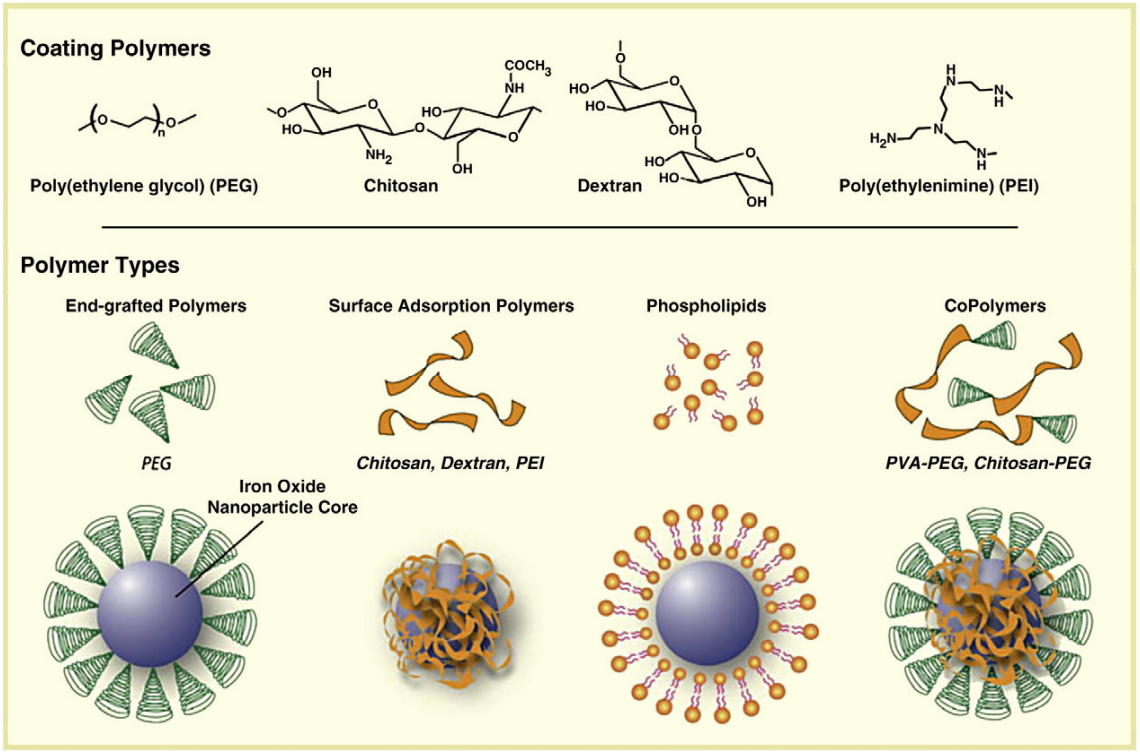

Figure 1-13: Surface coating of SPIONs with a variety of different polymers that make SPIONs suitable for *in vivo* applications.

There are a variety of natural and synthetic polymers have been evaluated for use as coatings on SPIONs. One of the most widely utilized used polymer coatings on SPIONs intended for in vivo applications, has been the polysaccharide dextran [134]. For instance, Weissleder et al have developed various formulations of dextran-coated SPIONs which have been evaluated extensively for a variety of MR imaging applications [135]. Poly(ethylene glycol) (PEG) is another widely used polymer for nanoparticle coating in biomedical applications [136] due to its antifouling nature that has been shown to reduce nanoparticle uptake by macrophages and extend *in vivo* circulation time [137]. Other polymeric coatings that have been used include: poly (vinyl alcohol) (PVA), polyethylenimine (PEI), chitosan, phospholipids, and a combination of these polymers and are illustrated on Figure **1-13** The SPIONs coated with these polymers result

in different structures that depend on the hydrophobicity/hydrophilicity of the polymer chain which may also determine the hydrodynamic size of the particles in aqueous solution (see Figure 1-**13**). Polymeric coatings provide a steric barrier to prevent nanoparticle agglomeration and avoid opsonization. Additionally, it provides a means to attach biomolecules such as peptides and antibodies. For example, we have recently prepared carboxyl-terminated 10-nm SPIONs by reverse-phase coating of oleic acid-stabilized SPIONs with carboxy-PEGylated phospholipids (PL-PEG, Avanti Polar lipids), resulting of SPIONs that can be easily attached to various molecules.

1.16. Importance Consideration in Nanoparticles Design

As stated previously, a significant challenge associated with the application of nanomaterials systems is their behavior under physiological conditions. The efficacy of many of these systems is often compromised due to recognition and clearance by the reticuloendothelial system (RES) prior to reaching target tissue, as well as the inability to overcome biological barriers, such as the vascular endothelium or the blood brain barrier [133]. The fate of these SPIONs upon intravenous administration is highly dependent on their size, morphology, charge, and surface chemistry. These include particle properties such as size, shape, surface charge (zeta potential), solubility, surface modifications (including specific targeting agents), and route of administration. There have been numerous reviews dwelling on the importance of these factors and how each can be rationally designed to influence bio-distribution [138]. When nanoparticles enter the bloodstream, they immediately encounter a complex environment of plasma proteins and immune cells. Nanoparticle uptake by the immune cells may occur both in the blood stream by monocytes, platelets, leukocytes, and dendritic cells and in tissues by resident phagocytes

(e.g., kupffer cells in liver, macrophages and B cells in spleen). Nanoparticle uptake by immune cells may occur through various pathways and can be facilitated by the adsorption of plasma proteins to the particle's surface. This uptake may cause nanoparticles to be routed away from the site of its intended application and can greatly reduce the number of nanoparticles available to reach the target site, effectively reducing the efficacy of the nanoparticle-based system. To this end, there are critical considerations to keep in mind when designing nanomaterials for *in vivo* applications that ensures that the nanoparticle-based probes can be efficacious at lower doses which would lower costs and cause fewer deleterious effects [42].

1.16.1. Size and Shape

The translocation of nanostructures across biological barriers (e.g. plasma membrane) is critical in determining the potential and efficacy of nanomaterial-based systems when used in biomedical applications. Nanostructures of various sizes, shapes, and chemical compositions have been designed for potential uses in difference areas spanning from their drug delivery uses to therapy applications. The rate of particle uptake, clearances, and their biodistribution which ultimately determines the fate of nanoparticle carrier systems are to greatly depend on the size and geometrical shape of these nanostructures [139]. For instance, the particles in the range of 10-200 nm have been shown to have longer blood half life compared to smaller particles (< 20 nm) which cannot escape RES capture and thus cleared rapidly from the bloodstream. Additionally, larger nanostructures (> 500 nm) are known to be rapidly captured by macrophages which shorten the particle blood residence time. Particle size is a critical factor that should be considered when designing nanomaterials for different uses. Some application may be require designing particle systems where fast clearance is critical whereas other applications may require

longer blood residence time such as in time-release of therapeutics. Particle size also affects the mechanism of bloodstream clearance where smaller particles (sub 10nm) are have been shown to occur through renal clearance while larger particles (> 10 nm) occur through clearance by kupffer cells in liver.

Particle shape has also been implicated as a critical factor that affects the rate of cellular uptake which would determine its success in the intended application. Rod-shaped nanoparticles, owing to their larger longitudinal surface area, have been demonstrated to be taken up by cells at the rate higher than the rate of uptake of spherical nanoparticles of comparable size. This is because rod-shaped nanoparticles have larger contact area with the cell membrane receptors that increase the rate of particles receptor-mediated cell surface attachment and endocytosis [140].

1.16.2. Surface Modifications

Several studies have shown that biological responses to nanoparticles tend to scale with surface area rather than mass. As particle become smaller, their surface areas shrink much more slowly than their volumes, causing nanoscale materials to have far greater surface-to-volume ratios than larger particles. A larger surface-to-volume ratio also implies more proteins will bind a nanoparticle (relative to its mass) than a particle of larger size and that means the surface factors (such as charge and modification) can play a critical role. Components of the nanoparticle corona, called opsonins, may be recognized and capture by the the reticuloendothelial system (RES) e.g. the macrophage cells in the liver and can lead to faster clearance. The presence of opsonins on the particle surface creates a “molecular signature” which is recognized by immune cells and determines the route of particle internalization. The route of internalization, then, may affect the eventual fate of the nanoparticle in the body (i.e. its

rate of clearance from the bloodstream, volume of distribution, organ disposition, and rate and route of clearance from the body). The effect of this protein corona may have special significance for nanoparticles, due to the increased importance of surface effects for particles of this size. Even for larger particles protein binding is established as one of the most important factors influencing bio-distribution. In efforts to limit or avoid immune cells capture of the nanoparticle-based system, there are various types of surface modifications that are currently under studies.

One common method of evading the RES capture is by modifying the particle corona with "stealth" molecules to minimize the molecular signatures. One commonly used stealth molecule is polyethylene glycol (PEG). Surface modification with PEG - a hydrophilic molecule which helps prevent protein adsorption to the corona- has been shown to increase the half life of particles by reducing protein-particle interaction (opsonization), and thus reducing the degree of macrophage capture. There are also dextran-coated nanoparticles with longer blood half-life that have been FDA-approved for clinical applications.

1.16.3. Surface Charge

Along with size, surface charge (zeta potential) is a ubiquitous parameter that is important in designing nanostructures suitable for biomedical applications. Particles may be of appropriate size to traverse a desired biological barrier but effects of surface charge may, nonetheless, limit their efficacy. For each application, the particle surface charge should be rationally tuned to match the intended use. For instance, it has been shown that positively charged nanoparticles perform better for gene DNA delivery because of their ability to bind to negatively charged proteoglycans [141]. Nanostructures intended for prolonged blood life

circulation have been shown to be optimal when negatively charged or neutrally charged particles are used [138].

1.16.4. In vivo Barriers

In designing NPs for potential biomedical applications, it is critically important the particles are appropriately designed to overcome the intrinsic biological barriers such as RES systems that would keep them from reaching the intended target site. Biological barriers serve to protect the body against foreign entities, including injected therapeutics and contrast agents, but can restrict nanomaterials by blocking their movement, causing physical aggregation, or inducing a negative host response [142]. Upon intravascular administration, NPs immediately encounter blood, a high ionic strength, and heterogenous solution that can alter particles' properties and can lead to aggregation. Particles for cellular imaging or therapy should be designed to evade the RES system.

1.16.5. Physicochemical Considerations

NP pharmacokinetics and cellular uptake in vivo, including their ability to manage biological barriers, are largely related to NP physicochemical properties, including morphology, hydrodynamic size, charge, and other surface properties [143]. These properties are dictated by the types, structures, and orientations of the materials that comprise the SPIONs. Typically, a SPION consists of a magnetically active core coated with a stabilizing shell to which targeting ligands and additional imaging modalities are anchored. Therapeutic agents can then be embedded in the shell structure or chemically bonded to its surface. At each stage of its design,

the size, charge, hydrophobicity, shape, and orientation of the NP's constituent materials must be considered with regards to overall NP physiochemical properties.

REFERENCES

1. Alivisatos, A. P., Semiconductor Clusters, Nanocrystals, and Quantum Dots. *Science* **1996,** 271, (5251), 933-937.

2. El-Sayed, I. H.; Huang, X.; El-Sayed, M. A., Selective laser photo-thermal therapy of epithelial carcinoma using anti-egfr antibody conjugated gold nanoparticles. *Cancer lett.* **2005,** 239, (1), 129-135.

3. Link, S.; El-Sayed, M. A., Spectral Properties and Relaxation Dynamics of Surface Plasmon Electronic Oscillations in Gold and Silver Nanodots and Nanorods. *J. Phys. Chem. B* **1999,** 103, (40), 8410-8426.

4. Yguerabide, J.; Yguerabide, E. E., Light-Scattering Submicroscopic Particles as Highly Fluorescent Analogs and Their Use as Tracer Labels in Clinical and Biological Applications: I. Theory. *Anal. Biochem.* **1998,** 262, (2), 137-156.

5. Thompson, D. T., Using gold nanoparticles for catalysis. *Nano Today* **2007,** 2, (4), 40-43.

6. Lahav, M.; Vaskevich, A.; Rubinstein, I., Biological Sensing Using Transmission Surface Plasmon Resonance Spectroscopy. *Langmuir* **2004,** 20, (18), 7365-7367.

7. Jain, P. K.; Lee, K. S.; El-Sayed, I. H.; El-Sayed, M. A., Calculated Absorption and Scattering Properties of Gold Nanoparticles of Different Size, Shape, and Composition: Applications in Biological Imaging and Biomedicine. *J. Phys. Chem. B* **2006,** 110, (14), 7238-7248.

8. Trindade, T.; O'Brien, P.; Pickett, N. L., Nanocrystalline Semiconductors:Synthesis, Properties, and Perspectives. *Chem. Mater.* **2001,** 13, (11), 3843-3858.

9. Burda, C.; Chen, X.; Narayanan, R.; El-Sayed, M. A., Chemistry and Properties of Nanocrystals of Different Shapes. *Chem. Rev.* **2005,** 105, (4), 1025-1102.

10. Wagner, F. E.; Haslbeck, S.; Stievano, L.; Calogero, S.; Pankhurst, Q. A.; Martinek, K. P., Before striking gold in gold-ruby glass. *Nature* **2000,** 407, (6805), 691-692.

11. Murphy, C. J., Nanocubes and Nanoboxes. *Science* **2002,** 298, (5601), 2139-2141.

12. Bohren, C. F.; Huffman, D. R., *Absorption and Scattering of Light by Small Particles*. Wiley: New York, 1983.

13. Mie, G., *Ann. Phys* **1908,** 25, 377.

14. Creighton, J. A.; Eadon, D. G., Ultraviolet-visible absorption spectra of the colloidal metallic elements. *J. Chem. Soc. Faraday Trans.* **1991,** 87, (24), 3881-3891.

15. Huang, X.; Neretina, S.; El-Sayed, M. A., Gold Nanorods: From Synthesis and Properties to Biological and Biomedical Applications. *Adv. Mater.* **2009,** 21, (48), 4880-4910.

16. Kreibig, U.; Vollmer, M., *Optical Properties of Metal Clusters*. Springer: New York, **1995**.

17. Link, S.; El-Sayed, M. A., Shape and size dependence of radiative, non-radiative and photothermal properties of gold nanocrystals. *Int. Rev. Phys. Chem.* **2000,** 19, (3), 409 - 453.

18. Njoki, P. N.; Lim, I. I. S.; Mott, D.; Park, H.-Y.; Khan, B.; Mishra, S.; Sujakumar, R.; Luo, J.; Zhong, C.-J., Size Correlation of Optical and Spectroscopic Properties for Gold Nanoparticles. *J. Phys. Chem. C* **2007,** 111, (40), 14664-14669.

19. Gans, R., *Ann. Phys* **1915,** 352, (10), 270-284.

20. Brioude, A.; Jiang, X. C.; Pileni, M. P., Optical Properties of Gold Nanorods:DDA Simulations Supported by Experiments. *J. Phys. Chem. B* **2005,** 109, (27), 13138-13142.

21. Link, S.; El-Sayed, M. A., Optical Properties and Ultrafast Dynamics of Metallic Nanocrystals. *Ann. Rev. Phys. Chem.* **2003,** 54, (1), 331-366.

22. Sung, H. W. F.; Rudowicz, C., Physics behind the magnetic hysteresis loop--a survey of misconceptions in magnetism literature. *J. Magn. Magn. Mater.* **2003,** 260, (1-2), 250-260.

23. Jordan, A.; Wust, P.; Fahling, H.; John, W.; Hinz, A.; Felix, R., Inductive heating of ferrimagnetic particles and magnetic fluids: Physical evaluation of their potential for hyperthermia. *Int. J. Hyperthermia* **1993,** 9, 51-68.

24. Cunningham, C. H.; Arai, T.; Yang, P. C.; McConnell, M. V.; Pauly, J. M.; Conolly, S. M., Positive contrast magnetic resonance imaging of cells labeled with magnetic nanoparticles. *Magn. Reson. Med.* **2005,** 53, (5), 999-1005.

25. Anderson, S. A.; Rader, R. K.; Westlin, W. F.; Null, C.; Jackson, D.; Lanza, G. M.; Wickline, S. A.; Kotyk, J. J., Magnetic resonance contrast enhancement of neovasculature with α v β 3-targeted nanoparticles. *Magn. Reson. Med.* **2000,** 44, (3), 433-439.

26. Polyak, B.; Friedman, G., Magnetic targeting for site-specific drug delivery: applications and clinical potential. *Expert Opin. Drug Del.* **2009,** 6, (1), 53-70.

27. Jalilian, A. R.; Panahifar, A.; Mahmoudi, M.; Akhlaghi, M.; Simchi, A., Preparation and biological evaluation of [67Ga]-labeled-superparamagnetic nanoparticles in normal rats. *Radiochimica Acta* **2009,** 97, (1), 51-56.

28. Alexiou, C.; Arnold, W.; Klein, R. J.; Parak, F. G.; Hulin, P.; Bergemann, C.; Erhardt, W.; Wagenpfeil, S.; LÃ¼bbe, A. S., Locoregional Cancer Treatment with Magnetic Drug Targeting. *Cancer Res.* **2000,** 60, (23), 6641-6648.

29. Mosbach, K.; Schröder, U., Preparation and application of magnetic polymers for targeting of drugs. *FEBS Lett.* **1979,** 102, (1), 112-116.

30. Sneed, P. K.; Stea, B.; Seegenschmiedt, M. H.; Fessenden, P.; Vernon, C. C., *Thermoradiotherapy and thermochemotherapy*. Springer: Berlin, **1996**.

31. van Landeghem, F. K. H.; Maier-Hauff, K.; Jordan, A.; Hoffmann, K.-T.; Gneveckow, U.; Scholz, R.; Thiesen, B.; Brück, W.; von Deimling, A., Post-mortem studies in glioblastoma patients treated with thermotherapy using magnetic nanoparticles. *Biomaterials* **2009,** 30, (1), 52-57.

32. Jun, Y. W.; Choi, J.-S.; Cheon, J., Heterostructured magnetic nanoparticles: their versatility and high performance capabilities. *Chem. Commun.* **2006**, 1203-1214.

33. Wang, L.; Park, H. Y.; Lim, S. I.; Schadt, M. J.; Mott, D.; Luo, J.; Wang, X.; Zhong, C., Core@Shell nanomaterials: gold-coates magnetic nanoparticles. *J Mater Chem* **2008,** 18, 2629-35.

34. Yu, H.; Chen, M.; Rice, P. M.; Wang, S. X.; White, W. R. L.; Sun, S., Dumbbell-like Bifunctional Au-Fe3O4 Nanoparticles. *Nano Lett.* **2005,** 5, (2), 379-382.

35. Wang, C.; Chen, J.; Talavage, T.; Irudajaraj, J., Gold Nanorods/Fe3O4 "Nano-Pearl-Necklaces" for Simultaneous Targeting, Dual-Mode Imaging, and Photothermal Ablation of Cancer Cells. *Angew. Chem. Int. Ed.* **2009,** 48, 2759-63.

36. Maier-Hauff, K.; Rothe, R.; Scholz, R.; Gneveckow, U.; Wust, P.; Thiesen, B.; Feussner, A.; von Deimling, A.; Waldoefner, N.; Felix, R.; Jordan, A., Intracranial Thermotherapy using Magnetic Nanoparticles Combined with External Beam Radiotherapy: Results of a Feasibility Study on Patients with Glioblastoma Multiforme. *J. Neuro-Oncol.* **2007,** 81, (1), 53-60.

37. *American Cancer Society report*; **2011**.

38. Stein, G. S.; Pardee, A. B., *Cell cycle and growth control: biomolecular regulation and cancer*. Wiley-Liss.: NJ, **2004**.

39. Lodish, H.; Berk, A.; Zipursky, L. S.; Matsudaira, P.; Baltimore, D.; Darnell, J., *Molecular Cell Biology*. W.H. FREEMAN: **2004**.

40. Heath, J. K.; White, S. J.; Johnstone, C. N.; Catimel, B.; Simpson, R. J.; Moritz, R. L.; Tu, G.-F.; Ji, H.; Whitehead, R. H.; Groenen, L. C.; Scott, A. M.; Ritter, G.; Cohen, L.; Welt, S.; Old, L. J.; Nice, E. C.; Burgess, A. W., The human A33 antigen is a transmembrane glycoprotein and a novel member of the immunoglobulin superfamily. *Proc. Natl. Acad. Sci.* **1997,** 94, (2), 469-474.

41. Veronese, M. L.; O'Dwyer, P. J., Monoclonal antibodies in the treatment of colorectal cancer. *Europ. J. Cancer* **2004,** 40, (9), 1292-1301.

42. Douillard, J. Y.; Cunningham, D.; Roth, A. D.; Navarro, M.; James, R. D.; Karasek, P.; Jandik, P.; Iveson, T.; Carmichael, J.; Alakl, M.; Gruia, G.; Awad, L.; Rougier, P., Irinotecan combined with fluorouracil compared with fluorouracil alone as first-line treatment for metastatic colorectal cancer: a multicentre randomised trial. *The Lancet* **2000,** 355, (9209), 1041-1047.

43. Schwartzberg, L. S., Clinical experience with edrecolomab: a monoclonal antibody therapy for colorectal carcinoma. *Crit. Rev. Oncology/Hematology* **2001,** 40, (1), 17-24.

44. Kabbinavar, F.; Hurwitz, H. I.; Fehrenbacher, L.; Meropol, N. J.; Novotny, W. F.; Lieberman, G.; Griffing, S.; Bergsland, E., Phase II, Randomized Trial Comparing Bevacizumab Plus Fluorouracil (FU)/Leucovorin (LV) With FU/LV Alone in Patients With Metastatic Colorectal Cancer. *J. Clinic. Oncol.* **2003,** 21, (1), 60-65.

45. Ackerman, M.; Chalouni, C.; Schmidt, M.; Raman, V.; Ritter, G.; Old, L.; Mellman, I.; Wittrup, K., A33 antigen displays persistent surface expression. *Cancer Immunol. Immunother.* **2008,** 57, (7), 1017-1027.

46. Genentech, Research reports. In **2011**.

47. Brioude, A.; Jiang, X. C.; Pileni, M. P., Optical Properties of Gold Nanorods:â€‰ DDA Simulations Supported by Experiments. *J. Phys. Chem. B* **2005,** 109, (27), 13138-13142.

48. Harari, P. M.; Huang, S. M.; Herbst, R.; Quon, H., *Molecular targeting of the epidermal growth factor in head and neck cancer. In Head and Neck Cancer: a Multidisciplinary Approach*. Lippincott, Williams and Wilkins: Philadelphia, PA, **2003**; p 1001-1016.

49. Trikha, M.; Yan, L.; Nakada, M. T., Monoclonal antibodies as therapeutics in oncology. *Curr. Opin. Biotechn.* **2002,** 13, (6), 609-614.

50. Verhaar, M. J.; Chester, K. A.; Keep, P. A.; Robson, L.; Pedley, R. B.; Boden, J. A.; Hawkins, R. E.; Begent, R. H. J., A single chain Fv derived from a filamentous phage library has distinct tumour targeting advantages over one derived from a hybridoma. *Int. J. Cancer* **1995,** 61, (4), 497-501.

51. Mayer, A.; Tsiompanou, E.; Oâ€™Malley, D.; Boxer, G. M.; Bhatia, J.; Flynn, A. A.; Chester, K. A.; Davidson, B. R.; Lewis, A. A. M.; Winslet, M. C.; Dhillon, A. P.; Hilson, A. J. W.; Begent, R. H. J., Radioimmunoguided Surgery in Colorectal Cancer Using a Genetically Engineered Anti-CEA Single-Chain Fv Antibody. *Clin. Cancer Res.* **2000,** 6, (5), 1711-1719.

52. Welt, S.; Ritter, G.; Williams, C.; Cohen, L. S.; John, M.; Jungbluth, A.; Old, E. A., Phase I Study Anticolon Cancer Humanized Antibody A33. *Clin. Cancer Res.* **2003,** 9, 1338-1346.

53. Damasceno, L.; Pla, I.; Chang, H. J.; Cohen, L.; Ritter, G.; Old, L. J.; Batt, C. A., An optimized fermentation process for high-level production of a single-chain antibody fragment in Pichia pastoris. *Protein Expr. Purif.* **2004,** 37, 18-26.

54. Yamamoto, M.; Kashiwagi, Y.; Sakata, T.; Mori, H.; Nakamoto, M., Synthesis and Morphology of Star-Shaped Gold Nanoplates Protected by Poly(N-vinyl-2-pyrrolidone). *Chem. Mater.* **2005,** 17, (22), 5391-5393.

55. Wu, X.; Liu, H.; Liu, J.; Haley, K. N.; Treadway, J. A.; Larson, J. P.; Ge, N.; Peale, F.; Bruchez, M. P., Immunofluorescent labeling of cancer marker Her2 and other cellular targets with semiconductor quantum dots. *Nat. Biotechnol.* **2003,** 21, 41.

56. Nikoobakht, B.; El-sayed, M. A., Preparation and growth Mechanism of Gold Nanorods (NRs) Using Seed-Mediated Growth Method. *Chem. Mater.* **2003,** 15, 1957-62.

57. McCarthy, J. R.; Bhaumik, J.; Karver, M. R.; Sibel Erdem, S.; Weissleder, R., Targeted nanoagents for the detection of cancers. *Molecular Oncol.* **2010,** 4, (6), 511-528.

58. Veiseh, O.; Gunn, J. W.; Zhang, M., Design and fabrication of magnetic nanoparticles for targeted drug delivery and imaging. *Adv. Drug Del. Rev.* **2010,** 62, (3), 284-304.

59. Santra, S.; Zhang, P.; Wang, K.; Tapec, R.; Tan, W., Conjugation of Biomolecules with Luminophore-Doped Silica Nanoparticles for Photostable Biomarkers. *Anal. Chem.* **2001,** 73, (20), 4988-4993.

60. Noone, K. M.; Ginger, D. S., Doping for Speed: Colloidal Nanoparticles for Thin-Film Optoelectronics. *ACS Nano* **2009,** 3, (2), 261-265.

61. Nie, S.; Emory, S. R., Probing Single Molecules and Single Nanoparticles by Surface-Enhanced Raman Scattering. *Science* **1997,** 275, (5303), 1102-1106.

62. Calvo, P.; Gouritin, B.; Chacun, H.; Desmaële, D.; D'Angelo, J.; Noel, J.-P.; Georgin, D.; Fattal, E.; Andreux, J. P.; Couvreur, P., Long-Circulating PEGylated Polycyanoacrylate Nanoparticles as New Drug Carrier for Brain Delivery. *Pharm. Res.* **2001,** 18, (8), 1157-1166.

63. Panyam, J.; Labhasetwar, V., Sustained Cytoplasmic Delivery of Drugs with Intracellular Receptors Using Biodegradable Nanoparticles. *Mol. Pharmaceutics* **2003,** 1, (1), 77-84.

64. Dubertret, B.; Skourides, P.; Norris, D. J.; Noireaux, V.; Brivanlou, A. H.; Libchaber, A., In vivo Imaging of Quantum Dots Encapsulated in Phospholipid Micelles. *Science* **2002,** 298, (5599), 1759-1762.

65. Hadjipanayis, C. G.; Bonder, M. J.; Hadjipanayis, G. G., Metallic Iron nanoparticles for MRI contrast enhancement and local hyperthermia. *Small* **2008,** 5, 1-5.

66. Huang, Y.-F.; Sefah, K.; Bamrungsap, S.; Chang, H.-T.; Tan, W., Selective Photothermal Therapy for Mixed Cancer Cells Using Aptamer-Conjugated Nanorods. *Langmuir* **2008,** 24, (20), 11860-11865.

67. Kong, G.; Braun, R. D.; Dewhirst, M. W., Hyperthermia Enables Tumor-specific Nanoparticle Delivery: Effect of Particle Size. *Cancer Res.* **2000,** 60, (16), 4440-45.

68. Rusinek, H.; Naidich, D. P.; McGuinness, G.; Leitman, B. S.; McCauley, D. I.; Krinsky, G. A.; Clayton, K.; Cohen, H., Pulmonary nodule detection: low-dose versus conventional CT. *Radiology* **1998,** 209, (1), 243-249.

69. Mulkern, R. V.; Robertson, R. L.; Packard, A. B., Contrast Agents in Neuroradiological MRI: Current Status. In *Handbook of Neuro-Oncology NeuroImaging*, Academic Press: San Diego, **2008**; pp 150-157.

70. Wikipedia, Information on iron oxide-based contrast agents. In *http://en.wikipedia.org/wiki/MRI_contrast_agen*t, **2011**.

71. Reimer, P.; Tombach, B., Hepatic MRI with SPIO: detection and characterization of focal liver lesions. *Eur. Radiol.* **1998,** 8, (7), 1198-1204.

72. Sun, C.; Lee, J. S. H.; Zhang, M., Magnetic nanoparticles in MR imaging and drug delivery. *Adv. Drug Del.Rev.* **2008,** 60, (11), 1252-1265.

73. Elsherbini, A. A. M.; Saber, M.; Aggag, M.; El-Shahawy, A.; Shokier, H. A. A., Magnetic nanoparticle-induced hyperthermia treatment under magnetic resonance imaging. *Magn. Reson. Imaging* **2011,** 29, (2), 272-280.

74. Medarova, Z.; Pham, W.; Farrar, C.; Petkova, V.; Moore, A., In vivo imaging of siRNA delivery and silencing in tumors. *Nat Med* **2007,** 13, (3), 372-377.

75. Jain, T. K., Reddy, M.K., Morales, M.A., Leslie-Pelecky, D.L., Labhasetwar, V., Biodistribution, Clearance, and Biocompatibility of Iron Oxide Magnetic Nanoparticles in Rats. *Mol. Pharmaceutics* **2007,** 5, (2), 12.

76. Mahmoudi, M., Simchi, A., Milani, A.S., Stroeve, P. , Cell toxicity of superparamagnetic iron oxide nanoparticles. *J. Colloid Interf. Sci.* **2009,** 336, 510-518.

77. Mahmoudi, M., Simchi, A., Vali, H., Imani, M., Shokrgozar, M.A., Azadmanesh, K., Azari, F., Cytotoxicity and Cell Cycle Effects of Bare and Poly(vinyl alcohol)-Coated Iron Oxide Nanoparticles in Mouse Fibroblasts. *Adv. Eng. Mater.* **2009,** 11, (12), 243-250.

78. Mahmoudi, M., Simchi, A., Imani, M., Cytotoxicity of Uncoated and Polyvinyl Alcohol Coated Superparamagnetic Iron Oxide Nanoparticles. *J. Phys. Chem. C* **2009,** 113, (22), 9573-9580.

79. Mahmoudi, M., Simchi, A., Imani, M., Shokrgozar, M.A., Milani, A.S., Hafeli, U.O., Stroeve, P. , A new approach for the *in vitro* identification of the cytotoxicity of superparamagnetic iron oxide nanoparticles. *Colloid Surf. B: Biointerf.* **2010,** 75, 300-309.

80. Berry, C. C. C., A.S.G., Functionalisation of magnetic nanoparticles for applications in biomedicine. *J. Phys. D: Appl. Phys.* **2003,** 36, R198-R206.

81. Lu, A.-H., Salabas, E.L., Schuth, F., Magnetic Nanoparticles: Synthesis, Protection, Functionalization, and Application. *Angew. Chem. Int. Ed.* **2007,** 46, 1222-1244.

82. Moore, G. E.; Peyton, W. T.; French, L. A.; Walker, W. W., The clinical use of fluorescein in neurosurgery; the localization of brain tumors. *J. Neurosurg.* **1948,** 5, 392-398.

83. Simberg, D.; Duza, T.; Park, J. H.; Essler, M.; Pilch, J.; Zhang, L.; Derfus, A. M.; Yang, M.; Hoffman, R. M.; Bhatia, S.; Sailor, M. J.; Ruoslahti, E., Biomimetic amplification of nanoparticle homing to tumors. *Proc. Natl. Acad. Sci.* **2007,** 104, (3), 932-936.

84. Kelly, K. A.; Setlur, S. R.; Ross, R.; Anbazhagan, R.; Waterman, P.; Rubin, M. A.; Weissleder, R., Detection of Early Prostate Cancer Using a Hepsin-Targeted Imaging Agent. *Cancer Res.* **2008,** 68, (7), 2286-2291.

85. Biju, V.; Mundayoor, S.; Omkumar, R. V.; Anas, A.; Ishikawa, M., Bioconjugated quantum dots for cancer research: Present status, prospects and remaining issues. *Biotechnol. Adv.* **2010,** 28, (2), 199-213.

86. Park, J. H.; Maltzahn, G. V.; Sangeeta, B. H.; Ruoslahti, E.; Bhatia, S. N.; Sailor, M. J., Micellar Hybrid Nanoparticles for Simultaneous Magnetofluorescent Imaging and Drug Delivery. *Angew. Chem. Int. Ed.* **2008,** 47, 1-6.

87. Popovtzer, R.; Agrawal, A.; Kotov, N. A.; Popovtzer, A.; Balter, J.; Carey, T. E.; Kopelman, R., Targeted Gold Nanoparticles Enable Molecular CT Imaging of Cancer. *Nano Lett.* **2008,** 8, (12), 4593-4596.

88. Hainfeld, J. F.; Slatkin, D. N.; Focella, T. M.; Smilowitz, H. M., Gold nanoparticles: a new X-ray contrast agent. *Br J Radiol* **2006,** 79, (939), 248-253.

89. Connor, E. E.; Mwamuka, J.; Gole, A.; Murphy, C. J.; Wyatt, M. D., Gold Nanoparticles Are Taken Up by Human Cells but Do Not Cause Acute Cytotoxicity. *Small* **2005,** 1, (3), 325-327.

90. Warsi, M. F.; Adams, R. W.; Duckett, S. B.; Chechik, V., Gd-functionalized Au nanoparticles as targeted contrast agents in MRI: relaxivity enhancement by polyelectrolyte coating. *Chem. Commun.* **2010,** 46, (3), 451-453.

91. Rabin, O.; Manuel Perez, J.; Grimm, J.; Wojtkiewicz, G.; Weissleder, R., An X-ray computed tomography imaging agent based on long-circulating bismuth sulphide nanoparticles. *Nat Mater* **2006,** 5, (2), 118-122.

92. Huang, X.; El-Sayed, M. A., Gold nanoparticles: Optical properties and implementations in cancer diagnosis and photothermal therapy. *J. Adv. Res.* **2010,** 1, (1), 13-28.

93. Pitsillides, C. M.; Joe, E. K.; Wei, X.; Anderson, R. R.; Lin, C. P., Selective Cell Targeting with Light-Absorbing Microparticles and Nanoparticles. *Biophysical J.* **2003,** 84, (6), 4023-4032.

94. Zharov, V. P.; Kim, J.-W.; Curiel, D. T.; Everts, M., Self-assembling nanoclusters in living systems: application for integrated photothermal nanodiagnostics and nanotherapy. *Nanomed.: Nanotech. Biol. Med.* **2005,** 1, (4), 326-345.

95. Terentyuk, G. S.; Maslyakova, G. N.; Suleymanova, L. V.; Khlebtsov, N. G.; Khlebtsov, B. N.; Akchurin, G. G.; Maksimova, I. L.; Tuchin, V. V., Laser-induced tissue hyperthermia mediated by gold nanoparticles: toward cancer phototherapy. *J. Biomed. Optics* **2009,** 14, (2), 021016-9.

96. Pissuwan, D.; Cortie, C. H.; Valenzuela, S. M.; Cortie, M. B., Gold nanosphere-antibody conjugates for hyperthermal therapeutic applications. *Gold Bull* **2007,** 40, (2), 121-9.

97. Huang, X.; El-Sayed, I. H.; Qian, W.; El-Sayed, M. A., Cancer Cell Imaging and Photothermal Therapy in the Near-Infrared Region by Using Gold Nanorods. *J. Am. Chem. Soc.* **2006,** 128, (6), 2115-2120.

98. Prencipe, G.; Tabakman, S. M.; Welsher, K.; Liu, Z.; Goodwin, A. P.; Zhang, L.; Henry, J.; Dai, H., PEG Branched Polymer for Functionalization of Nanomaterials with Ultralong Blood Circulation. *J. Am. Chem. Soc.* **2009,** 131, (13), 4783-4787.

99. Sakamoto, M.; Fujistuka, M.; Majima, T., Light as a construction tool of metal nanoparticles: Synthesis and mechanism. *J. Photochem. and Photobiol. C: Photochem. Rev.* **2009,** 10, (1), 33-56.

100. Wang, J.; Wang, L.; Liu, X.; Liang, Z.; Song, S.; Li, W.; Li, G.; Fan, C., A Gold Nanoparticle-Based Aptamer Target Binding Readout for ATP Assay. *Adv. Mater.* **2007,** 19, (22), 3943-3946.

101. Capek, I., Preparation of metal nanoparticles in water-in-oil (w/o) microemulsions. *Adv. Colloid Interface Sci.* **2004,** 110, (1-2), 49-74.

102. Birtcher, R. C.; Donnelly, S. E.; Schlutig, S., Nanoparticle ejection from gold during ion irradiation. *Nucl. Instrum. Methods in Phys. Res. B* **2004,** 215, (1-2), 69-75.

103. Lung, J.-K.; Huang, J.-C.; Tien, D.-C.; Liao, C.-Y.; Tseng, K.-H.; Tsung, T.-T.; Kao, W.-S.; Tsai, T.-H.; Jwo, C.-S.; Lin, H.-M.; Stobinski, L., Preparation of gold nanoparticles by arc discharge in water. *J. Alloys Compd.* **2007,** 434-435, 655-658.

104. Nguyen, D. T.; Kim, D.-J.; Kim, K.-S., Controlled synthesis and biomolecular probe application of gold nanoparticles. *Micron* **2011,** 42, (3), 207-227.

105. Kimling, J.; Maier, M.; Okenve, B.; Kotaidis, V.; Ballot, H.; Plech, A., Turkevich Method for Gold Nanoparticle Synthesis Revisited. *J. Phys. Chem. B* **2006,** 110, (32), 15700-15707.

106. Jana, N. R.; Gearheart, L.; Murphy, C. J., Seeding Growth for Size Control of 5â˜’40 nm Diameter Gold Nanoparticles. *Langmuir* **2001,** 17, (22), 6782-6786.

107. Hu, J.; Zhang, Y.; Liu, B.; Liu, J.; Zhou, H.; Xu, Y.; Jiang, Y.; Yang, Z.; Tian, Z.-Q., Synthesis and Properties of Tadpole-Shaped Gold Nanoparticles. *J. Am. Chem. Soc.* **2004,** 126, (31), 9470-9471.

108. Kuo, C.-H.; Huang, M. H., Synthesis of Branched Gold Nanocrystals by a Seeding Growth Approach. *Langmuir* **2005,** 21, (5), 2012-2016.

109. Sau, T. K.; Murphy, C. J., Room Temperature, High-Yield Synthesis of Multiple Shapes of Gold Nanoparticles in Aqueous Solution. *J. Am. Chem. Soc.* **2004,** 126, (28), 8648-8649.

110. Zijlstra, P.; Bullen, C.; Chon, J. W. M.; Gu, M., High-Temperature Seedless Synthesis of Gold Nanorods. *J. Phys. Chem. B* **2006,** 110, (39), 19315-19318.

111. Abdelsayed, V.; Panda, A. B.; Glaspell, G. P.; El Shall, M. S., Synthesis, Passivation, and Stabilization of Nanoparticles, Nanorods, and Nanowires by Microwave Irradiation. In *Nanoparticles: Synthesis, Stabilization, Passivation, and Functionalization*, ACS: **2008**; 996, 225-247.

112. Orendorff, C. J.; Hankins, P. L.; Murphy, C. J., pH-Triggered Assembly of Gold Nanorods. *Langmuir* **2005,** 21, (5), 2022-2026.

113. Ahmed, M.; Narain, R., Rapid Synthesis of Gold Nanorods Using a One-Step Photochemical Strategy. *Langmuir* **2010,** 26, (23), 18392-18399.

114. Gole, A.; Murphy, C. J., Polyelectrolyte-Coated Gold Nanorods:Synthesis, Characterization and Immobilization. *Chem. Mater.* **2005,** 17, (6), 1325-1330.

115. Gorelikov, I.; Matsuura, N., Single-Step Coating of Mesoporous Silica on Cetyltrimethyl Ammonium Bromide-Capped Nanoparticles. *Nano Lett.* **2007,** 8, (1), 369-373.

116. Mortier, T.; Persoons, A.; Verbiest, T., Two-step synthesis of high aspect ratio gold nanorods. *Cent. Eur. J. Chem.* **2006,** 4, (1), 160-165.

117. Sun, X.; Luo, Y., Synthesis of gold microplates and polyhedral nanoparticles. *Mater. Lett.* **2006,** 60, (24), 2988-2990.

118. Gupta, A. K.; Gupta, M., Synthesis and surface engineering of iron oxide nanoparticles for biomedical applications. *Biomaterials* **2005,** 26, (18), 3995-4021.

119. Kim, D. K.; Zhang, Y.; Voit, W.; Rao, K. V.; Muhammed, M., Synthesis and characterization of surfactant-coated superparamagnetic monodispersed iron oxide nanoparticles. *J. Magn. Magn. Mater.* **2001,** 225, (1-2), 30-36.

120. Sun, S.; Zeng, H., Size-Controlled Synthesis of Magnetite Nanoparticles. *J. Am. Chem. Soc* **2002,** 124, 8204-8205.

121. Aryal, S.; B.K.C, R.; Dharmaraj, N.; Bhattarai, N.; Kim, C. H.; Kim, H. Y., Spectroscopic identification of SAu interaction in cysteine capped gold nanoparticles. *Spectrochim. Acta Part A* **2006,** 63, (1), 160-163.

122. Yoo, C. I.; Seo, D.; Chung, B. H.; Chung, I. S.; Song, H., A Facile One-Pot Synthesis of Hydroxyl-Functionalized Gold Polyhedrons by a Surface Regulating Copolymer. *Chem. Mater.* **2009,** 21, (5), 939-944.

123. Shem, P. M.; Sardar, R.; Shumaker-Parry, J. S., One-Step Synthesis of Phosphine-Stabilized Gold Nanoparticles Using the Mild Reducing Agent 9-BBN. *Langmuir* **2009,** 25, (23), 13279-13283.

124. Ding, Y.; Zhang, X.; Liu, X.; Guo, R., Adsorption Characteristics of Thionine on Gold Nanoparticles. *Langmuir* **2006,** 22, (5), 2292-2298.

125. Goren, M.; Galley, N.; Lennox, R. B., Adsorption of Alkylthiol-Capped Gold Nanoparticles onto Alkylthiol Self-Assembled Monolayers: An SPR Study. *Langmuir* **2005,** 22, (3), 1048-1054.

126. Chechik, V.; Crooks, R. M., Monolayers of Thiol-Terminated Dendrimers on the Surface of Planar and Colloidal Gold. *Langmuir* **1999,** 15, (19), 6364-6369.

127. Zhou, J.; Beattie, D. A.; Ralston, J.; Sedev, R., Colloid Stability of Thymine-Functionalized Gold Nanoparticles. *Langmuir* **2007,** 23, (24), 12096-12103.

128. Aili, D.; Enander, K.; Baltzer, L.; Liedberg, B., Assembly of Polypeptide-Functionalized Gold Nanoparticles through a Heteroassociation- and Folding-Dependent Bridging. *Nano Lett.* **2008,** 8, (8), 2473-2478.

129. Weare, W. W.; Reed, S. M.; Warner, M. G.; Hutchison, J. E., Improved Synthesis of Small (dCORE ~ 1.5 nm) Phosphine-Stabilized Gold Nanoparticles. *J. Am. Chem. Soc.* **2000,** 122, (51), 12890-12891.

130. Wang, X.; Kawanami, H.; Islam, N. M.; Chattergee, M.; Yokoyama, T.; Ikushima, Y., Amphiphilic block copolymer-stabilized gold nanoparticles for aerobic oxidation of alcohols in aqueous solution. *Chem. Commun.* **2008**, (37), 4442-4444.

131. Rey, D. A.; Strickland, A. D.; Kirui, D.; Niamsiri, N.; Batt, C. A., In vitro Self-Assembly of Gold Nanoparticle-Coated Poly(3-hydroxybutyrate) Granules Exhibiting Plasmon-Induced Thermo-Optical Enhancements. *ACS Appl. Mater. Interf.* **2010,** 2, (7), 1804-1810.

132. Graf, C.; Vossen, D. L. J.; Imhof, A.; van Blaaderen, A., A General Method To Coat Colloidal Particles with Silica. *Langmuir* **2003,** 19, (17), 6693.

133. Sun, C.; Lee, J. S. H.; Zhang, M., Magnetic nanoparticles in MR imaging and drug delivery. *Adv. Drug Del. Rev.* **2008,** 60, (11), 1252-1265.

134. Weissleder, R.; Bogdanov, A.; Neuwelt, E. A.; Papisov, M., Long-circulating iron oxides for MR imaging. *Adv. Drug Del. Rev.* **1995,** 16, (2-3), 321-334.

135. Shen, T.; Weissleder, R.; Papisov, M.; Bogdanov, A.; Brady, T. J., Monocrystalline iron oxide nanocompounds (MION): Physicochemical properties. *Magn. Reson. Med.* **1993,** 29, (5), 599-604.

136. Gref, R.; Lück, M.; Quellec, P.; Marchand, M.; Dellacherie, E.; Harnisch, S.; Blunk, T.; Müller, R. H., 'Stealth' corona-core nanoparticles surface modified by polyethylene glycol (PEG): influences of the corona (PEG chain length and surface density) and of the core composition on phagocytic uptake and plasma protein adsorption. *Colloid Surf. B: Biointerf.* **2000,** 18, (3-4), 301-313.

137. Zhang, Y.; Kohler, N.; Zhang, M., Surface modification of superparamagnetic magnetite nanoparticles and their intracellular uptake. *Biomaterials* **2002,** 23, (7), 1553-1561.

138. Aggarwal, P.; Hall, J. B.; McLeland, C. B.; Dobrovolskaia, M. A.; McNeil, S. E., Nanoparticle interaction with plasma proteins as it relates to particle biodistribution, biocompatibility and therapeutic efficacy. *Adv. Drug Del. Rev.* **2009,** 61, (6), 428-437.

139. Zhang, K.; Fang, H.; Chen, Z.; Taylor, J.-S. A.; Wooley, K. L., Shape Effects of Nanoparticles Conjugated with Cell-Penetrating Peptides (HIV Tat PTD) on CHO Cell Uptake. *Bioconjug. Chem.* **2008,** 19, (9), 1880-1887.

140. Chithrani, B. D.; Ghazani, A. A.; Chan, W. C. W., Determining the Size and Shape Dependence of Gold Nanoparticle Uptake into Mammalian Cells. *Nano Lett.* **2006,** 6, (4), 662-668.

141. Adler, A. F.; Leong, K. W., Emerging links between surface nanotechnology and endocytosis: Impact on nonviral gene delivery. *Nano Today* **2010,** 5, (6), 553-569.

142. Belting, M.; Sandgren, S.; Wittrup, A., Nuclear delivery of macromolecules: barriers and carriers. *Adv. Drug Del. Rev.* **2005,** 57, (4), 505-527.

143. Dobrovolskaia, M. A.; Aggarwal, P.; Hall, J. B.; McNeil, S. E., Preclinical Studies To Understand Nanoparticle Interaction with the Immune System and Its Potential Effects on Nanoparticle Biodistribution. *Mol. Pharmaceutics* **2008,** 5, (4), 487-495.

Chapter 2

Gold hybrid nanoparticles for targeted phototherapy and cancer imaging

Abstract:
Gold and iron oxide hybrid nanoparticles (HNPs) synthesized by thermal decomposition technique are bio-functionalized with single chain antibody, scFv, that binds to the A33 antigen present on colorectal cancer cells. The HNPs-scFv conjugates are stable in aqueous solution with magnetization value of 44 emu/g rate and exhibit strong optical absorbance at 800 nm. Here we test this material in targeting, imaging and selective thermal killing of colorectal cancer cells. Cellular uptake studies showed that A33-expressing cells take up the A33scFv conjugated HNPs at a rate five-times higher than cells that do not express the A33 antigen. Laser irradiation studies showed that approximately 53% of the A33-expressing cells exposed to targeted HNPs are killed after a six-minute laser treatment at 5.1 W cm^{-2} using a 808 nm continuous wave laser diode while < 5% of A33-nonexpressing cells are killed. At a higher intensity, 31.5 W cm^{-2}, the thermal destruction increases to 99% and 40% for A33-expressing cells and A33 non-expressing cells, respectively after 6-min exposure. Flow cytometric analyses of the laser-irradiated A33 antigen-expressing cells show that apoptosis-related cell death to be the primary of mode of cell death at 5.1 W cm^{-2} with increasing necrotic-related cell death at higher laser power. These results suggest that this new class of bio-conjugated hybrid nanoparticles can potentially serve as

an effective antigen-targeted photothermal therapeutic agent for cancer treatment as well as a probe for magnetic resonance-based imaging.

There has been a great deal of interest devoted to the development of nanomaterials for photothermal therapy that can be used in minimally-invasive selective cancer treatment. This type of therapy utilizes the large absorption band of nanomaterials in the near infrared (NIR) region [1]. Absorption in the NIR region is desirable owing to the weak absorption by tissues which can penetrate the skin with less risk of thermal injury to normal tissues, and thus, can be used to treat specific cells targeted by the nanomaterials [1]. Nanomaterials that strongly absorb NIR irradiation include: gold spherical particles [1, 2], gold nanocages [3], gold nanorods [4], and single-walled carbon nanotubes [5] all of which have been demonstrated to have potential therapeutic applications. These types of materials can convert absorbed photons into thermal energy, causing cell destruction as a result of electron-phonon and phonon-phonon processes [1] and the use of these gold-nanostructured materials have shown promise as photothermal therapeutic agents both *in vitro* [1] and *in vivo* [6].

The potential benefits of integrating nanomaterials with different properties (such as magnetization, fluorescence, and near-infrared absorption) into a single object of nanoscale dimensions can lead to the development of multifunctional nanomedical platforms for simultaneous targeting, imaging, and therapy administration [7, 8]. These efforts have spurred the developments of various types of hybrid nanoparticle systems such as hybrids of iron oxide-quantum dots [9], and various types of gold nanoparticle-iron oxide hybrids [10-12]. For example Kim and coworkers reported multifunctional nanoparticles that exhibit both magnetic and optical properties with potential use for simultaneous targeted phototherapy and imaging using magnetic resonance imaging (MRI) [2]. Iron oxide nanoparticles such as superparamagnetic iron oxide (SPIO) nanoparticles, have been extensively utilized as MRI contrast agents to image target

tissues *in vivo* in a highly specific manner [13-15]. The SPIO nanoparticles modified with tumor-targeting ligands were used as *in vivo* MRI contrast agents [16] and to induce cell apoptosis via hyperthermia [17].

For cancer targeting, high specificity is generally introduced by taking advantage of the physiological differences between malignant and normal cells. Nanoparticles conjugated to cancer targeting agents have been used for site specific delivery of drugs and therapeutics [18]. This has been shown to significantly reduce drug toxicity and localize therapeutic impact [19]. Achieving specific targeting is particularly important when it comes to laser irradiation for medical applications. It is critical to reduce the energy level to abide by medical safety standard and this has been demonstrated by the use of the targeting agents to reduce the laser power needed to achieve therapeutic effects in cancers. Humanized single chain antibody (A33scFv) is one example of such targeting agent. It is known to bind to a transmembrane glycoprotein, A33 antigen, which is expressed in 95% of primary and metastatic human colorectal tumor cells [20], but is absent in most other normal tissues and tumor types [21]. A33 is not secreted or shed into the bloodstream and some colon cancer cell lines express large amounts of this antigen, binding almost 10^6 mAb molecules/cell [22]. Consequently, the A33 antigenic system is the focus of several clinical studies in patients with colon cancers [20, 22]. The A33scFv has recently been optimized and produced in our laboratory under the Cornell University/ Ludwig Institute for Cancer Research Partnership [23]. It has been recently conjugated to the surface of 5-nm gold nanoparticles encapsulated in novel diblock copolymers [24]. In this work, we utilized the clinically relevant A33scFv covalently-bound to HNPs to achieve specific targeting of A33-expresssing colorectal cancer cells and to minimize damage to healthy surrounding cells.

Here, we report on novel dumbbell-like nanoparticles that have both magnetic and optical properties and are additionally conjugated to a targeting antigen, integrating therapeutic (photothermal therapy) and imaging functions (MRI and fluorescence) into a single nanoscale probe. The dumbbell-like nanoparticles have several distinct advantages over previously reported materials used for photothermal therapy that individually lack one or more of the characteristics of our particles [1, 25].

2. Experimental and Methods

2.1. Materials

All of the chemicals were of reagent grade and were used without further purification. Iron(III) acetylacetonate (≥ 99.9%), 1-octadecene (90%), oleylamine, 1,2-tetradecanediol (90%), oleic acid (technical grade, 90%), gold (III) chloride, 1,2,3,4-tetrahydronaphthalene (reagent grade, 97%), iron pentacarbonyl (≥ 99.9%), dimethyl sulfoxide (DMSO), and Albumin, Bovine (BSA) were purchased from Sigma-Aldrich; 1,2 Distearoyl-sn-glycero-3-phosphoethanolamine-N-[Carboxyl (polyethylene glycol) 2000] ammonium salt (DSPEG-PEG COOH 2000) was purchased from Avanti Polar Lipids; N-hydroxylsulfosuccinimide (Sulfo-NHS), 1-Ethyl-3-(3-dimethylaminopropyl carboiimide HCl (EDC) were purchased from Pierce Biotechnology; Alexa Fluor 488 and 3-(4,5-dimethylthiazol-2-yl)-2,5-diphenyltetrazolium bromide (MTT) cell proliferation assay kit were purchased from Invitrogen; Annexin-V fluorescein isothiocyanate (FITC)/ propidium iodide (PI) detection kit and calcien AM stain from BD Biosciences, PharMingen; SW1222 cells (antigen expressing colorectal cancer) and non-malignant cell lines HT29 cells were received as a gift from Ludwig Cancer institute of Cancer

Research, (New York, NY); A33 single chain antibody was expressed in *Pichia pastoris* as previously reported [23].

2.2. Nanoparticle Preparation

The dumbbell-like Au-Fe_3O_4 nanoparticles were fabricated as previously described by Yu et *al* [26]. Briefly, 0.2 mmol gold (III) chloride solution in toluene was injected into a 4 mmol iron precursor, $Fe(CO)_5$, in presence of 12 mmol oleic acid and 12 mmol oleylamine and then heated to reflux (~ 310^{o}C) for 45 min. The size of the Au nanoparticles was tuned by controlling the temperature at which gold (III) chloride solution was injected into the mixture or by controlling the Au $(Cl)_3$/oleylamine ratio. For example, injecting the Au precursor at 180^{o}C led to the formation of 6 nm Au nanoparticles while the injection at 120^{o}C has been previously shown to lead to 3 nm Au nanoparticles [27]. The reacted mixture was subsequently oxidized in air at room temperature for 1 h to ensure complete oxidation of Fe_3O_4 nanoparticles. The particles were isolated by adding excess isopropanol followed by centrifugation for 5 min at 3000 rpm. The oleic-capped nanoparticles were encapsulated with carboxy-PEGylated phospholipids (PL-PEG), resulting in stable water-soluble HNPs (see Supplementary Information). The carboxyl-terminated HNPs nanoparticles were further modified by covalently attaching A33scFv single antibody [23] using EDC-NHS chemistry following the manufacturer's protocols and then fluorescently-labeled with Alexa Fluor 488. Bovine Serum albumin (BSA) was similarly immobilized on the particles and used as the non-targeted particle conjugate control (see Supplementary Information). Particle purification to eliminate excess micelles, un-conjugated antibody and fluorophore were carried out in a size exclusion chromatography using FPLC

system (Superdex 200 size exclusion column on an AKTA Explorer FPLC, Amersham Biosciences, Piscataway, NJ).

2.3. Particle characterization

Particles were characterized by transmission electron microscopy (Philips, Tecnai F20, TEM) operating at 120kV and Dynamic light scattering (DLS) Zetasizer ZS system (Malvern, UK) to determine size and composition. The particles were also characterized to determine the magnetic character using vibrating sample magnetometer (VSM, Lakeshore Model 7410) while magnetic relaxivity (r_2) and contrast agent (T_2) values were determined using a 3.0-T GE HDx imager (General Electric Healthcare, Waukesha, WI). The optical properties were determined by obtaining an absorption spectrum using Shimadzu UV-3101 UV/Vis/NIR spectrophotometer in the range of 400 to 1000 nm. Further, the fluorescently-labeled HNPs-antibody conjugates were characterized using spectrophotometer (Perkin Elmer, LSB-50) at 490/520 nm excitation and emission wavelength, respectively.

2.4. Cell Culture

Colorectal cancer cell lines (SW1222 and HT 29 cells) were used to demonstrate specific targeting and phototherapy using laser irradiation. The cells were cultured in Dulbecco's modified Eagle medium (DMEM), supplemented with 10% fetal bovine serum (FBS), 1% penicillin-streptomycin (P/S, 100 units/mL penicillin, and 100 µg/mL streptomycin). For all studies, cell were grown overnight as monolayers at concentration of 10,000 cells per well at 37 ^{o}C and 5% CO_2 in a humidified incubator [28]. The cells were grown in black-walled 96-well

plates for toxicity assays and photothermal therapy assays and in glass 35-mm glass bottom culture dishes for confocal microscopy analyses.

2.5. Cellular Uptake Assay

Cells were grown in 35 mm glass-bottom flask overnight for particle uptake assay. As a control, SW 1222 cells expressing the A33 antigen receptor were treated using excess A33scFv in phosphate buffer (PBS, pH 7.4) for 4 hr to block the extracellular A33 antigen receptors. This was compared to the response of untreated SW 1222 cells. After which the SW 1222 and HT 29 cells were treated with equal concentrations of fluorescently-labeled HNPs particle conjugates (HNPs-scFv) and then incubated for various time durations before analyzing by confocal microscopy. The cells were washed with PBS twice and fresh medium added. Cellular uptake was quantified by measuring the fluorescence intensity of Alexa Fluor 488 with 490/520 nm excitation-emission filter.

2.6. Photothermal Therapy

Malignant colorectal cancer cell line, SW1222 cell line, which express A33 antigen and HT 29 cell line that do not express the antigen were used to study the phototherapy effect of the nanoparticles. The cells were grown at concentration of 100,000 cells/well in a 96-well plate overnight. The monolayers were treated with HNPs-A33scFv conjugates for 3 hr in fresh medium. After which the cells were washed and fresh medium replenished before laser irradiation with a continuous wave 808-nm laser for 6 min. To find the threshold NIR irradiation intensity for inducing photothermal destruction, the laser power was increased step-wise (n ~ 2.5 W cm^{-2}) while maintaining a fixed irradiation area of 4 mm in diameter. Cell viability after laser

irradiation was assessed using a membrane-permeable dye calcein-AM used as a live cell stain. The dye permeates cell membranes and is digested by esterases inside the cytoplasm to produce a green fluorescent calcein dye. Briefly, 40 µL of 10 µM of freshly prepared calcien AM solution was added and incubated for 1 h. The cells were imaged using fluorescence microscope (Olympus BX50) and the number of viable cells quantified by measuring the fluorescence using a microplate reader on spectrophotometer (LS-50B) with 470 nm/ 520 nm excitation-emission filter.

2.7. Flow cytometric apoptosis analysis after Photothermal Therapy

To resolve the extent of laser phototherapeutic effect, cells irradiated with varying laser power intensities were double-stained with Annexin V-(FITC) and (PI) detection kit to determine the percent of apoptotic and necrotic cells. In brief, cultured and laser treated SW1222 cells were washed with Annexin-V binding buffer and stained with Annexin-V (5 µL) and PI (5 µL) for 15 min at room temperature in the dark. After the addition of 400 µL of binding buffer, cells were analyzed by FACScanCalibur flow cytometer using 488 nm and 533 filters for Annexin-V FITC and PI detection, respectively (Becton Dickinson).

3. Results and Discussion

3.1. Nanoparticle Synthesis, Functionalization and Characterization

The hybrid gold nanoparticles synthesized by thermal decomposition of iron and gold precursors resulted in particles with an average aggregate size of 25 nm as characterized by TEM and DLS (**Figure 2-1 (a, b)**). The TEM micrographs showed monodispersed dumbbell-like Au-

Fe_3O_4 composed of 6 ± 2 nm Au and 18 ± 3 nm Fe_3O_4 nanoparticles. The Au nanoparticles appear darker in color while the Fe_3O_4 appear lighter due to the higher electron density of gold. The DLS data showed oleic acid-capped particles with an average aggregate size of 28 ± 5 nm (**Figure 2-1 (b)**). This is consistent with the TEM size measurements (6 nm Au and 18 nm Fe_3O_4 with a 1.8 nm monolayer of oleic acid and the chloroform solvent layer 0.64 nm). Subsequent functionalization with carboxy-PEGylated phospholipids (PL-PEG) increased its hydrodynamic aggregate size to 65 ± 5 nm (**Figure 2-1 (c, d)**). The PL-PEG layer coating was invisible due to its low electron density compared to the core of HNPs and could not be accounted for in the TEM measurements and, thus, showed no increase in size (**Figure 2-1 (c)**). The resulting HNPs were water-soluble and stable for up to 6 months with no visible aggregation and much more stable than a previously reported functionalization strategy stable in aqueous solutions that aggregated in less than < 24 hr [29].

The potential use of HNPs for NIR photothermal therapy is dependent upon ability to absorb energy (light) in the NIR region. Nanomaterials with high absorbance around 700-900 nm have previously been shown to be ideal materials for NIR therapy [30-32]. The optical properties of the nanoparticles were characterized by obtaining a UV-Vis spectrum (**Figure 2-1 (e)**). The Au-Fe_3O_4 nanoparticles have an absorption peak at 525 nm and at 505 nm for 8-nm Au nanoparticles. As compared to the single-component Fe_3O_4, the hybrid nanoparticles showed enhanced optical absorption properties in the NIR region. The increase in the absorbance of Au-Fe_3O_4 nanoparticles is due to the presence of Au in the particle composition which has been reported in several gold nanostructures used for NIR imaging [25]. The optical properties of these particles compares well to the gold nanoparticles UV-Vis spectra in the literature (peaks at 550

nm for core shell Au and 800 nm for hollow Au nanoparticles) [25, 33]. In addition, the slight red shift of the Au-Fe_3O_4 has been attributed to the junction effect between Au and Fe [29].

The potential use of HNPs for therapy as well as for magnetic resonance imaging also depends on their magnetic properties. Generally, magnetic materials with superparamagnetic properties have been used as *in vivo* MRI contrast agents [34-36]. The field-dependent magnetization curve of the Au-Fe_3O_4 shows no hysteresis at room temperature (**Figure 2-1 f**), which is consistent with superparamagnetic behavior arising from the iron oxide (magnetite) nanoparticles. The VSM measurements showed a magnetic moment of 44 for Au-Fe_3O_4 and 81 emu/g for bare Fe_3O_4 nanoparticles. These results compare well with previously reported literature values [12, 29]. To demonstrate the potential use as an enhanced MRI contrast agent, Au-Fe_3O_4 was compared to bare Fe_3O_4 nanoparticles of an equivalent iron concentration. MR images were obtained using a clinical 3.0-T MR system as described elsewhere (Supplemental Information). The hybrid Au-Fe_3O_4 show a MR contrast with a r_2 relaxivity value of 49.2 $mM^{-1}s^{-1}$ while Fe_3O_4 exhibited stronger MR contrast with a relaxivity value of 69.0 $mM^{-1}s^{-1}$ (**Figure 2-2**). The significant decrease in the relaxivity value Au-Fe_3O_4 is attributed to the weakly magnetic contribution from the Au nanoparticles. These properties make the HNPs potential MRI T_2 contrast agents.

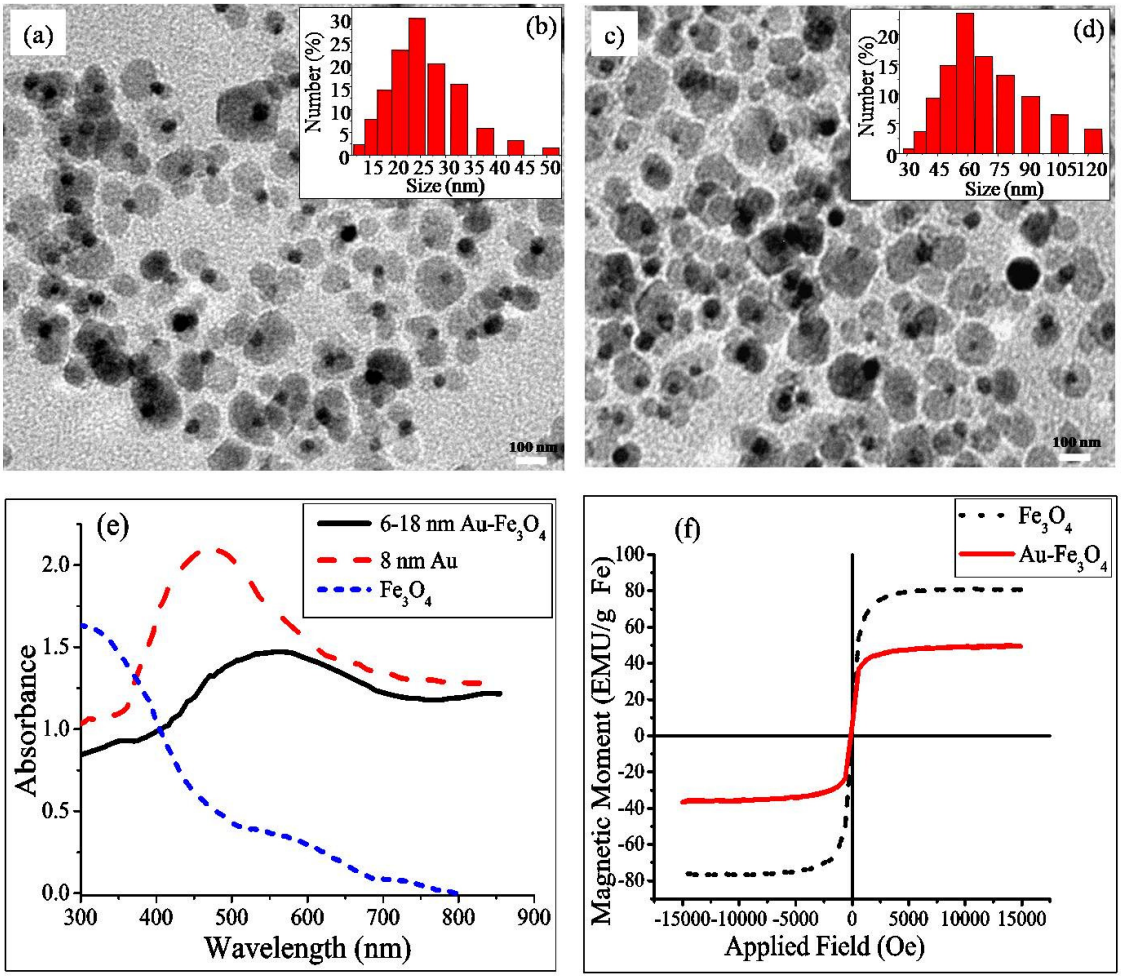

Figure 2-1: Particle characterization of Au-Fe_3O_4 of ; (a, b) TEM and DLS data of 'as synthesized' oleic-capped particle size with average of 25 nm; (c, d) PL-PEG coated particles with average size 65 nm; (e) optical properties of HNPs with strong absorption at 600-800 nm; (f) Superparamagnetic properties with 40 emu/mg magnetic moment. Scale bar: 100 nm TEM

The use of nanoparticles *in vitro* and *in vivo* requires that they are biocompatible. The cytotoxic behavior of HNPs- and targeted HNPs-A33scFv conjugates on SW 1222 cells were examined by the MTT (3-(4,5-dimethylthiazol-2-yl)-2,5-diphenyltetrazolium bromide) assay. As expected, the HNPs were reasonably nontoxic and biocompatible up to 100 µg particle concentration, whereas HNPs-A33 scFv conjugates show a dose-dependent toxicity. Thus, no obvious cytotoxicity was observed at low doses up to 100 µg HNPs, while higher doses exhibited some toxicity (**Figure 2-3**).

3.2. Confocal Imaging and Cellular Uptake

The HNPs-scFv were fluorescently labeled with Alexa Fluor 488 and in turn used to demonstrate cellular particle uptake in SW 1222 cells. The particle conjugates showed a slight red shift from an emission maximum of 520 nm for an un-conjugated Alexa Fluor 488 to 525 nm after conjugation to scFv or BSA (**Figure 2-S1 (a-b**) in the Supplementary Information). Further, the labeled particles of HNPs-scFv and HNPs-BSA showed to have equal conjugation efficiency which is necessary if they are to be used for comparative cellular uptake experiments (Figure S1 in the Supplementary Information). They can also potentially be used for *in vivo* fluorescence imaging to monitor the effects of therapeutics [37]. The un-conjugated HNPs showed no fluorescence, confirming that the fluorescence is due to presence of Alexa Fluor 488 (Supplementary information). The applicability of scFv to target and enhance therapeutic /particle uptake was demonstrated using confocal laser scanning microscope to image cells incubated with fluorescently-labeled HNPs-scFv or HNPs-BSA conjugates. SW 1222 cells used as a control for receptor-mediated endocytosis were pretreated with excess free A33 scFv molecules (non-fluorescent, 100 times the number of scFv on particle) before incubation with

HNPs-scFv conjugates. This was necessary to block the extracellular A33 antigen receptors for which HNPs-A33 scFv conjugates could bind and be endocytosed. **Figure 2-4 (a-f)** show bright-field and dark-field images obtained after 5-hr incubation where endocytosed particles appear green (HNPs-Alexa 488). The results show that there is enhanced particle uptake of HNPs-scFv in A33 antigen expressing cells (SW 1222 cells) as compared to the uptake in SW 1222 cells with blocked receptors or in HT 29 cells. A time-course study of particle uptake up to 15 h shows a time-dependent increase in the particle uptake for A33scFv single chain conjugated particles in cells expressing the A33 antigen cells while the particle uptake for non-A33 antigen cells is diminished (**Figure 2-4 (g)**). At 15 hr, there is a 5-fold preferential particle uptake of HNPs-scFv in SW1222 cells with unblocked receptors as compared with cells with blocked receptors are cells that do not express A33 antigen receptors (**Figure 2-4**). The preferential uptake of HNPs-scFv is attributable to receptor-mediated endocytosis which can be used to enhance particle uptake in A33-expressing colorectal cancer cells while limiting the uptake in non-antigen expressing cells. The use of targeting agent such as the A33scFv antibody is crucial in reducing amount of therapeutics such as the amount the energy laser power to below medical safety standard needed to achieve therapeutic effects in cancers [1, 25]. It also provides a targeting mechanism for *in vivo* imaging as well as for drug delivery [9, 38].

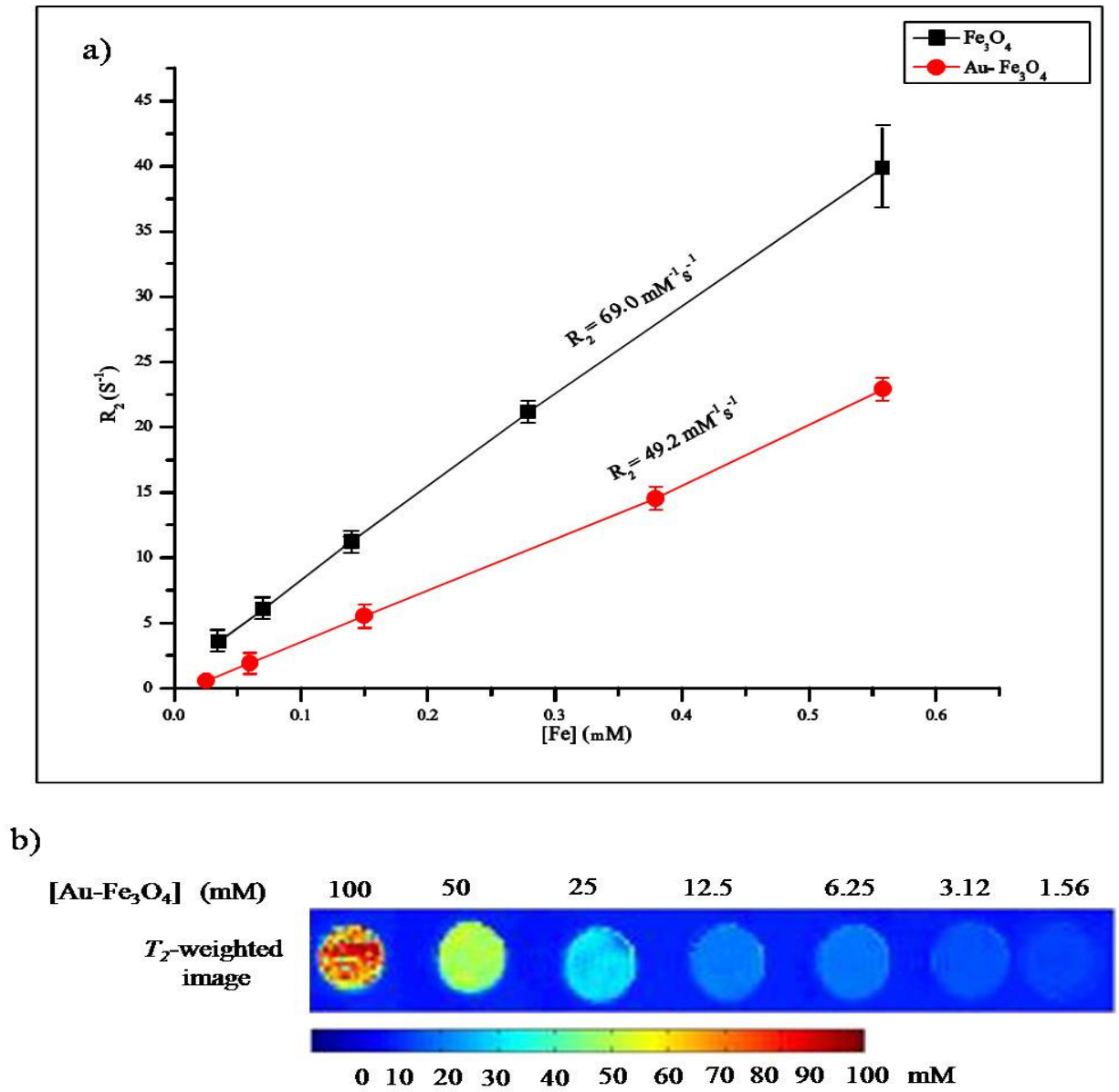

Figure 2-2 : (a) Plot of spin-spin relaxation rate (R_2) against Fe concentration for Au-Fe_3O_4 and bare Fe_3O_4 nanoparticles; (b) T2-weighted MR images of the PL-PEG-coated nanoparticles at various concentrations in water illustrating the detection limit to be lower than 31 µg/mL. Error bars represent variability in R2 values (n = 3).

3.4. In vitro phototherapy

As shown in **Figure 2-1 e**, HNPs showed strong absorption in the NIR region and can potentially be used for therapeutic applications of cancer cells using NIR irradiation. To demonstrate the photothermal effect *in vitro*, the SW 1222 and HT 29 cell lines were treated with HNPs-scFv conjugates and laser irradiated at varying intensities. The proportion of viable cells as a function irradiation intensity for both cell lines were quantified by measuring the fluorescence intensity of calcien AM staining of cell death are visualized in fluorescence microscopy images. **Figure 2-5** show fluorescent images of NIR-irradiated cells after calcien AM staining where the presence of green fluorescence indicate live cells and regions devoid of fluorescence indicate dead cells. After laser exposure at 5.1 W cm^{-2} for 6 min, the cell viability of SW 1222 cells decreased to nearly 53% while the viability of HT 29 cells remained almost unchanged (96%), indicating that the targeted HNPs-scFv conjugates are potent photothermal absorbers in cells that express A33 antigen (**Figure 2-5 (b, g)**). At higher laser power intensities, the proportion of viable SW 1222 cells decreases more dramatically than the HT29 cells as is shown by the widening area devoid of fluorescence for SW 1222 cells (see **Figure 2-5 (a-e)**). Increased photothermal destruction was observed with increasing laser intensity i.e. the proportion of viable SW 1222 cells decreased to 32%, 11%, and 1% for laser intensities of 7.9, 31.5, and 100 W cm^{-2}. In contrast, the control HT 29 cells that do not express A33 showed no significant decrease in cell viability at low laser intensity (98%, 96% and 90% for 3.2, 5.1 and 7.9 W cm^{-2}, respectively) and exhibited normal morphology after 6-min laser exposure. The fluorescent images show no observable cell damage and appear indistinguishable from the images of non-irradiated cells (**Figure 2-5 (f-h)**). Significant decrease in cell viability was

observed at 31.5 W cm^{-2} with 65% viability and 28% for 100 W cm^{-2} (**Figure 2-5 (i, j)**). At this dosage, the laser power is high enough to cause photodestruction in a nonspecific fashion, even in the absence of the light-absorbing nanoparticles.

The conclusion from this study was that use of A33scFv as a targeting agent leads to preferential particle uptake and that phothermal-active particles when irradiated with NIR irradiation result in photodestruction of SW 1222 cells at much less power (5.1 W cm^{-2}) than in cells that do not express A33 antigen (31.5 W cm^{-2}). This allows for highly localized treatment of cells that express a known and targeted biomarker achieved by the antigenic nature of the cells and not by the positioning of the laser irradiation. This system also could allow for broader application of laser illumination without adverse effects to untreated tissue thus allowing for greater assurance of complete irradiation of targeted areas.

The threshold laser power for the selective destruction of A33 antigen-expressing cells (SW1222 cells) using HNPs-scFv is approximated to be 5.1 W cm^{-2}. This value compares well to the 7.0 W cm^{-2} threshold power intensity reported for the use of transferrin-conjugated gold nanoparticles to selectively destroy breast cancer cells [1]. Gadolinium-based paramagnetic gold nanostructures with magnetic susceptibility and potential MRI agent have a reported 3.1 W cm^{-2} threshold laser power for photodestruction of SKB3-expressing breast cancer cells [25]. Silica-gold core-shell type gold nanoshells with 35.0 W cm^{-2} threshold laser power have also been reported [39]. While the potency of the hybrid Au-Fe_3O_4 compares favorably to other materials previously used for photothermal therapy, our HNPs can potentially be used for dual therapy and imaging via magnetic resonance imaging.

3.5. Flow Cytometric Analysis of Photothermally-treated cells

Flow Cytometric (FACS) analysis was performed to measure the percentage of live, apoptotic, and necrotic cells. The effect of laser irradiation on cell death was investigated by varying laser intensity with a fixed concentration of 0.5 mg of HNPs-scFv. The degree of apoptosis and necrosis was then examined by measuring the binding of Annexin-V FITC and inclusion/exclusion of PI using FACSCalibur flow cytometer (Becton Dickinson). Data were analyzed using the WINMDI software (Purdue University), employing a uniform analysis gate set on the core population of the cultured cells so that events of extreme forward or side scatter were excluded. The cytograms in **Figure 2-6** show the bivariate PI/Annexin-V analysis of SW 1222 cells after photothermal therapy at varying laser power. Viable cells are negative for both PI and Annexin-V (Q3), apoptosis cells are PI negative and Annexin-V positive (Q2), while necrotic cells are positive both PI and Annexin -V (Q1). After 6-min laser irradiation at 5.1 W cm^{-2}, 3.2% of the cell populations were apoptotic. With increasing laser power, the proportion of these cells increased to 7.0% at 7.9, 29.5% at 31.5, and 46.2% at 100 W cm^{-2}. The proportion of dead cells attributable to necrosis-related cell death were 22.5% for 5.1 W cm^{-2} and increased to 37.6% at 7.9, 56.4% for 31.5 W cm^{-2}, and 52.7% at 100 W cm^{-2} (**Figure 2-6 (a-d)**). It seems that cell death was dominated by late apoptosis-related death at various laser intensities while the proportion of the necrosis-related cell death increased at higher laser power (31.5 and 100 W cm^{-2}). Non-irradiated cells of equal density and grown under similar conditions were used as control. The flow cytometric analysis revealed that < 1% cells were apoptotic or necrotic cells with the vast majority being live cells with negative PI/Annexin-V (**Figure 2-6 e**). Our findings support other photothermal studies using anti-HER2 gadolinium-gold nanostructures targeting breast cancer cells that reported a similar observation where higher laser intensity to led increase in the necrotic cells [25]. This study confirmed the conclusion reached from our photothermal

study that using targeted particles increases preferential particle uptake in cells, which consequently reduces the amount of laser power required to reach threshold therapeutic levels. This study also provided more insight on the mechanism of cell death.

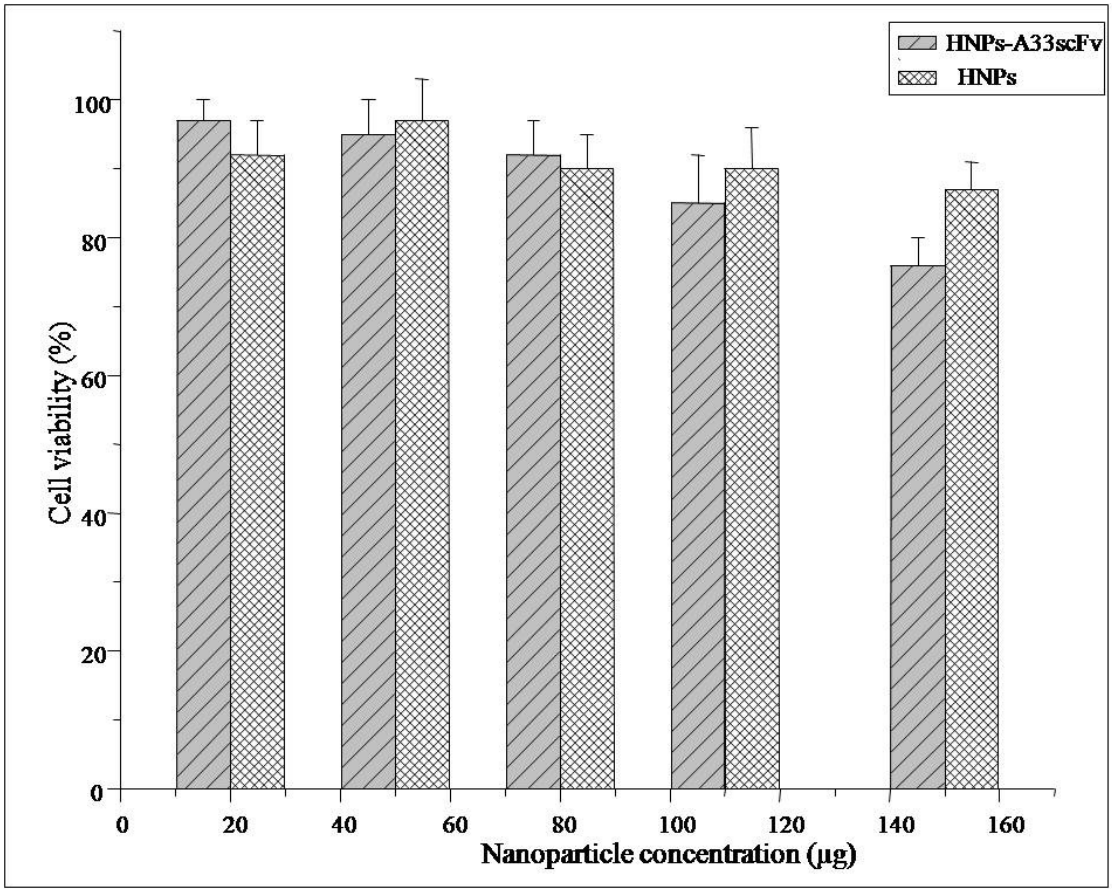

Figure 2-3: Cell viability of SW 1222 cells after incubating in increasing concentration particle conjugates as determined by MTT assay of: (a) HNPs- A33scFv, (b) HNPs-BSA. The results show a dose-dependent toxicity where there is significant cytoxicity at higher particle concentration. Error bars represent absorbance variability measured at 570 nm where n = 3.

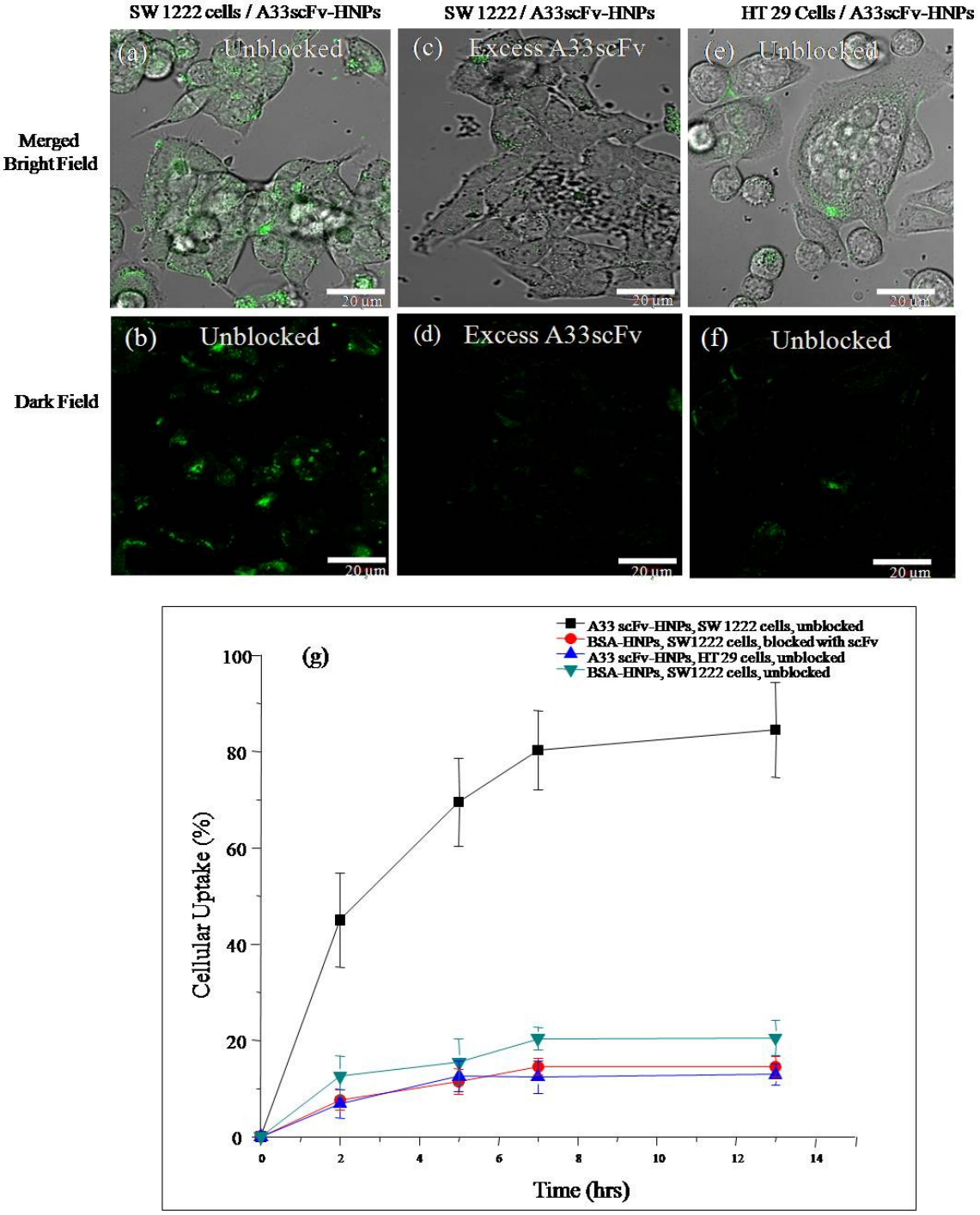

Figure 2-4: Particles uptake colorectal cancer cells as analyzed by confocal microscopy images; (a-d) SW1222 colorectal cancer cells with; (a, b) HNPs- A33scFv; (c, d) HNPs-BSA, blocked receptors; (e, f) HT 29 cells with HNPs- A33scFv for 5hr; scale bar:10 µm. g) time- course cellular uptake of HNPs conjugates. Error bars represent variability in image fluorescence (n = 5).

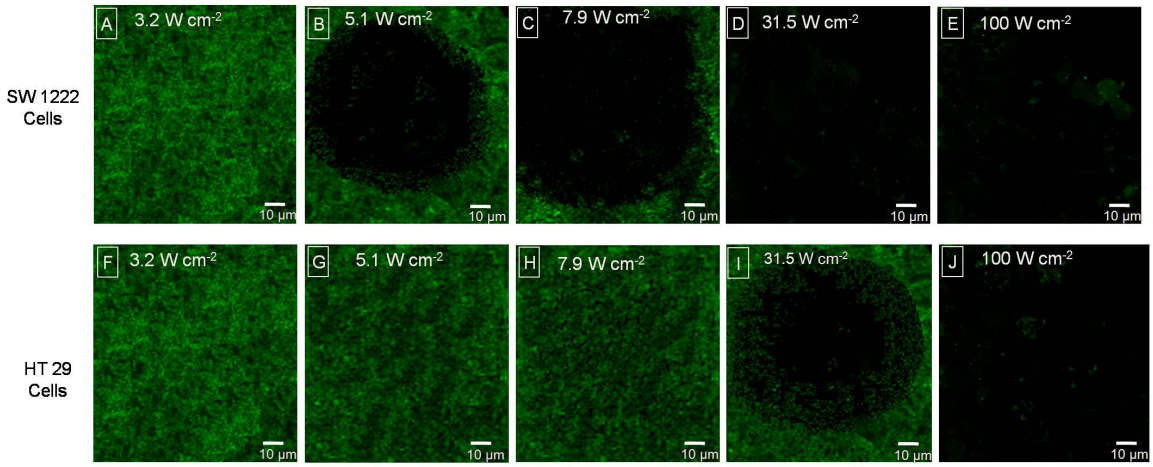

Figure 2-5: Cells incubated with HNPs-scFv and then irradiated by 800-nm laser for 6 min at different power densities. The first row shows SW 1222 cells while the second row shows HT 29 cells. Each column shows cells treated at a specific laser intensity where 3.2 W cm^{-2} (a, f), 5.1 W cm^{-2} (b, g), 7.9 W cm^{-2} (c, h), 31.2 W cm^{-2} (d, i) and 100 W cm^{-2} (e, j). Viable cells appear green from calcien AM staining while dark areas devoid of fluorescence are cells destroyed from photothermal irradiation. Scale bar 10 µm for all images.

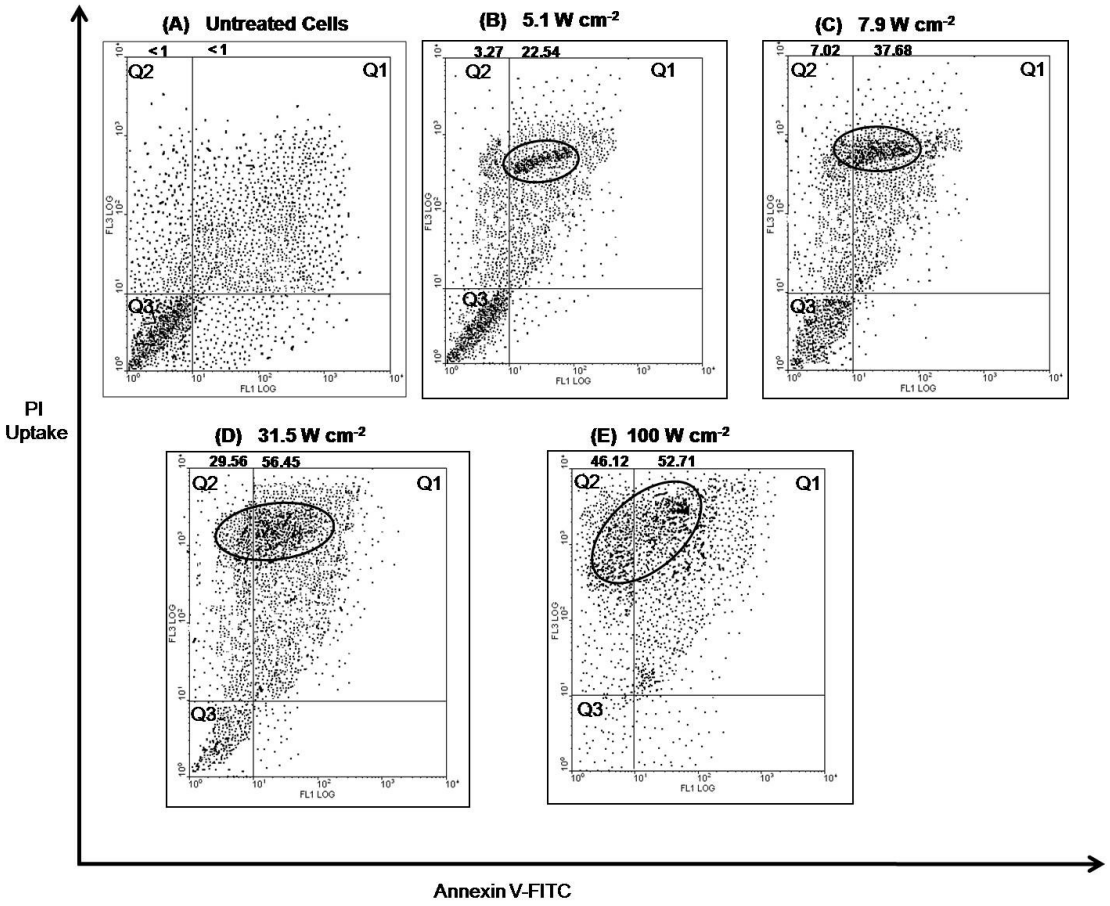

Figure 2-6: Flow cytometric analysis to determine death modes of SW 1222 colorectal cancer cells after NIR irradiation at varying laser intensities: (a) Untreated cells, (b) 5.2, (c) 7.9, (d) 31.5, (e) 100 W cm^{-2}, and. Cells are double-stained with Annexin V-FITC and propidium iodide (PI) to detect early apoptosis and necrosis (late stage apoptosis), respectively. Late apoptosis-related cell death is observed across the board with increasing necrosis-related cell death with increasing laser power.

4. **Conclusion**

In summary, this work reports the preparation of multifunctional gold-iron oxide nanoparticles for targeting, imaging and laser photothermal therapy of cancer cells using laser irradiation at 800 nm. The hybrid nanoparticles are functionalized with carboxyl-terminated phospholipid and then conjugated with A33scFv single chain antibody to target A33 antigen that are over-expressed on the surface of SW1222 colorectal cancer cells. Our preliminary results showed that the presence of the targeting antibody (scFv) can facilitate preferential cellular particle uptake. The photothermal studies with the immunotargeted hybrid nanoparticles show that they strongly absorb at 808 nm, with a photothermal cell damage power density threshold of ~ 5.1 W cm^{-2}. This threshold for selective destruction of cancer is substantially lower than those reported for gold nanoshells (35 W cm^{-2}) [39] and comparable to paramagnetic gold nanostructures (3.1 W cm^{-2}) [25]. Further flow cytometric analysis of photothermally treated cells show that at lower power densities, the primary of model of cell death is by apoptosis-related cell death while the necrotic-related cell death becomes prevalent at higher laser densities (31.5 and 100 W cm^{-2}). The results also demonstrate that the nanoparticle conjugates are potential multifunctional probes for cancer diagnosis and therapy. *In vivo* studies will be carried out to examine the applicability of the multifunctional nanoparticles in targeting, imaging and therapy of cancer cells. The imaging can be carried out using MR imaging and scattering-based imaging techniques including two-photon photoluminescence imaging [16, 40].

Acknowledgments

We thank John Grazul (Cornell Center for Material Research) and Carol Bayles (Nanobiotechnology Center) for their assistance in performing TEM and fluorescence microscopy. The authors acknowledge the financial support from Sloan foundation and the Ludwig Institute for Cancer Research.

REFERENCES

1. Li, J. L.; Wang, L.; Liu, X. Y.; Zhang, Z. P.; Guo, H. C.; Liu, W. M.; Tang, S. H., In vitro cancer cell imaging and therapy using transferrin-conjugated gold nanoparticles. *Cancer Letters* **2009,** 274, 319-326.

2. Kim, J.; Park, S.; Lee, J. E.; Jin, S. M.; Lee, J. H.; Lee, I. S.; Yang, I.; Kim, J.-S.; Kim, S. K.; Hyeon, T., Designed Fabrication of Multifunctional Magnetic Gold Nanoshells and their Application to Magnetic Resonance Imaging and Photothermal Therapy. *Angew. Chem Int* **2006,** 45, 7754-7758.

3. Chen, J.; Wang, D.; Jiefeng, X.; Au, L.; Siekkinen, A.; Warsen, A.; Li, Z.-Y.; Zhang, H.; Xia, Y.; Li, X., Immuno Gold Nanocages with Tailored Optical Properties for Targeted Photothermal Destruction of Cancer Cells. *Nano Lett.* **2007,** 5, 1318-1322.

4. Kuo, W. S.; Wu, C. M.; Yang, Z. S.; Chen, S. Y.; Chen, C. Y.; Huang, W. M.; Sun, C. K.; Yeh, C. S., Biocompatible bacteria@Au composites for application in the photothermal destruction of cancer cells. *Chem Commun* **2008**, 4430-32.

5. Kam, N. W.; O'Connell, M.; Wisdom, J. A.; Dai, H., Carbon nanotubes as multifunctional biological transporters and near-infrared agents for selective cancer cell destruction. *Proc. Natl. Acad. Sci. USA* **2005**.

6. O'Neal, D. P.; Hirsch, L. R.; Halas, N. J.; Payne, J. D.; West, J. L., Photo-thermal tumor ablation in mice using near-infrared absorbing nanoparticles. *Cancer Lett* **2004,** 209, 171-6.

7. Wang, L.; Bao, J.; Li, Y.; Huang, Y., Multifunctional Nanoparticles Displaying Magnetization anfd Near-IR absorption. *Angew. Chem. Int.* **2008,** 120, (13), 2473-76.

8. Park, H.; Yang, J.; Seo, S.; Kim, K.; Suh, J.; Kim, D.; Haam, S.; Yoo, K.-H., Multifunctional Nanoparticles for photothermally controlled drug delivery and magnetic resonance Imaging Enhancement. *Angew. Chem. Int.* **2008,** 4, (2), 192-96.

9. Park, J. H.; Maltzahn, G. V.; Sangeeta, B. H.; Ruoslahti, E.; Bhatia, S. N.; Sailor, M. J., Micellar Hybrid Nanoparticles for Simultaneous Magnetofluorescent Imaging and Drug Delivery. *Angew. Chem. Int. Ed.* **2008,** 47, 1-6.

10. Drake, P.; Cho, H. J.; Shih, P. S.; Kao, C.-H.; Lee, K.-F.; Kuo, C. H., Gd-doped iron-oxide nanoparticles for tumour therapy via magnetic field hyperthermia. *J. Mater. Chem.* **2007,** 17, 4914-4918.

11. Wang, L.; Park, H. Y.; Lim, S. I.; Schadt, M. J.; Mott, D.; Luo, J.; Wang, X.; Zhong, C., Core@Shell nanomaterials: gold-coates magnetic nanoparticles. *J Mater Chem* **2008,** 18, 2629-35.

12. Wang, L.; Maye, M. W.; Fan, Q.; Rendeng, Q.; Zhong, C., Iron oxide-gold core-shell nanoparticles and thin film assembly. *J Mater Chem* **2005,** 15, 1821-32.

13. Josephson, L.; Kircher, M. F.; Mahmood, U.; Tang, Y.; Weissleder, R., Near-Infrared Fluorescent Nanoparticles as Combined MR/Optical Imaging Probes. *Bioconjugate Chemistry* **2002,** 13, (3), 554-560.

14. Medorova, Z.; Pham, W.; Kim, Y.; Dai, G.; Moore, A., In vivo imaging of tumor response to therapy using a dual-modality imaging strategy. *Int. J. Cancer* **2006,** 118, 2796-802.

15. Veiseh, O.; Sun, C.; Gunn, J.; Kohler, N.; Gabikian, P.; Lee, D.; Bhattarai, N.; Ellenbogen, R.; Sze, R.; Hallahan, A.; Olson, J.; Zhang, M., Optical and MRI Multifunctional Nanoprobe for Targeting Gliomas. *Nano Lett.* **2005,** 5, (6), 1003-1008.

16. Khemtong, C.; Kessinger, C. W.; Ren, J.; Bey, E. A.; Yang, S.; Guthi, J. S.; Boothman, D. A.; Gao, J., In vivo off-Resonance Saturation Magnetic Resonance Imaging of Targeted Superparamagnetic Nanoparticles. *Cancer Res* **2009,** 69, (4), 1651-55.

17. Prasad, N. K.; Rathinasamy, K.; Panda, D.; Bahadur, D., Mechanism of cell death induced by magnetic hyperthermia with nanoparticles of Mnx Fe2O3 synthesized by a single step process. *J. Mater. Chem.* **2007,** 17, 5042-5051.

18. Arbab, A. S.; Bashaw, L. A.; Miller, B. R.; Jordan, E. K.; Lewis, B. K.; H, K., Characterization of biophysical and metabolic properties of cells labeled with superparamagnetic iron oxide nanoparticles and transfection agent for cellular MR imaging. *Radiology* **2003,** 229, (3), 838-46.

19. Glennie, M. J.; van de Winkel, J. G., Renaissance of cancer therapeutic antibodies. *Drug Discovery Today* **2003,** 8, 503-5.

20. Deckert, P. M.; Renner, C.; Cohen, L. S.; Jungbluth, A.; Ritter, G.; Welt, S., A33scFv-cytosine deaminase:a recombinant protein construct for antibody-directed enzyme-pro-drug therapy. *J. Cancer* **2003,** 88, 937-939.

21. Ackerman, M.; Chalouni, C.; Schmidt, M.; Raman, V.; Ritter, G.; Old, L.; Mellman, I.; Wittrup, K., A33 antigen displays persistent surface expression. *Cancer Immunology, Immunotherapy* **2008,** 57, (7), 1017-1027.

22. Daghighian, F.; Barendswaard, E.; Welt, S.; Humm, J.; Scott, A.; Willingham, M. C.; McGuffie, E.; Old, L. J.; Larson, S. M., Enhancement of Radiation Dose to the Nucleus by Vesicular Internalization of Iodine-125-Labeled A33 Monoclonal Antibody. *J Nucl Med* **1996,** 37, (6), 1052-1057.

23. Damasceno, L.; Pla, I.; Chang, H. J.; Cohen, L.; Ritter, G.; Old, L. J.; Batt, C. A., An optimized fermentation process for high-level production of a single-chain antibody fragment in Pichia pastoris. *Protein Express Purif.* **2004,** 37, 18-26.

24. Hong, Y. C.; Sinoj, A.; Juana, M.; Soazig, C. D.; Kahli, S.; Il, K.; Carl, A. B., Encapsulation of Single Small Gold Nanoparticles by Diblock Copolymers. *Chem Phys Chem* **2008,** 9, (3), 388-392.

25. Lim, Y. T.; Cho, M. Y.; Lee, J. M.; Chung, B. H., Paramagnetic gold nanostructures for dual bioimaging and phototherapy of cancer cells. *Chem Commun* **2008**, 4930-4932.

26. Yu, H.; Chen, M.; Rice, P. M.; Wang, S. X.; White, W. R. L.; Sun, S., Dumbbell-like Bifunctional Au-Fe3O4 Nanoparticles. *Nano Lett.* **2005,** 5, (2), 379-382.

27. Shi, W.; Zeng, H.; Sahoo, Y.; Ohulchanskyy, T. Y.; Ding, Y.; Wang, Z. L.; Prasad, P. N., A General Approach to Binary and Ternary Hybrid Nanocrystals. *Nano Lett.* **2006,** 6, (4), 875-881.

28. Cortez, C.; Crook, T. E.; Johnson, A. P. R.; Radt, B.; Cody, S. H.; Caruso, F., Targeting and Uptake of Multilayered Particles for Colorectal Cancer cells. *Adv Mater* **1998,** 18, 1998-2003.

29. Xu, C.; Xie, J.; Wang, C.; Kohler, N.; Walsh, E. G.; Morgan, J.; Chin, Y. E.; Sun, S., Au-Fe3O4 Dumbbell Nanoparticles as Dual-Functionalal Probes *Angew. Chem. Int.* **2008,** 47, 173-176.

30. Terentyuk, G. S.; Maslyakova, G. N.; Suleymanova, L. V.; Khlebtsov, N. G.; Khlebtsov, B. N.; Akchurin, G. G.; Maksimova, I. L.; Tuchin, V. V., Laser-induced tissue hyperthermia mediated by gold nanoparticles: toward cancer phototherapy. *Journal of Biomedical Optics* **2009,** 14, (2), 021016-9.

31. Murphy, C. J.; Gole, A. M.; Stone, J. W.; Sisco, P. N.; Alkilany, A. M.; Goldsmith, E. C.; Baxter, S. C., Gold Nanoparticles in Biology: Beyond Toxicity to Cellular Imaging. *Accounts of Chemical Research* **2008,** 41, (12), 1721-1730.

32. Niidome, T.; Yamagata, M.; Okamoto, Y.; Akiyama, Y.; Takahashi, H.; Kawano, T.; Katayama, Y.; Niidome, Y., PEG-modified gold nanorods with a stealth character for in vivo applications. *Journal of Controlled Release* **2006,** 114, (3), 343-347.

33. Larson, T. A.; Bankson, J.; Aaron, J.; Sokolov, K., Hybrid plasmonic magnetic nanoparticles as molecular specific agents for MRI imaging and photothermal therapy of cancer cells *Nanotechnology* **2007,** 18, 325-333.

34. Sun, S.; Zeng, H., Size-Controlled Synthesis of Magnetite Nanoparticles. *J. Am. Chem. Soc* **2002,** 124, 8204-8205.

35. Jun, Y. H., YM; Choi, JS; Suh, JS; Cheon, J, Nanoscale Size Effect of Magnetic Nanocrystals and Their Utilization for Cancer Diagnosis via Magnetic Resonance Imaging. *JACS* **2005,** 127, 5732-5733.

36. Lee, J. H., YM; Jun, JW; Jang, JT; Cheon, J, Artificially engineered magnetic nanoparticles for ultra-sensitive molecular imaging; Nature medicine. *Nature Medicine* **2007,** 13, (1), 95-99.

37. Dubertret, B.; Skourides, P.; Norris, D. J.; Noireaux, V.; Brivanlou, A. H.; Libchaber, A., In Vivo Imaging of Quantum Dots Encapsulated in Phospholipid Micelles. *Science* **2002,** 298, 1759-1761.

38. Welt, S.; Ritter, G.; Williams, C.; Cohen, L. S.; John, M.; Jungbluth, A.; Old, E. A., Phase I Study Anticolon Cancer Humanized Antibody A33. *Clin Cancer Res* **2003,** 9, 1338-1346.

39. Hirsch, L. R.; Stafford, R. J.; Bankson, J. A.; Sershen, S. R.; Rivera, B.; Price, R. E.; Hazle, J. D.; Halas, N. J.; West, J. L., Nanoshell-mediated near-infrared thermal therapy of tumors under magnetic resonance guidance. *Proc. Natl. Acad. Sci. U. S.A* **2003,** 100, (23), 13549-13554.

40. Park, J.; Estrada, A.; Sharp, K.; Sang, K.; Schwartz, J. A.; Smith, D. K.; Coleman, C.; Payne, J. D.; Korgel, B. A.; Dunn, A. K.; Tunnell, J. W., Two-photon-induced photoluminescence imaging of tumors using near-infrared excited gold nanoshells. *Opt. Express* **2008,** 16, 1590-1599.

Supplementary Information

Gold Hybrid Nanoparticles for Targeted Phototherapy and Cancer Imaging

Experimental Section

Synthesis and Functionalization of Au-Fe_3O_4 hybrid nanoparticles (HNPs): Gold-iron oxide hybrid nanoparticles capped with oleic acid were synthesized by a previously reported procedure [1]. The surface HNPs nanoparticles were then functionalized with carboxyl group-containing phospholipid by coating with (1,2-Distearoyl-sn-Glycero-3-Phosphoethanolamine-N-[carboxy(Polyethylene Glycol) 2000 (PL-PEG COOH) [2]. Briefly, 17 mg of oleic acid-capped as-synthesized nanoparticle powder was suspended in 1mL chloroform with $5.5x10^{-6}$ moles of carboxyl-terminated PEG phospholipids (PL PEG COOH). The chloroform was evaporated to dryness at room temperature and the residue heated to 80^{o}C. The particles were rehydrated in 1mL of borate buffer (pH = 5.5) and then spun at 500,000 x g in an ultracentrifuge to eliminate empty micelles. The resuspended water-soluble HNPs were sonicated in a bath sonicator (Branson Sonifier 250, Branson Ultrasonics) for 30 minutes and were subsequently bio-functionalized.

Bio-functionalization of HNPs with A33 single chain antibody (A33scFv): The PL-PEG-coated HNPs were then subsequently functionalized to attach single chain antibody as well as bovine serum albumin using EDC-NHS chemistry (1-Ethyl-3-(3-dimethylaminopropyl carboiimide HCl and N-hydroxylsulfosuccinimide). Briefly, 50 µL of 5 mg mL^{-1} HNPs-PL-PEG were dispersed in borate buffer (pH = 5.5) and then reacted with 40 mg EDC and 20 mg NHS for 20 min at room temperature. Excess EDC and NHS were removed by using a size exclusion chromatography FPLC system (Superdex 200 size exclusion column on an AKTA Explorer

FPLC, Amersham Biosciences, Piscataway, NJ) eluted with 50 mM sodium borate buffer (pH 5.5) and concentrated by centrifugation (3 000 rpm, 10 min) using a 30,000 MWCO filter (Millipore). The NHS-ester activated HNPs were reacted with 2 mL of 1 mg mL^{-1} A33 scFv at 4^{o} C for 2 hr. The conjugates were again purified by size exclusion chromatography FPLC system eluting with 50 mM phosphate-buffer saline (pH 7.4).

Fluorescent-labeling of HNPs-scFv: The HNPs-scFv conjugates were then reacted with amine-reactive Alexa Fluor® 488 carboxylic acid, tetrafluorophenyl (TFP) ester following manufacturer's protocol (Invitrogen). Briefly, 100 µL of 3.1 mg mL^{-1} of HNPs-scFv were added into 1 mL of 10 mM of bicarbonate solution (pH 8.1) to which excess amine-reactive Alexa Fluor (TFP) 488 was added and stirred at 4^{o} C for 3 hr. The fluorescently-labeled HNPs-scFv conjugates were also purified using size exclusion chromatography FPLC system eluted using phosphate-buffer saline (pH 7.4). The labeled HNPs-scFv were concentrated to 1 mg mL^{-1} by centrifugation and subsequently used to perform cellular uptake experiments. The fluorescence of HNPs-scFv and HNPs-BSA conjugates were measured using spectrophotometer (LS-B 50, Perkin Elmer, 490/520 excitation-emission wavelengths). The successful antibody immobilization was determined by measuring the fluorescence of the nanoparticle conjugates. The presence of fluorescence in purified nanoparticle conjugates indicates that the A33scFv was successfully immobilized on the particles. This is because amine-reactive Alexa Fluor 488 would not react directly with the carboxyl-terminated nanoparticles, but would react via amines groups on the antibody which were covalently linked to the A33 scFv antibody via EDC-NHS chemistry.

Magnetic Resonance Imaging (MRI) measurement: To determine the potential application of HNPs particles for MR contrast imaging, serial dilution of particles were prepared

and the T_2-weighted value measured using a 3T GE HDx imager (General Electric Healthcare, Waukesha, WI). A transmit-receive knee coil array was used for data acquisition, T_2-weighted fast-spin-echo sequences with the following parameters were used: repetition rate (TR) = 2400 ms, echo time (TE) = 80 ns, slick thickness = 0.5 mm, field of view = 140 x 140 mm, echo train length = 13.

Magnetic nanoparticles are known to shorten the spin-spin relaxation time (T_2) of water resulting in a decrease in the MR signal intensity. The MR signal intensity decreased with increasing HNPs concentration because of higher concentration of Fe_3O_4 nanoparticles.

Nanoparticles Cytotoxicity and cell viability Assay: *In vitro* cytotoxicity was evaluated by 3-(4,5-dimethylthiazol-2-yl)-2,5-diphenyltetrazolium bromide (MTT) assay. Briefly, 10,000 cells/well were seeded in black-walled 96-well culture plates in a final volume of 100 µL. After attachment for 24 h, cells were incubated with nanoparticle conjugates at various concentrations (0, 30, 60, 90, 120, 150 µg HNPs) for 12 h before adding 50 µl of MTT (5 mg mL^{-1} in PBS) solution to each well for an additional 4 h. The reaction was stopped by removal of MTT, and formazan crystals were solubilized in 100 µl dimethyl sulfoxide (DMSO) in each well. Absorbance at 570 nm was recorded using a Model 680 Microplate Reader (Bio-Rad, Bath, UK) and then correlated to cell viable using a beer law via a standard curve.

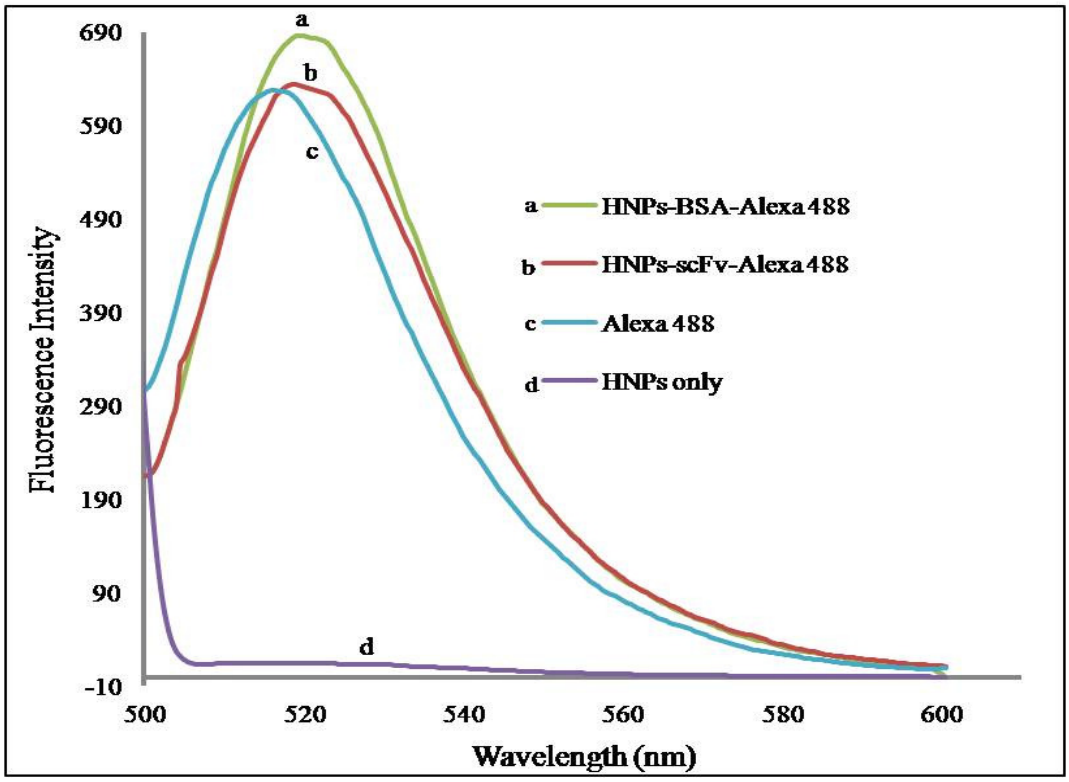

Figure 2-S1: Fluorescence spectra of particle conjugates obtained at 490/ 520 excitation-emission wavelength of Alexa Fluor 488-labeled conjugates; (a) HNPs-BSA, (b) HNPs-A33scFv,(c) Alexa 488, and (d) HNPs only. The fluorescently labeled particles show an emission peak while non-fluorescent HNPs do not have an emission peak.

Figure 2-S1 show fluorescence spectra of Alexa 488 labeled-particle conjugates. The fluorescence of HNPs-A33scFv and HNPs-BSA conjugates are represented on **Figure 2-S1** (**a, b**) in which the emission maximum is shifted ~ 5 nm higher compared to un-conjugated dye (**Figure 2-S1 (c)**). The HNPs-BSA-Alexa 488 conjugates that were treated and reacted in a similar fashion (**Figure 2-S1 (b)**) have equal fluorescence intensity, suggesting equivalent conjugation efficiency.

REFERENCES

1. Yu, H.; Chen, M.; Rice, P. M.; Wang, S. X.; White, W. R. L.; Sun, S., Dumbbell-like Bifunctional Au-Fe3O4 Nanoparticles. *Nano Lett.* **2005,** 5, (2), 379-382.

2. Dubertret, B.; Skourides, P.; Norris, D. J.; Noireaux, V.; Brivanlou, A. H.; Libchaber, A., In vivo Imaging of Quantum Dots Encapsulated in Phospholipid Micelles. *Science* **2002,** 298, (5599), 1759-1762.

Chapter 3

Polyacrylic acid-derived Gold Nanorods for Cellular Targeting and Photothermal Therapy

Abstract

The modification and control of surface chemistry on gold nanorods (GNRs) is a critical step in the production of functional GNRs for use in a myriad of applications. The popular cetyltrimethyl ammonium bromide (CTAB)-capped GNR synthesis produces stabile aqueous suspensions of GNRs having a net positive surface charge and trimethyl ammonium surface groups. However, CTAB-capped GNRs are inert to traditional coupling chemistries, and typically require GNR ligand exchange in order to change the GNR surface groups to more functional moieties (e.g., carboxylates, amines, thiols). Further, CTAB removal and ligand exchange often presents problems associated with GNR precipitation. Here, we report a single-step, layer-by-layer procedure to functionalize CTAB-capped GNRs with functional carboxylic acid surface groups via electrostatic self-assembly using polyacrylic acid (PAA). This approach allowed for consistent biomolecule-GNR coupling using standard carboxyl-amine conjugation chemistries. The current study focuses on cancer targeting biomolecule-GNR conjugates and selective photothermal destruction of cancer cells by GNR-mediated hyperthermia and near-infrared light. Gold nanorods were conjugated to a single chain antibody (A33scFv) selective for colorectal carcinoma cells and used as probes to target, visualize and demonstrate photothermal therapy of colorectal carcinoma cells. Selective targeting and GNR uptake in antigen-expressing

human colorectal carcinoma (SW 1222) cells were observed using fluorescence microscopy. Selective photothermal therapy is demonstrated using SW 1222 cells, where > 62 % cell death was observed after cells are treated with targeted A33scFv-GNRs and an 808-nm diode laser.

Gold nanorods (GNRs) are nanoscale materials that possess interesting optical properties and unique application potentials particularly in photothermal therapy,[1, 2] biosensing,[3] molecular imaging,[4-6] and in gene delivery,[7] for cancer therapy. These various potential applications require that the nanorods be functionalized to attach different biochemical groups. However, this is a very challenging issue that typically involves multistep processes and can lead to shape change and self-assembly based aggregation. As synthesized, nanorods are coated with a cationic surfactant cetyltrimethyl ammonium bromide (CTAB) stabilizer that does not provide useful chemical moieties for successive conjugation to attach biomolecules. Previous conjugation strategies have involved exchanging CTAB for other molecules with useful functional groups. A common example is the use of thiolated bifunctional small molecules such as mercaptopropionic acid and/or mercaptohexanoic acid and other homofunctionalized thiol molecules (e.g poly(ethylene glycol) (PEG)-thiols) chemisorbed on the nanorod surfaces [8] to displace CTAB from the surface. While thiolated nanorods have good colloidal stability in buffered solutions,[9] they are prone to detach from the particle surface in the presence of other thiols, or during chromatographic purification steps. Additionally, thiols are reactive to some conjugation reagents (e.g., maleamide). The instability of thiol groups have been shown to increase particles' rapid clearance in blood, making them less desirable for *in vivo* applications that require long blood half-life.[10] Gold nanorods are also commonly functionalized by applying a thin layer of mesoporous silica coat on nanorods and then chemically modifying the silica surface with another silane molecule (e.g. aminopropyltrimethoxysilane) for conjugation to molecular targets. Silica-coated nanorods have been shown to have good colloidal stability; however its syntheses require the use of intermediate coatings such as poly (vinylpyrrolidone) and polystyrene sulfonate to facilitate silica coating.[11] Additionally, obtaining a smooth silica

thickness is critically dependent on amount of CTAB on the nanorods, amount of base added, and ethanol or methanol/water ratio used.[12, 13] This process is often tedious and time-consuming resulting in nanorods that are prone to aggregation and have limited uses in biomedical applications.

Another commonly used method is Layer-by-layer (LBL) electrostatic adsorption of polyelectrolytes on positively-charged CTAB surface on GNRs.[14] Layer-by-layer coating involves applying a layer of negatively-charged poly-styrene sulfonate (PSS) over CTAB layer and then subsequently coating with positively-charged polyallylamine hydrochloride (PAH) layer.[11] This coating alters the surface charge on GNRs in order to achieve good colloid stability and/or to enhance cellular uptake. For example, Chen et al recently prepared PAH-PSS-GNRs with a net positive surface charge that could stain HeLa cells due to electrostatic interaction.[15] While coating GNRs with these polyelectrolytes have been shown to enhance biocompability and increase cellular uptake, they have been immobilized through time-consuming, multistep processes and have not been used for covalent attachment of targeting agents that are critical to achieve specificity required for cellular applications.

In this report, we outline a novel, simple layer-by-layer method for direct coating of CTAB-stabilized gold nanorods with polyacrylic acid (PAA) without intermediary coating step or no further polymerization step (Scheme 3-1). Additionally, the coating strategy allows the covalent attachment of targeting molecules such as single chain antibodies without further modifications. We hypothesized that CTAB-capped nanorods can be coated in a single-step with a thin layer of PAA coating resulting in rods with peripheral carboxyl groups for facile attachment of targeting agents such as A33scFv. Photothermal therapy application of targeted A33-GNRs was demonstrated in colorectal cancer cells using a continuous wave 808-nm laser

treatment. The cationic CTAB adsorbed to the nanorods can provide strong positive charges to which a layer of negatively-charged PAA can form stable water-soluble nanorods with carboxyl functional groups on the surface. The carboxyl functional groups provide critical anchors for targeting agents and other biomolecules. Cytotoxicity of the resultant PAA-coated GNRs were demonstrated using a human colon adenocarcinoma, SW 1222 cell line, known to express A33 receptors on the plasma membrane [16] and assessed viability after 24 h of incubation with nanorods using the 3-(4,5-dimethylthiazol-2-yl)-2,5-diphenyltetrazolium bromide (MTT) assay. Gold nanorods were then conjugated to A33 single chain antibody (A33scFv) to form A33scFv-GNRs, labeled with fluorescein (FITC), and subsequently used to demonstrate potential application for targeting, cell labeling, and for selective photothermal therapy of antigen-expressing cells.

1. Experimental Methods

1.1. Chemicals and Materials.

Gold (III) chloride (≥ 99.9%), silver nitrate (99.99%), L-ascorbic acid (99%), cetyltrimethyl ammonium bromide (CTAB, 99+ %), benzylhexadecyldimethylammonium chloride (BDAC), sodium borohydride (96%), fluorescein (FITC), and poly (acrylic acid) (M_v = 420,000) were purchased from Sigma-Aldrich. N-hydroxylsulfosuccinimide (Sulfo-NHS), 1-Ethyl-3-(3-dimethylaminopropyl carboiimide HCl (EDC) were purchased from Pierce Biotechnology, and 3-(4,5-dimethylthiazol-2-yl)-2,5-diphenyltetrazolium bromide (MTT) cell proliferation assay kit, blocker solution, alkaline phosphatase chromogenic solution(BCIP/NBT) were purchased from Invitrogen; calcien AM stain purchased from BD Biosciences; protein L-peroxidase was purchased from Sigma-Aldrich; and nitrocellulose membrane, 0.2 μm, was

purchased from Whatman. A33 single chain antibody was expressed and purified as previously reported [17].

1.2. Preparation of Au Seeds.

A CTAB solution (1 mL, 0.20 M) was mixed with $HAuCl_4$ (1mL, 0.5 mM) under stirring, to which 120 µL of freshly prepared, ice-cold $NaBH_4$ (0.01 M) was added, leading to a brownish-yellow solution. The obtained solution was stirred for another 2 min and was kept at 25^o C and was used as the seed solution.

1.3. Preparation of Au NRs.

Growth solution was prepared by mixing together 50 mL of 0.20 M CTAB and 0.15 M BDAC, 2.8 mL of 4 mM $AgNO_3$, 5 mL of 15 mM $HAuCl_4$ and 45 mL of Milli-Q water in a 250 mL flask. After gentle mixing and equilibration in a 27-30^o C oil bath, approximately 1 mL of ascorbic acid (80 mM) was slowly added drop-wise until the mixture became colorless. After this color change, ascorbic acid solution was added drop-wise to give a final volume of 1.25 mL. The final step was the addition of 120 µL of the seed solution to the growth solution at 27-30^{o}C. The colorless solution gradually became purple within 10-20 minutes and was allowed to proceed for 2 h. The solution was centrifuged at 10 000 rpm for 15 min to remove excess CTAB and BDAC surfactant. It was further re-suspended and centrifuged twice to remove excess CTAB and then re-dispersed in a final volume of 20 mL Milli-Q water.

1.4. Surface modification of Au GNRs.

CTAB bilayer is dynamic in nature and can desorb resulting in the apparent toxicity of gold nanorods. Moreover, the desorption of the surfactant from the bilayer will decrease the

effective nanorod surface charge and thus may result in irreversible nanonorod aggregation;[18] hence, it is important to mask the CTAB layer for potential biomedical applications.[19] In this work, surface modification of gold nanorods was coated with polyacrylic acid using the following protocol. In brief, 1 mL of GNRs solution was diluted to 10 mL with Milli-Q water. To this solution, 100 µL of 2 µg/mL polyacrylic acid (M_w = 420,000) prepared in a 6 mM NaCl solution (which was sonicated previously for 30 min) was added drop-wise and the resulting solution was stirred vigorously for 6 h. The PAA-coated GNRs were separated by centrifugation in a test tube twice to remove excess polyelectrolyte and then redispersed in 2 mL of PBS buffer (pH 7.4). The colloidal stability of PAA-coated GNRs was compared to the stability of CTAB-capped nanorods after repeated centrifugation and redispersion in buffer solutions and in buffer-ethanol mixture.

1.5. Functionalization of Poly(acrylic) acid-coated Nanorods.

The carboxyl-terminated PAA-coated nanorods were modified by covalently attaching A33scFv single antibody [17] using EDC-NHS chemistry following the manufactures protocols and then fluorescently-labeled with amine-reactive fluorescein (FITC). Particle purification to eliminate excess un-conjugated antibody and fluorescein were carried out in a size exclusion chromatography using FPLC system (Superdex 200 size exclusion column on an AKTA Explorer FPLC, Amersham Biosciences, Piscataway, NJ).

1.6. Dot-blot immunoassay analyses.

A33scFv-GNRs conjugates were analyzed using a colorimetric dot-blot immunoassay to determine the presence and retention of A33scFv native conformation after the attachment of

GNR. This method is useful for screening antibody reactivity against specific antigens and is employed in the production of antibodies, antibody purification, or for routine diagnosis of pathological conditions.[20] In brief, 20 µL of A33scFv-GNRs (1 mg mL^{-1}), 20 µL of GNRs (1 mg mL^{-1}), and 5 µL of A33scFv (0.6 mg mL^{-1}) were spotted on a nitrocellulose membrane and allowed to dry for 1 min. The membrane was immersed in Milli-Q water for 5 min and developed in blocker solution following manufacturer's protocol (Invitrogen). The reactivity of the conjugates were tested against a 5-mL solution of a protein L-peroxidase conjugate (100 µg mL^{-1}), where protein L is known to bind to the F_{ab} region of the antibody. Next, the membrane was incubated in an alkaline phosphatase chromogenic solution (BCIP/NBT, 5 mL), and an intense purple color develops in response to peroxidase catalysis.

1.7. Cytotoxicity and Cellular uptake Studies.

We examined the potential cytotoxicity of PAA-coated nanorods using a colorimetric MTT cell viability assay while cellular uptake was examined using fluorescent-based confocal microscopy analysis. Human colorectal SW1222 cancer cell line were cultured at 37°C in a humidified atmosphere containing 5% CO_2 and grown continuously in Dulbecco's modified Eagle (DMEM) medium (Invitrogen) containing 10% fetal bovine serum (Sigma) and 1% penicillin-streptomycin (Invitrogen) and used for both cytotoxicity and cellular uptake studies. In a cytotoxicity experiment, a 100 µL suspension of SW 1222 cells (10^6 cells mL^{-1}) was plated onto 96-well black-walled plates, grown for 12 h, then treated with an aliquot of increasing PAA-GNRs concentration and maintained at 37°C for 7 h with periodic monitoring. Medium containing gold nanorods not taken up by the cells was discarded; fresh media was replenished and 10 µL of MTT assay component A was added followed by the addition 100 µL of

component B 18 h later. The absorbance of the resultant cell suspension was determined (λ = 595 nm) by using a microplate absorbance reader (Tecan GENios, MTX lab systems, Virginia) and correlated to cell density using a pre-determined standard curve. The absorbance of cell suspensions treated with PAA-GNRs were compared to the untreated wells and its cell viability deduced. For cellular uptake studies, human colorectal cancer cells (SW 1222 and HT 29) were seeded overnight in a 35-mm glass bottom flask at density of 10^4 cells in a humidified incubator.[21] Cells designated for non-targeted cellular uptake were subsequently treated with excess A33scFv in phosphate buffer (PBS, pH 7.4) for 4 h to block the extracellular A33 antigen receptors and was used as a control. The seeded cells were treated with 60 µL of 2 mM FITC-labeled A33scFv-GNRs for 6 h after which nanorods not taken up were discarded, washed three times with PBS, and replenished with fresh medium. To allow live-cell visualization, 20 µL of FM 4-64® cell labeling dye (20 µg mL^{-1}, Invitrogen) was added and then further incubated in a 37^{o}C humidified incubator for 30 min. The cellular uptake was visualized by the fluorescence intensity from fluorescein using confocal microscope (Zeiss).

1.8. Photothermal therapy.

The potential application of GNRs for targeted photothermal therapy was investigated by measuring the temperature rise of PAA-GNRs solution (100 µg mL^{-1}, PBS) irradiated using 808-nm continuous wave (cw) laser (5.1 W cm^{-2}) for 10 min. Next, malignant colorectal cancer cell line, SW 1222 cell line, which express A33 antigen was used to study the photothermal therapy effect of targeted nanorods using a HT 29 cells as a control. The cells were grown at concentration of 100,000 cells/well in 35-mm glass bottom culture plates overnight. The monolayers were treated with A33scFv-GNRs conjugates for 5 h in fresh medium. After which

the cells were washed and fresh medium replenished before laser irradiation with a 808-nm laser for 6 min. To find the threshold NIR irradiation intensity for inducing photothermal destruction, the laser power was increased step-wise (n ~ 2.5 W cm^{-2}) while maintaining a fixed irradiation area of 4 mm in diameter. Cell viability after laser irradiation was assessed using a membrane-permeable dye calcein-AM used as a live cell stain. The dye permeates cell membranes and is digested by esterases inside the cytoplasm to produce a green fluorescent calcein dye. Briefly, 40 µL of 10 µM of freshly prepared calcien AM solution was added and incubated for 1 h. The cells were imaged using fluorescence microscope (Olympus BX50) with a green filter. Quantitative analysis of cell death was performed by measuring fluorescence of detached cells using a spectrophotometer (LS-50B) with 470 nm/ 520 nm excitation-emission filter.

1.9. Instrumentation.

The characterization of gold nanorods was carried out by using different experimental techniques. Absorption UV-visible spectra were measured with a Shimadzu spectrometer in a quartz cell with 1 cm path length. Fluorescence spectra were measured with a LS-50B spectrometer (Perkin Elmer) also in a quartz cell with 1 cm path length. The nanorod solution was dried on carbon formvar-coated grids and analyzed in a transmission electron microscopic (TEM, FEI Tecnai G2 F20) with a field-emission gun operating at 120 kV. Dynamic light scattering (DLS) studies and surface charge measurements of gold nanorods before and after polyacrylic acid coating were determined using Malvern Zetasizer Nano ZS (Malvern Instruments). Attenuated total reflectance Fourier transform infrared (ATR-FTIR, Bruker Optics, Vertex 80v) was used to analyze the adsorption of PAA on the nanorod surface. Samples for analysis were prepared by carefully dispersing 100 µL (1 mg mL^{-1}) of nanorod solution onto

a silicon oxide chip, and allowing it to dry in a dessicator for 24 h. Live cell imaging for cellular uptake studies was carried out using LS-510 confocal microscope (Zeiss).

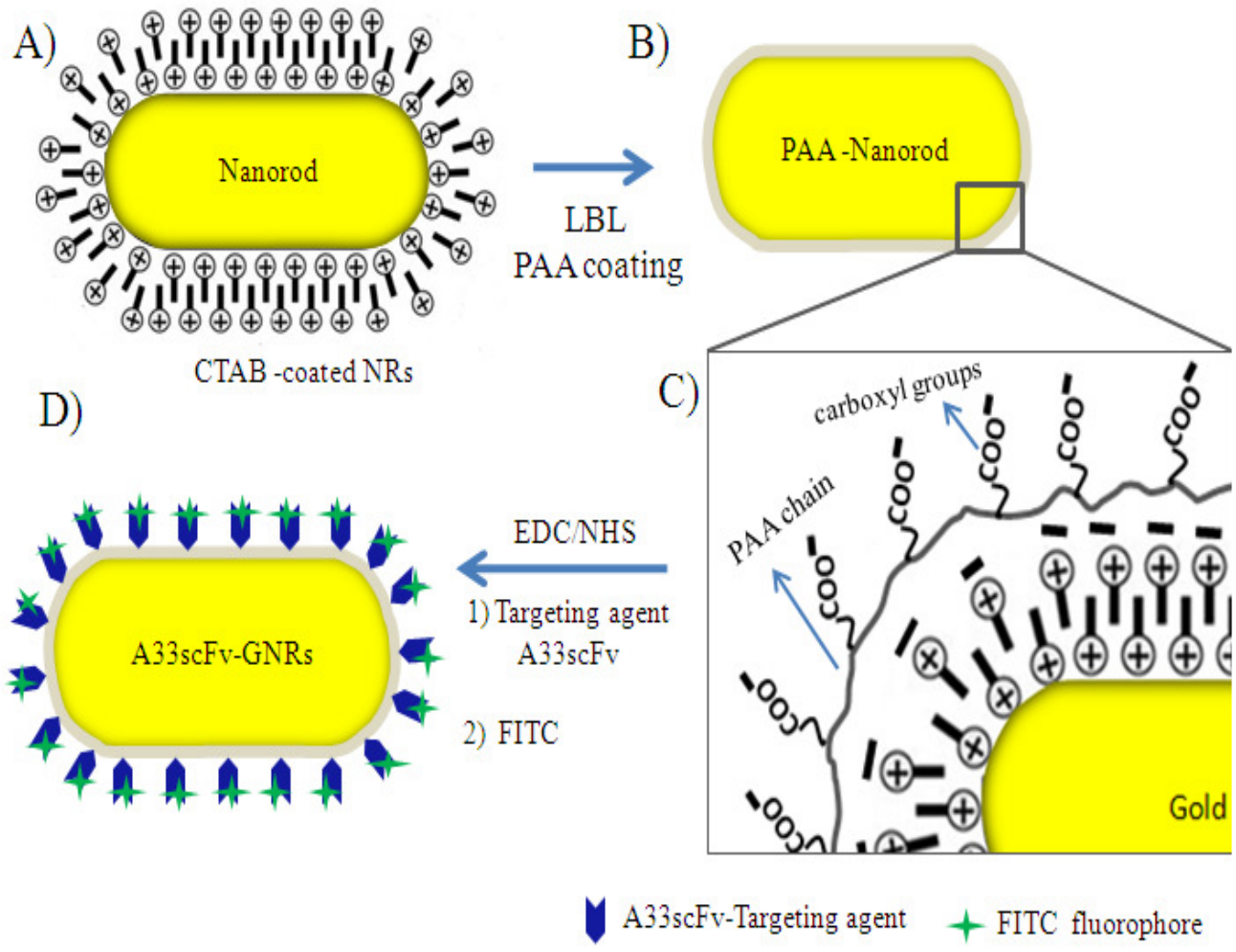

Scheme 3-1: Schematic representation of Layer-by-layer PAA-coating procedure of gold nanorods using polyacrylic acid and subsequent bio-functionalization to prepare molecular probes for cellular labeling.

2. Results and Discussion

Gold Nanorod Synthesis and Characterization. Gold nanorods were synthesized by a seed-mediated growth method using CTAB and BDAC surfactants, as described in the ***Experimental Section***. The polymer coating of the CTAB-stabilized gold nanorods and successive bio-conjugation scheme are shown in **Scheme 3-1.** The seed-mediated synthesis resulted in gold nanorods with an average aspect ratio of 5-6 (length 66 ± 5 and width 11 ± 3 nm), which is consistent with literature reports.[5, 14, 22] Before surface modification and conjugation reactions, the structural and optical properties of CTAB-stabilized gold nanorods were confirmed by transmission electron microscopy (TEM), dynamic light scattering (DLS) and by UV−vis spectroscopy. TEM micrographs and DLS size distribution data showed fairly uniform gold nanorods **(Figure 3-2 (a, b))**. CTAB-stabilized nanorods are positively charged, and their mutual repulsion prevents aggregation and as a result remained stable in the original, high-CTAB content solution for over 3 months. However, the presence of CTAB poses major obstacles in utilizing gold nanorods for biological applications. First, CTAB is a cationic detergent and shows high cytotoxity at the concentrations used for rod synthesis (~ 0.2 M).[23, 24] The cytotoxicity has been attributed to the excess CTAB in solution, and not from the fraction of CTAB bound to the nanonorods. We assumed that through strong electrostatic cationic nanorod-bound CTAB and consequently would reduce cytotoxicity associated with time-dependent desorption of the CTAB surfacant. More importantly, the carboxyl-groups on the polymer chain would provide critical functionality to anchor biomolecules required for various applications. In fact, after incubating the rods with PAA for 6 h, TEM analysis showed monodispersed rods coated with a thin layer (~ 3 nm) of PAA which is shown with uranyl acetate negative staining **(Figure 3-2 (d))**.

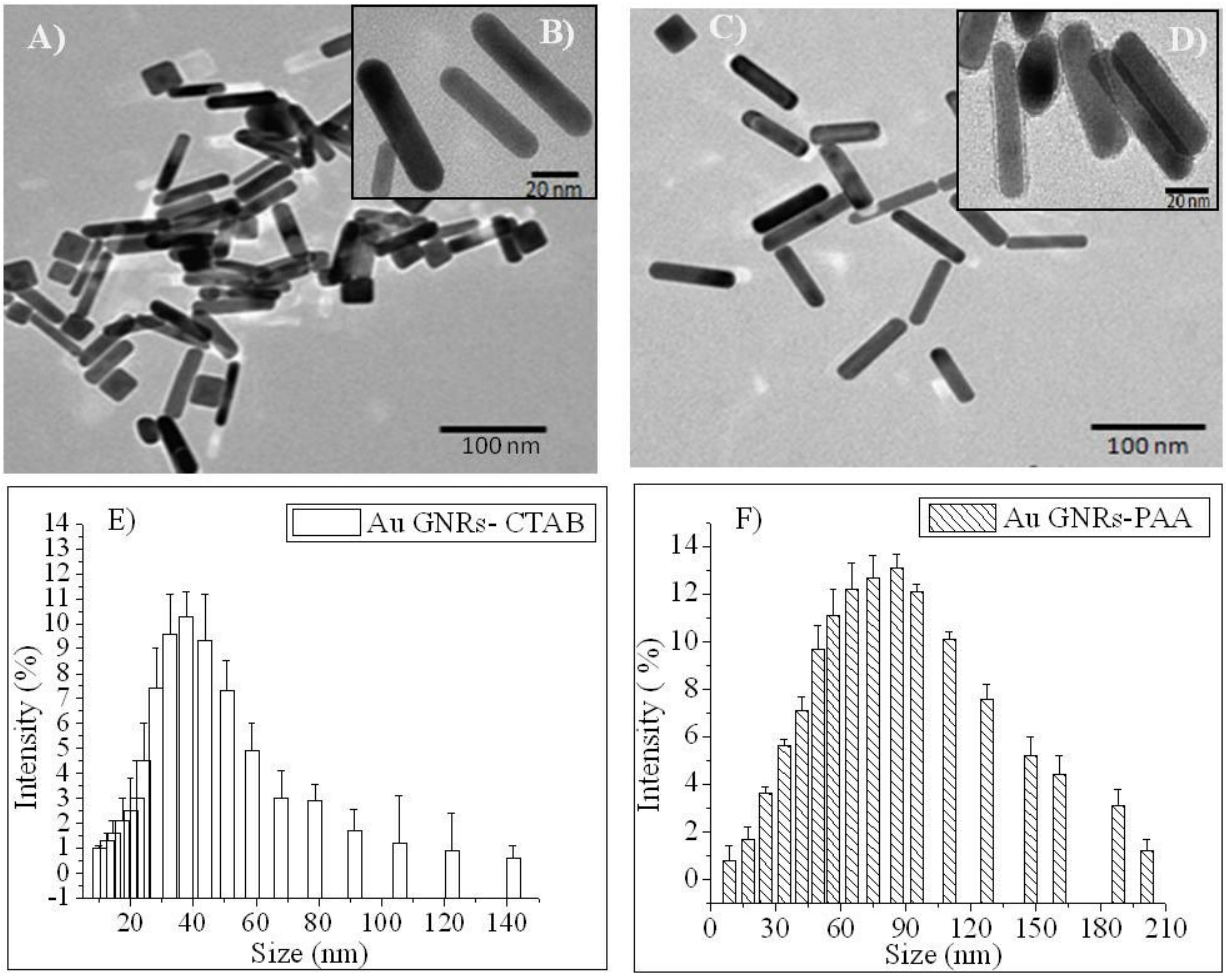

Figure 3-2 : TEM images of as-synthesized CTAB-coated NRs (A); CTAB-coated NRs stained with uranyl acetate showing no apparent surface coating (B); PAA-coated NRs (C); PAA-coated NRs stained with uranyl acetate showing a 3-nm layer of polyacrylate coating (D); DLS size distribution data of as-synthesized NRs (E); and PAA-coated NRs (F).

The uranyl acetate stained images are shown on **Figure 3-2 (b, d)**. Polyacrylate coating is visible on a sample of PAA-coated rods (Figure 3-2 d), but not on **Figure 3-2 (b)** which is a sample of as-synthesized rods. Furthermore, as expected the DLS analysis showed an increase in average hydrodynamic diameter (60 nm) with narrow distribution (**Figure 3-2 (f)**). The DLS size increase as compared to uncoated nanorods takes into account the size of the PAA layer and the timed average diameter of PAA-coated nanorods in solution over the course of the DLS acquisition period. Further FT-IR surface analyses confirmed the adsorption of PAA on the nanorod surface. **Figure 3-3** displays the FTIR spectra of the surface chemistry of these PAA-coated GNRs and the appropriate controls. The characteristic peaks located at 1721 cm^{-1} are unique for vibration mode of the carbonyl (C=O) double bond, 1454 and 1414 cm^{-1} are attributed to C-H_2 scissoring, and the bands at 1270 and 1178 cm^{-1} are caused by vibration of the C-O bond which are all known IR signatures for polyacrylate.[25] The presence of these peaks on PAA-GNRs and their absence on CTAB-GNRs samples confirmed the successful incorporation of PAA on the rod surface (**Figure 3-3 (b, c)**).

Absorption spectra of gold nanorods at different stages of functionalization are shown in **Figure 3-4**. The UV−visible spectra show the transverse and longitudinal plasmon bands of nanorods at 500−550 and 800−900 nm, respectively. The SPR band of as-prepared gold nanorods is observed at 825 nm (**Figure 3-4 (a)**). It is clear from the figure that there is a red shift in the longitudinal band after PAA functionalization to (λ_{max} = 850 nm), about ~25 nm increase with no peak broadening. This suggests that the coating resulted in insignificant nanorod aggregation which is corroborated by the TEM images previously discussed. The increase in the λ_{max} after PAA coating is consistent with changes in local dielectric function from the attachment of PAA. It is known that the absorption and scattering properties of metal

nanoparticles are strongly determined by the local dielectric function.[26] Therefore, the red shift in the peak maxima is probably due to the change in the local refractive index around the CTAB-coated nanorods from water to that of PAA. These observations are consistent with the previous reports on coating of gold nanorods with different polyelectrolytes.[22, 27] The stability of the PAA-capped Au GNRs in PBS buffer solution (pH 7.4) was monitored over a 30-day period. The plasmon spectra of PAA-GNRs at 15 and 30 days after surface coating are shown in **Figure 3-4(b)**, and indicate no significant spectral changes or shift in absorbance due to time-dependent aggregation, and thus, good colloidal stability of the PAA-capped GNRs.

The presence and the stability of PAA coating on the nanorods surface was further analyzed by measuring Zeta (ζ) potential before and after functionalization. As expected, CTAB-stabilized nanorods showed a positive charge (+53.2 mV) on the surface due to the presence of cationic quaternary ammonium groups from adsorbed CTAB, whereas PAA-coated nanorods showed a negative charge (-64.2 mV) surface charge due to the presence of anionic COO^- groups. The stability and potential desorption of PAA from the nanorod surface under physiological conditions was investigated by monitoring changes in Zeta (ζ) potential over 1-week period. The results showed insignificant variations in ζ, suggesting that the adsorbed PAA layer is stabile and can withstand physiological conditions. Further zeta potential measurements showed that the PAA nanorods conjugated with A33 single chain antibody to form A33scFv-GNRs and subsequently labeled with amine-reactive fluorescein resulted in nanorod probes with a higher surface potential (-25.4 mV). The higher surface charge is probably due reduction in the number of surface COO^- groups due to covalent attachment of A33scFv.

CTAB cytotoxicity is well documented and poses challenges to the use of gold nanorods for biological applications.[22, 28] CTAB-coated gold nanorods can kill cells at sufficiently high

concentration primarily due to free CTAB (desorbed or a fraction remaining from nanorod synthesis). In this work, we expected that the PAA coating of the surfactant bilayer would reduce the toxicity of these nanorods because surfactant desorption would be retarded, and excess CTAB from rod synthesis can be removed with successive washing. To investigate our hypothesis, we compared the toxicity of gold nanorod solutions before and after applying the PAA coating using a standard colorimetric assay (e.g., MTT assay) [29] on the SW 1222 cell line, which is a convenient method for evaluating proliferation and cell death in response to external factors. We found that coating the surfactant bilayer with PAA reduced the cytotoxicity and rendered the PAA-coated nanorods biologically nontoxic within the concentration of ~200 μg/mL. CTAB-capped nanorods concentration of ~ 200 μg/mL exhibited marked cytotoxicity (**Figure 3-5**). Similar results have been reported for nanorods coated with other polyelectrolytes such as PSS and PAH.[15, 19] The reduced cytotoxicity have been explained by the retardation effect[30] in which applied polyelectrolyte overcoat reduces the amount of quaternary ammonium surfactant desorbed over time which would ultimately lead to cell death as previously described.

The use of PAH and PSS polyelectrolytes as intermediary surface coatings to passivate or alter surface charge prior to application of a permanent coating such as mesoporous silica coating is widely reported in the literature.[14, 15] However, previous reports on the use of these polyelectrolytes have involved multistep processes and have not demonstrated covalent attachment of biomolecules that are necessary for achieving specific molecular targeting. We expected that using PAA would provide robust colloidal stability as well as allow facile the attachment of various biomolecules through its carboxyl groups. We tested the colloidal stability of PAA-coated nanorods after several rounds of buffer exchanges, increases in salt concentration and centrifugation steps then compared it to CTAB-stabilized nanorods. It was found that the

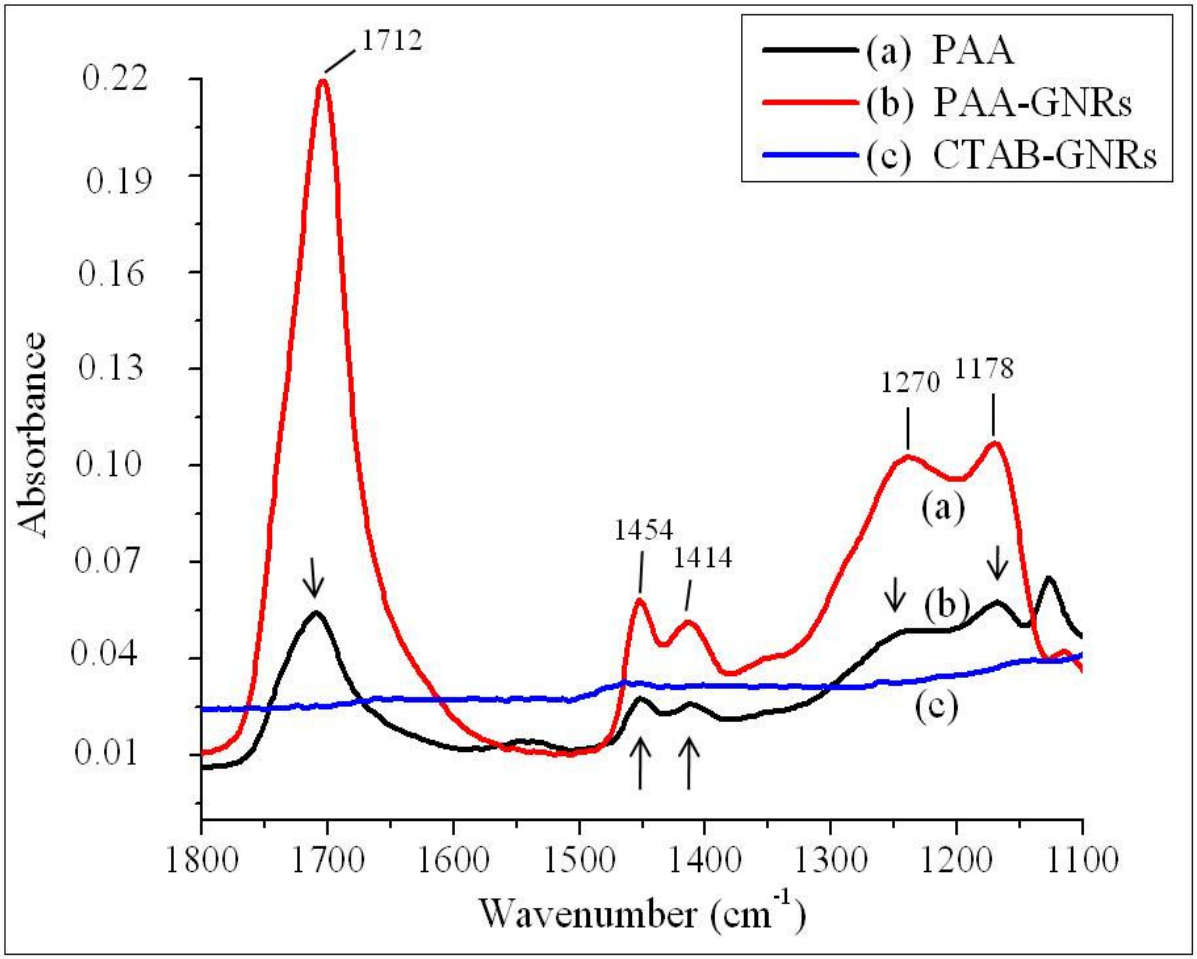

Figure 3-3 : ATR-FTIR spectra of dry Au GNRs solution showing the adsorption of PAA on the nanorod surface; (A) absorbance of dried PAA; (B) PAA-GNRs showing PAA peaks indicated with arrows; (C) as-synthesized Au GNRs coated with CTAB.

PAA-coated nanorods retained its stability whereas CTAB-stabilized nanorods aggregated in each step likely due to the removal of free CTAB in solution, which aids in nanorod stabilization (not shown). These observations confirm previously discussed time-dependent zeta potential measurements in which solutions of PAA-coated nanorods showed insignificant changes in zeta potential over a 1-week period. These findings proved that PAA-coated nanorods are robust with potential uses in various biomedical applications. One of the potential applications of these carboxylated nanorods is for cellular targeting and labeling.

In order to prove that these nanorods can be used to target and discriminately label antigen-expressing cells, we have functionalized the PAA-coated nanorods with targeting antibody specific to colorectal carcinoma cells, labeled the conjugates with fluorescein, and then demonstrated their applicability *in vitro*. Covalent attachment of single chain antibody using EDC-NHS chemistry and successive fluorescein (FITC)-labeling were performed and used to demonstrate cellular labeling. The presence of A33scFv in the antibody-nanorod conjugates was confirmed using a dot blot assay (**Figure 3-6 (a)**). A solution of A33scFv–GNRs conjugates spotted onto nitrocellulose paper developed an intense purple color, which is a colorimetric indicator of the presence of A33scFv in the purified nanorods conjugates; this color change did not occur for purified PAA-GNRs or CTAB-stabilized GNRs. The intense purple color shown in **Figure 3-6 (a)** suggests that successful EDC-NHS coupling chemistry and efficient binding of protein L to the blotted nanorod conjugates. Further, this suggests that the antibody native conformation and active site is unaltered and is useful for cellular targeting applications. Furthermore, colloidal stability of A33scFv-GNRs conjugates was confirmed by obtaining a Uv-Vis absorbance spectrum which showed no further shift with the peak maxima at λ_{max} = 850 nm,

suggesting that the covalent attachment of A33 antibody did not alter the spectroscopic properties of GNRs. Following covalent A33scFv attachment, A33scFv-GNRs conjugates were fluorescently labeled with FITC and then confirmed by measuring its fluorescence (**Figure 3-6 (b)**). The A33-GNRs conjugates showed an excitation at λ_{max} 525 nm compared to the fluorescence of un-conjugated FITC (λ_{max} = 520 nm).

Selective targeting of surface cell receptors using peptides, aptamers, and antibodies have been shown to be critical and has been successfully used to achieve tumor targeted drug delivery, [31] detection and imaging,[32] and efficient photothermal therapy.[1, 33] In this work, we evaluated specific targeting, preferential nanorod cellular uptake, and the potential use of A33scFv-GNRs for photothermal therapy using human colorectal cancer (SW 1222) cell line with A33 antigen surface expression. Under confocal microscopy, colorectal cancer SW 1222 cells incubated with fluorescently-labeled A33scFv-GNRs conjugates **Figure 3-7 (a, b))** exhibit a strong internalized green fluorescence color, which suggests successful binding to A33 surface antigen and subsequent internalization. As a control, SW 1222 cells pre-treated with free A33scFv and subsequently incubated with fluorescently-labeled A33scFv-GNRs did not exhibit fluorescence **Figure 3-7 (c-d)**), which suggests that free A33scFv can block the binding of A33scFv-GNRs in A33 antigen expressed on the tumor cells. Furthermore, incubation of the HT 29 cell line, a human colon adenocarcinoma epithelial cell line with low expression of A33 receptors on the plasma membrane, with fluorescently-labeled A33scFv-GNRs showed very weak fluorescence (**Figure 3-7 (e-f)**). Together, these results suggest that A33scFv-GNRs can specifically target and can lead to selective uptake in colorectal SW 1222 cells.

Gold nanorods are also attractive molecular probes for photothermal therapy application used to induce cell death via hyperthermia. They possess strong absorption in the near-infrared

region and can be used in combination with laser irradiation to achieve selective cell killing. The heating capacity of A33scFv-GNRs was determined by irradiation with 808-nm NIR laser. **Figure 3-8 (a)** show a heating curve of A33-GNRs solution (100 µL, 100 µg mL^{-1}) where +35°C temperature increase after 10 min of irradiation was observed which is consistent with other reported literature values.[34] This result suggested nanorods as efficient thermal converters that can be used for selective photothermal therapy to induce cancer cell death via hyperthermia. Hyperthermia conditions are reached between 42-43°C which causes cell death by direct damage to DNA.[35] Next, we demonstrated selective photothermal therapy *in vitro* using antigen-expressing SW 1222 cell line that were initially treated with A33-GNRs and then irradiated with 808-nm near-infrared laser (5.1 W cm^{-2}). **Figure 3-8 (b, c)** show fluorescent images of SW 1222 cells treated with A33-GNRs followed by laser irradiation and then stained with calcien AM. The presence of green fluorescence indicates live cells and regions devoid of fluorescence indicate dead cells. After laser exposure at 5.1 W cm^{-2} for 5 min, approximately 62 % of the SW 1222 cells were killed, while the viability of HT 29 cells remained almost unchanged (98 %), indicating that the targeted A33-GNRs conjugates are potent photothermal absorbers in cells that express A33 antigen.

3. Conclusion

In this paper, we report on a facile layer-by-layer method of functionalizing gold nanorods in order to reduce cytotoxicity of GNRs that are synthesized by surfactant-mediated method. This single-step coating procedure results in carboxylated nanorods with good colloidal stability, which obviates the need for multistep, time-consuming functionalization strategies widely reported in the literature. We have also demonstrated that the coating strategy produces

polyacrylate-coated nanorods that provide anchors for biomolecule conjugations using simple covalent chemistries. The polyacrylate coating strategy also produces GNRs that are non-cytotoxic as tested *in vitro* at relatively high concentrations (~200 μg/mL) and are therefore suitable for bio-applications.

Biomolecules can be attached as needed to these as-synthesized GNRs for a wide variety of bio-applications. PAA coating allowed facile attachment of single chain antibodies and subsequent fluorescent labeling needed for the fabrication of selective molecular probes for cell labeling and imaging. Further we demonstrated differential of antibody-coated GNRs uptake in antigen-expressing human colorectal carcinoma cells compared to the control cell lines. Experiments showed effective photothermal therapy of colorectal cancer cells when treated with Plasmon resonant A33scFv-GNRs and irradiated with NIR laser for 5 min. The proposed PAA coating protocol can also be extended to conjugate DNA/RNA, proteins, enzymes to monitor cell interactions in living cells as well as to fabricate probes for *in vivo* diagnostics. The nanorods showed good colloidal stability and optimal near-infrared optical absorption with broad *in vivo* applications in imaging and as therapeutic agents.

Acknowledgments

We would like to gratefully acknowledge John Grazul (Cornell Center for Material Research) for his assistance in performing TEM, Will Xia for his help using confocal fluorescence microscope, and Carol Bayles (Life Science core Center) for her assistance with fluorescent microscopy. The authors acknowledge the financial support from the Ludwig Institute for Cancer Research.

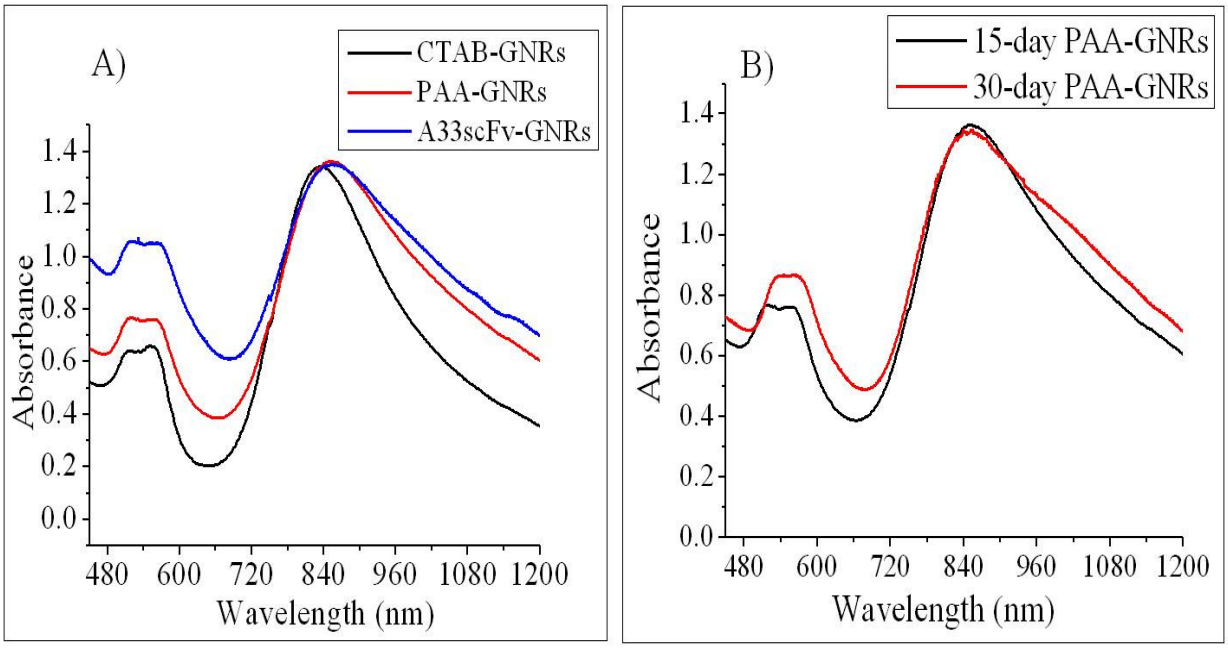

Figure 3-4: Stability of PAA-GNRs over time. UV-vis absorption spectra of as-synthesized gold nanorods (A), PAA-coated gold nanorods (B), A33scFv-GNRs prepared from reaction of PAA-coated gold nanorods with A33scFv.

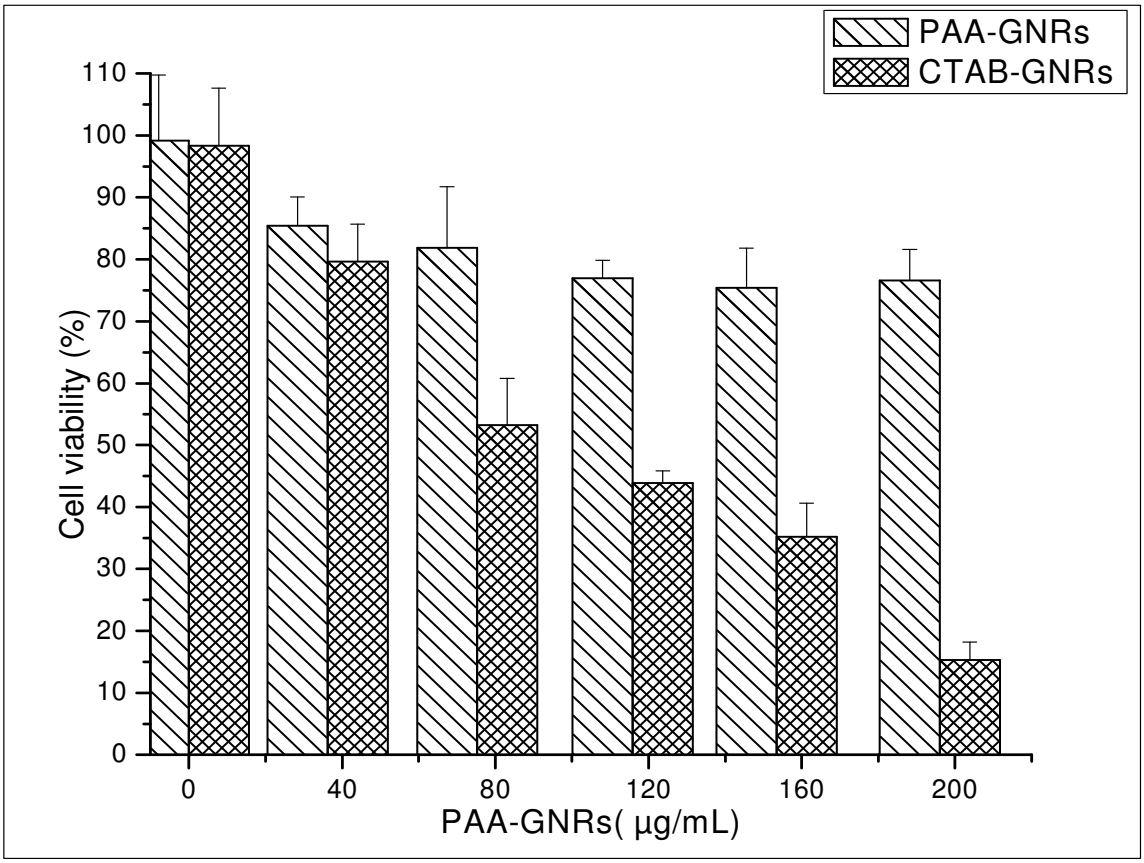

Figure 3-5: Cell viability of SW 1222 cells after incubation with increasing concentration particle conjugates as determined by MTT assay of: (A) PAA-GNRs, (B) CTAB-GNRs. The results show a dose-dependent toxicity with significantly higher cytotoxicity for cells incubated with CTAB-GNRs at higher particle concentration. Error bars represent absorbance variability measured at 570 nm where n = 3.

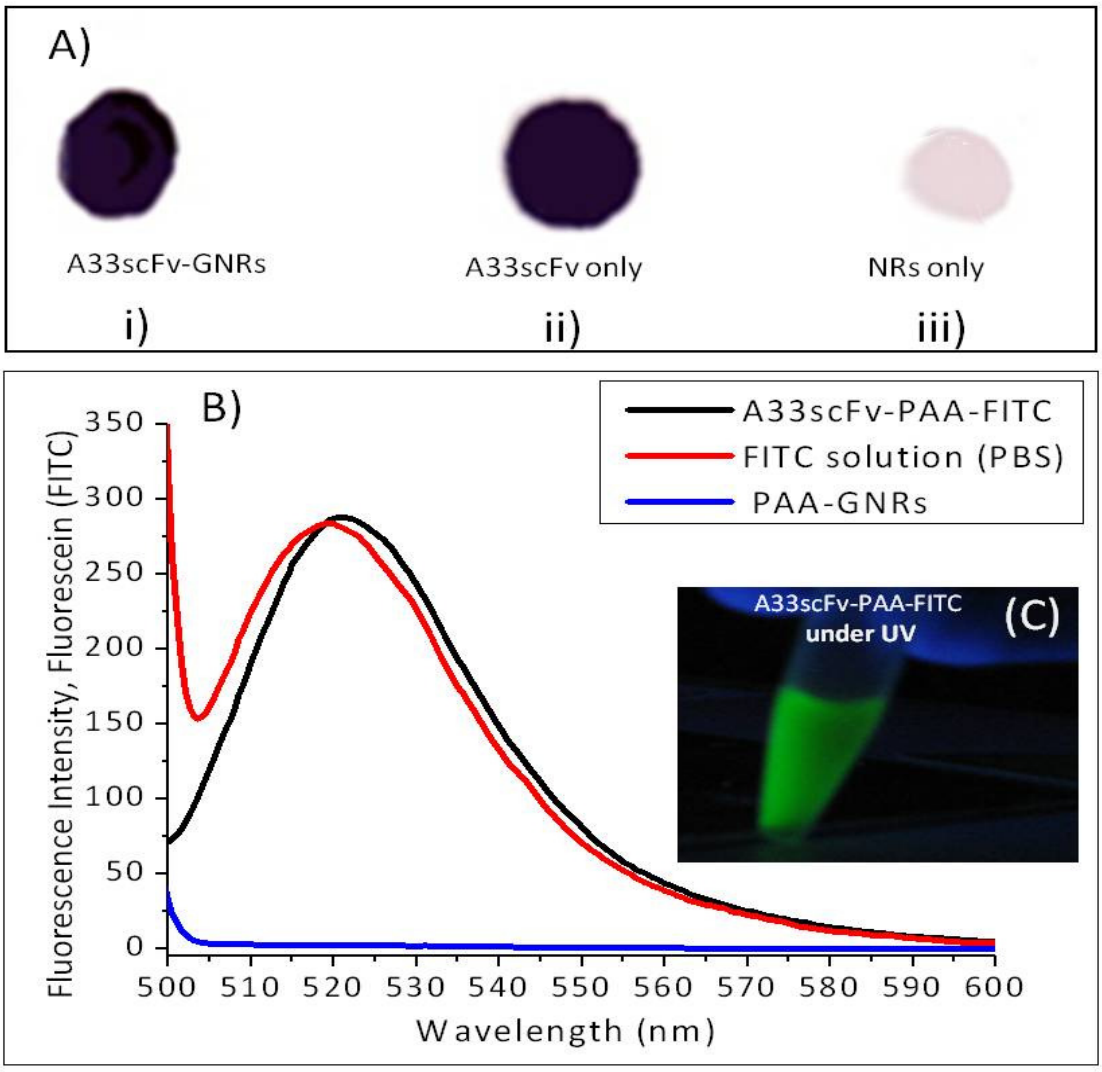

Figure 3-6: Characterization of antibody-conjugated and fluorescently labeled PAA-coated GNRs, (A) Dot Blot assay on nitrocellulose membrane confirming the presence of A33scFv in purified A33-GNRs conjugates (i) show intense purple colored arising from HRP-peroxidase, (ii) positive control (A33scFv), and (iii) negative control showing less intense corresponding to the native GNRs color; (B) Fluorescence of FITC-labeled GNRs antibody conjugates with the corresponding positive and negative control; (C) image of fluorescently-labeled GNRs under UV-light.

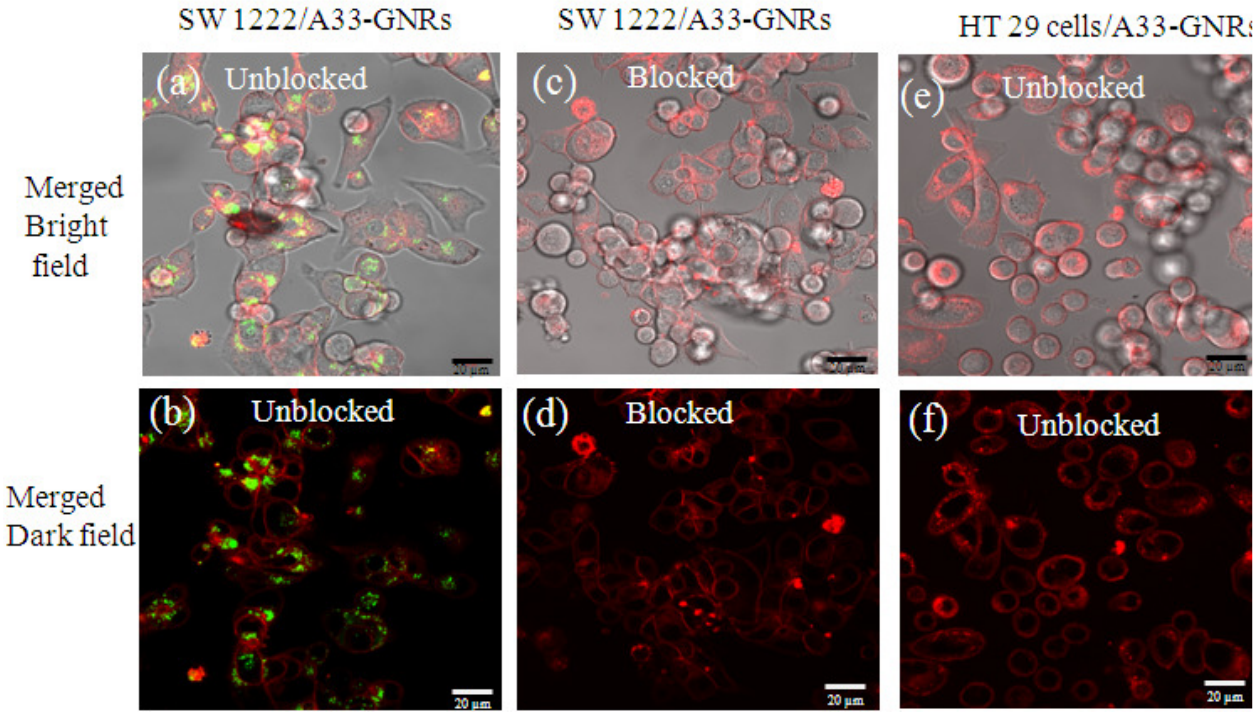

Figure 3-7: Effect of A33 targeting on uptake of PAA-GNRs. Gold nanorods uptake in colorectal carcinoma cells as analyzed by confocal microscopy. (a, b) antigen-expressing SW 1222 cells incubated with A33-GNRs; (c-d) SW1222 cells are incubated with excess A33scFv to block surface receptors and then incubated with A33scFv-GNRs; (e-f) non-antigen expressing HT 29 cell line incubated with A33scFv-GNRs for 5 h; green fluorescence: FITC; red fluorescence: FM 4-64® cell labeling dye; scale bar: 20 µm.

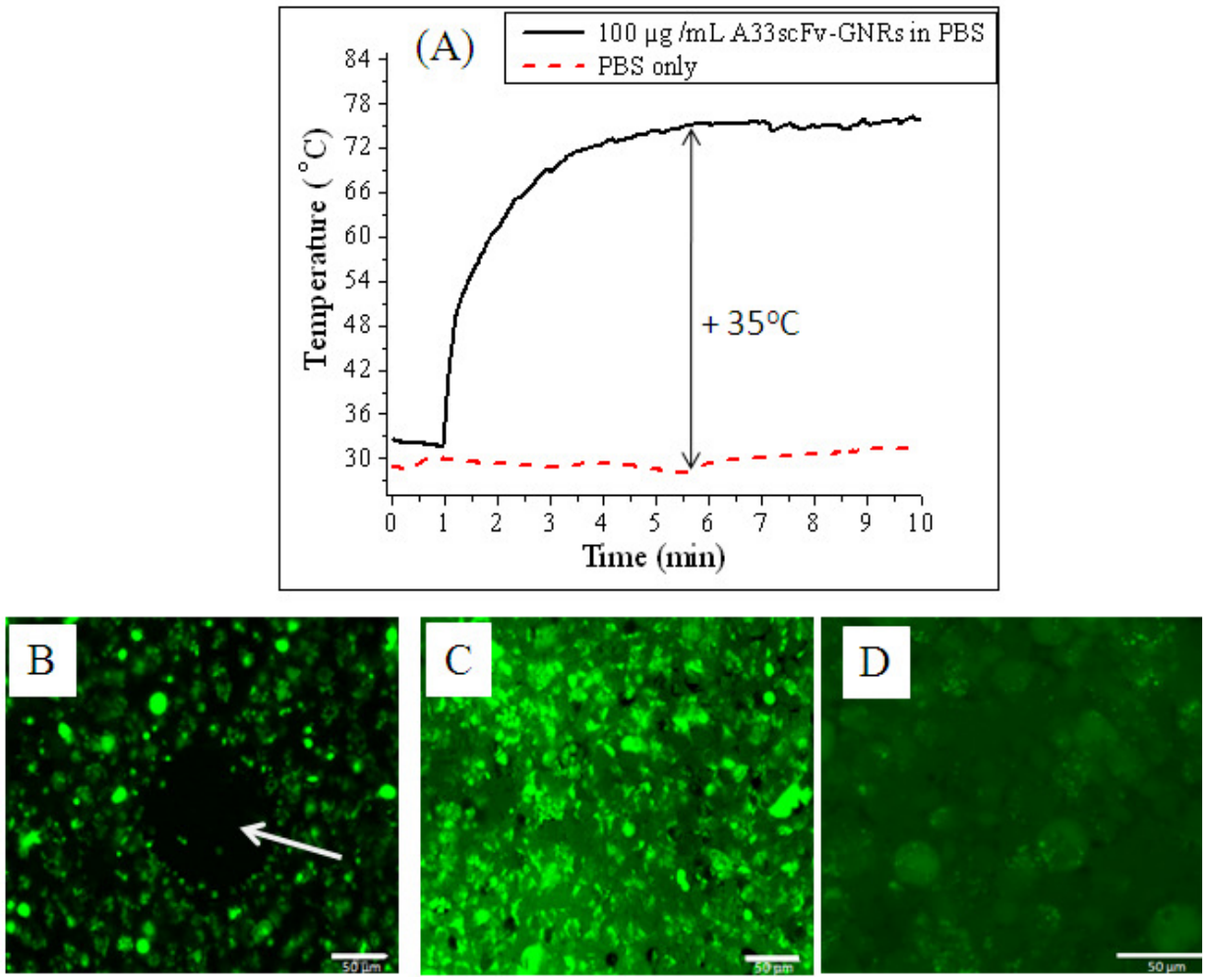

Figure 3-8: GNRs-assisted photothermal therapy of colorectal carcinoma cells using 808-nm NIR laser treatment. (A) Graph shows 35°C temperature increase in a A33scFv-GNRs solution (100 µL ,100 µg/mL) when irradiation 808-nm laser; (B) SW 1222 cells incubated with A33scFv-GNRs (C) SW 1222 cells pretreated with excess A33scFv before addition of A33scFv-GNRs; (D) HT 29 cells incubated with A33scFv-GNRs followed by laser irradiation. Nanorod incubation lasted for 5 h and laser treatments performed at 5.1 W cm^{-2} power density. Viable cells appear green from calcien AM staining while dark areas devoid of fluorescence are cells destroyed from photothermal therapy irradiation. Scale bar 50 µm for all images.

REFERENCES

1. Huang, X.; El-Sayed, I. H.; Qian, W.; El-Sayed, M. A., Cancer Cell Imaging and Photothermal Therapy in the Near-Infrared Region by Using Gold Nanorods. *J. Am. Chem. Soc* **2006,** 128, (6), 2115-2120.

2. Tong, L.; Zhao, Y.; Huff, T. B.; Hansen, M. N.; Wei, A.; Cheng, J. X., Gold Nanorods Mediate Tumor Cell Death by Compromising Membrane Integrity. *Adv. Mater.* **2007,** 19, (20), 3136-3141.

3. Wang, C.; Chen, Y.; Wang, T.; Ma, Z.; Su, Z., Monodispersed Gold Nanorod-Embedded Silica Particles as Novel Raman Labels for Biosensing. *Adv. Funct. Mater.* **2008,** 18, (2), 355-361.

4. Geoffrey von, M.; Andrea, C.; Ji-Ho, P.; Renuka, R.; Michael, J. S.; Hatton, T. A.; Sangeeta, N. B., SERS-Coded Gold Nanorods as a Multifunctional Platform for Densely Multiplexed Near-Infrared Imaging and Photothermal Heating. *Adv. Mater.* **2009,** 21, (31), 3175-3180.

5. Basiruddin, S. K.; Saha, A.; Pradhan, N.; Jana, N. R., Functionalized Gold Nanorod Solution via Reverse Micelle Based Polyacrylate Coating. *Langmuir* **2010,** 26, (10), 7475-7481.

6. Sendroiu, I. E.; Warner, M. E.; Corn, R. M., Fabrication of Silica-Coated Gold Nanorods Functionalized with DNA for Enhanced Surface Plasmon Resonance Imaging Biosensing Applications. *Langmuir* **2009,** 25, (19), 11282-11284.

7. Chen, C.-C.; Lin, Y.-P.; Wang, C.-W.; Tzeng, H.-C.; Wu, C.-H.; Chen, Y.-C.; Chen, C.-P.; Chen, L.-C.; Wu, Y.-C., DNA-Gold Nanorod Conjugates for Remote Control of Localized Gene Expression by near Infrared Irradiation. *J. Am. Chem. Soc.* **2006,** 128, (11), 3709-3715.

8. Li, C.; Wu, C. L.; Zheng, J. S.; Lai, J. P.; Zhang, C. L.; Zhao, Y. B., LSPR Sensing of Molecular Biothiols Based on Noncoupled Gold Nanorods. *Langmuir* **2010,** 26, (11), 9130-9135.

9. Wijaya, A.; Hamad-Schifferli, K., Ligand Customization and DNA Functionalization of Gold Nanorods via Round-Trip Phase Transfer Ligand Exchange. *Langmuir* **2008,** 24, (18), 9966-9969.

10. Alexis, F.; Pridgen, E.; Molnar, L. K.; Farokhzad, O. C., Factors Affecting the Clearance and Biodistribution of Polymeric Nanoparticles. *Mol. Pharmaceutics* **2008,** 5, (4), 505-515.

11. Pastoriza-Santos, I.; Perez-Juste, J.; Liz-Marzan, L. M., Silica-Coating and Hydrophobation of CTAB-Stabilized Gold Nanorods. *Chem. Mater.* **2006,** 18, (10), 2465-2467.

12. Gorelikov, I.; Matsuura, N., Single-Step Coating of Mesoporous Silica on Cetyltrimethyl Ammonium Bromide-Capped Nanoparticles. *Nano Lett.* **2007,** 8, (1), 369-373.

13. Xin, L.; et al., Enhancing fluorescence of quantum dots by silica-coated gold nanorods under one- and two-photon excitation. *Optics Express.* **2010,** 18, (11), 11335.

14. Gole, A.; Murphy, C. J., Polyelectrolyte-Coated Gold Nanorods:Synthesis, Characterization and Immobilization. *Chem. Mater.* **2005,** 17, (6), 1325-1330.

15. Chen, L.-l.; Jiang, L.; Wang, Y.-l.; Qian, J.; He, S., Multilayered polyelectrolyte-coated gold nanorods as multifunctional optical contrast agents for cancer cell imaging. *J. Zhejiang Univ. Sci. B* **2010,** 11, (6), 417-422.

16. Hashino, J.; Fukuda, Y.; Oikawa, S.; Nakazato, H.; Nakanishi, T., Metastatic potential of human colorectal carcinoma SW1222 cells transfected with cDNA encoding carcinoembryonic antigen. *Clin. Exp. Metastasis* **1994,** 12, (4), 324-328.

17. Damasceno, L. M.; Pla, I.; Chang, H.-J.; Cohen, L.; Ritter, G.; Old, L. J.; Batt, C. A., An optimized fermentation process for high-level production of a single-chain Fv antibody fragment in Pichia pastoris. *Protein Express. Purif.* **2004,** 37, (1), 18-26.

18. Sau, T. K.; Murphy, C. J., Self-Assembly Patterns Formed upon Solvent Evaporation of Aqueous Cetyltrimethylammonium Bromide-Coated Gold Nanoparticles of Various Shapes. *Langmuir* **2005,** 21, (7), 2923-2929.

19. Ellen , E. C.; Judith, M.; Anand, G.; Catherine , J. M.; Michael , D. W., Gold Nanoparticles Are Taken Up by Human Cells but Do Not Cause Acute Cytotoxicity. *Small* **2005,** 1, (3), 325-327.

20. Zalis, M.; Jaffe, C. L., Routine dot-blot assay of multiple serum samples using a simple apparatus. *J. Immunol. Methods* **1987,** 101, (2), 261-264.

21. Cortez, C.; Crook, T. E.; Johnson, A. P. R.; Radt, B.; Cody, S. H.; Caruso, F., Targeting and Uptake of Multilayered Particles for Colorectal Cancer cells. *Adv. Mater.* **1998,** 18, 1998-2003.

22. Parab, H. J.; Chen, H. M.; Lai, T.-C.; Huang, J. H.; Chen, P. H.; Liu, R.-S.; Hsiao, M.; Chen, C.-H.; Tsai, D.-P.; Hwu, Y.-K., Biosensing, Cytotoxicity, and Cellular Uptake Studies of Surface-Modified Gold Nanorods. *J. Phys. Chem. C* **2009,** 113, (18), 7574-7578.

23. Connor, E.; Mwamuka, J.; Gole, A.; Murphy, C.; Wyatt, M., Gold Nanoparticles Are Taken Up by Human Cells but Do Not Cause Acute Cytotoxicity. *Small* **2005,** 1, (3), 325-327.

24. Mirska, D.; Schirmer, K.; Funari, S. S.; Langner, A.; Dobner, B.; Brezesinski, G., Biophysical and biochemical properties of a binary lipid mixture for DNA transfection. *Colloid Surf. B: Biointerf.* **2005,** 40, (1), 51-59.

25. Petroski, J.; El-Sayed, M. A., FTIR Study of the Adsorption of the Capping Material to Different Platinum Nanoparticle Shapes. *J. Phys. Chem. A* **2003,** 107, (40), 8371-8375.

26. McFarland, A. D.; Van Duyne, R. P., Single Silver Nanoparticles as Real-Time Optical Sensors with Zeptomole Sensitivity. *Nano Lett.* **2003,** 3, (8), 1057-1062.

27. Yu, C.; Irudayaraj, J., Multiplex Biosensor Using Gold Nanorods. *Anal. Chem.* **2006,** 79, (2), 572-579.

28. Mitamura, K.; Imae, T., Functionalization of Gold Nanorods Toward Their Applications. *Plasmonics* **2009,** 4, (1), 23-30.

29. van de Loosdrecht, A. A.; Beelen, R. H. J.; Ossenkoppele, G. J.; Broekhoven, M. G.; Langenhuijsen, M. M. A. C., A tetrazolium-based colorimetric MTT assay to quantitate human

monocyte mediated cytotoxicity against leukemic cells from cell lines and patients with acute myeloid leukemia. *J. Immunol. Methods* **1994,** 174, (1-2), 311-320.

30. Alkilany, A. M.; Nagaria, P. K.; Wyatt, M. D.; Murphy, C. J., Cation Exchange on the Surface of Gold Nanorods with a Polymerizable Surfactant: Polymerization, Stability, and Toxicity Evaluation. *Langmuir* **2010,** 26, (12), 9328-9333.

31. Sugahara, K. N.; Teesalu, T.; Karmali, P. P.; Kotamraju, V. R.; Agemy, L.; Girard, O. M.; Hanahan, D.; Mattrey, R. F.; Ruoslahti, E., Tissue-Penetrating Delivery of Compounds and Nanoparticles into Tumors. *Cancer Cell* **2009,** 16, (6), 510-520.

32. von Maltzahn, G.; Centrone, A.; Park, J. H.; Ramanathan, R.; Sailor, M. J.; Hatton, T. A.; Bhatia, S. N., SERS-Coded Gold Nanorods as a Multifunctional Platform for Densely Multiplexed Near-Infrared Imaging and Photothermal Heating. *Adv. Mater.* **2009,** 21, (31), 3175-3180.

33. Wu, X.; Ming, T.; Wang, X.; Wang, P.; Wang, J.; Chen, J., High-Photoluminescence-Yield Gold Nanocubes: For Cell Imaging and Photothermal Therapy. *ACS Nano* **2009,** 4, (1), 113-120.

34. Huang, Y.-F.; Sefah, K.; Bamrungsap, S.; Chang, H.-T.; Tan, W., Selective Photothermal Therapy for Mixed Cancer Cells Using Aptamer-Conjugated Nanorods. *Langmuir* **2008,** 24, (20), 11860-11865.

35. Hildebrandt, B. W., P.; Ahlers, O.; Dieing, A.; Sreenivasa, G.; Kerner, T.; Felix R.; Riess, H., The cellular and molecular basis of hyperthermia. *Critical Rev. Oncology/Hematology* **2002,** 43, 33-56.

Chapter 4

Targeted near-IR hybrid magnetic nanoparticles for *in vivo* Cancer therapy and Imaging

Abstract:

The potential of gold-iron oxide hybrid nanoparticles (HNPs) conjugated to A33 single chain antibody used in combination with 808-nm laser irradiation for selective therapy and non-invasive *in vivo* imaging of human colorectal cancer cells in subcutaneous xenograft tumor model is demonstrated. Laser-activated photothermal therapy represents a new, minimally invasive technology with potential uses for selective ablation of malignant tumors. Tumor xenograft models of human colorectal carcinoma cells are used to demonstrate particle localization following systemic injection and to show effective photothermal treatment using near-IR laser irradiation (808 nm, 5 W cm^{-1}) during a 14-day therapy duration. Dumbbell-like gold-iron oxide (6-18 nm) nanoparticles (HNPs) were conjugated with A33 targeting single chain antibody (A33scFv) and shown to selectively accumulate in SW 1222 tumors as compared to their accumulation in non-A33 expressing (HT 29) tumors cells. Particle localization in A33-expressing tumors was observed 12 h post-injection while particle clearance occurred after 24 h after injection. Subsequent photothermal treatment of antigen-expressing tumor cells showing over 65% necrotized cell population, corrupt extracellular matrix and cytoplasmic acidophilia after seven courses of laser treatment (as compared to untreated group). Cell killing was shown

using histological assessment by hematoxylin and eosin (H&E) staining where scar-like structure containing collagen bundles were observed for samples treated with HNPs plus laser irradiation. In contrast, there was no difference in the size or tumor histology in control groups, indicating the laser treatment alone was incapable of causing significant cell killing. In addition, systemically injected HNPs were shown to be effective T2 magnetic resonance (MR) imaging contrast agents where localized particles were detected in the targeted xenograft tumors. These finding suggest that the new class of bio-conjugated hybrid nanoparticles (HNPs) exhibit great potential for dual applications in both therapy applications as well for non-invasive *in vivo* detection using MR imaging.

D.K. Kirui, I. Khalidov, M. Jin, Y.Wang C.A. Batt. Targeted near-IR hybrid magnetic nanoparticles for *in vivo* Cancer therapy and Imaging, Unpublished manuscript, Cornell University.

Current hyperthermic techniques for cancer tumor therapy [1, 2] possess low spatial selectivity in the heating of tumors which causes unintended harm to surrounding healthy tissues. To circumvent this problem, there has been a great interest in the use of gold nanostructures as local heating agents to induce cell death of the targeted cells by hyperthermia. Interest in the use of gold nanostructures for photothermal ablation originates from their surface Plasmon resonance (SPR) effect, a strong enhancement of absorption and scattering of light in resonant with the SPR frequency. These types of materials can convert absorbed photons into thermal energy in a picosecond time scale, causing cell destruction as a result of electron-phonon and phonon-phonon processes [3]. One of the potential applications is to selectively cause thermal heating of biomolecules, cells or tissues and thus cause heat-induced damage of the surrounding materials or cells. This photothermal destruction can be used for disease treatment or cancer therapy. Gold nanoparticles with different shapes and structures, such as gold spherical particles [4, 5], gold nanocages [6], gold nanorods [7], and single-walled carbon nanotubes [8] have shown promise as photothermal therapeutic agents both *in vitro* [5] and *in vivo* [9].

While gold nanoparticles offer distinct optical properties with potential photothermal therapy applications, magnetic iron oxide nanoparticles on the other hand exhibit superparamagnetic properties and have been utilized to make noninvasive molecular probes for disease detection and diagnosis. Magnetic nanoparticles have been employed as magnetic resonance imaging (MRI) T2 contrast agents to provide valuable anatomical information regarding clinical behavior of a disease and treatment response to certain therapeutic modalities [10]. Additionally, iron oxide nanoparticles have been used for thermotherapy of cancer cells using

external magnetic field to induce hyperthermia and to aid in magnetic-guided drug delivery [11, 12]. Combining the magnetic property of iron oxide nanoparticle and the optimal properties of the gold nanoparticle to make a single multifunctional device for both therapy and diagnostics (theranostics) applications has recently garnered great interest. Multifunctional gold-iron hybrid nanoparticles can potentially be used for multimodal imaging, (MRI and CT imaging) [12], therapeutic combinations such as drug delivery and photothermal therapy, and image-guided, minimally invasive intervention [13].

The potential benefits of integrating nanomaterials with a variety of novel properties (such as strong plasmonic behavior, and magnetization) into a single object of nanoscale dimensions have spurred great interest in the development of multifunctional nanomedical platforms for simultaneous targeting, imaging, and therapy administration [14, 15]. These efforts have led to the developments of various types of hybrid nanoparticle systems such as hybrids of iron oxide- quantum dots [16], and various types of gold nanoparticle-iron oxide hybrids [17-19]. For example Kim and coworkers reported multifunctional nanoparticles that exhibit both magnetic and optical properties with potential use for simultaneous targeted phototherapy and imaging using magnetic resonance imaging (MRI) [4]. Iron oxide nanoparticles such as superparamagnetic iron oxide (SPIO) nanoparticles have been extensively utilized as MRI contrast agents to image target tissues *in vivo* in a highly specific manner [20-22]. The SPIO nanoparticles modified with tumor-targeting ligands were used as *in vivo* MRI contrast agents [23] as well as to induce cell apoptosis via hyperthermia [24]. Recently, we reported on the use of novel gold hybrid nanoparticles for targeted photothermal therapy and magnetic-based imaging of colorectal cancer model in vitro [25].

Motivated by the efficacy of these gold hybrid nanoparticles to selectively kill cells in an *in vitro* model, we report on our investigation of systemically delivery of targeted HNPs, application a near-infrared irradiation, activating capability of HNPs and resulting tumor response (as measured by histology and tumor size reduction) using subcutaneous colorectal cancer tumor murine model. Furthermore, we evaluated the oncological efficacy and benign tissue ablation capabilities of this technology as well as their applicability for non-invasive MR imaging detection. To increase the uptake/accumulation in antigen-expressing cells, the HNPs were conjugated to a humanized single chain antibody (A33scFv) to target a A33 antigen expressed in 95% of primary and metastatic human colorectal tumor cells [26], but is absent in most other normal tissues and tumor types [27]. A33scFv, recently produced in our laboratory, has been shown to bind to a transmembrane glycoprotein, A33 antigen expressed in colorectal cancer cells [28]. Advantages of using A33 antigen as localization targets because it is not secreted or shed into the bloodstream and some colon cancer cell lines express large amounts of this antigen, binding almost 10^6 mAb molecules/cell [29]. Consequently, the A33 antigenic system has been the focus of several clinical studies in patients with colon cancers [26, 29].

We have demonstrated particle targeting and localization in subcutaneous (s.c.) human colorectal tumor xenografts using fluorescently-labeled HNPs-A33scFv conjugates. Alexa Fluor® 750, a near-IR dye, was conjugated through the amino-terminal fragment of A33scFv to make stabile HNPs-A33scFv conjugates suitable for *in vivo* near-IR fluorescence imaging. Following particle localization, subsequent laser treatment resulted in effective cell killing as observed by the reduction of tumor volume (in positive control) and confirmed by histological assessment which showed cell damage after seven-course therapy. Targeted HNPs were also detected in the SW1222 tumor xenograft by MR imaging suggesting the potential uses of these

hybrid nanoparticles for therapy applications as well for non-invasive imaging diagnostic applications.

1. Experimental and Methods

1.1. Materials

All of the chemicals were of reagent grade and were used without further purification. N-hydroxylsulfosuccinimide (Sulfo-NHS), and 1-Ethyl-3-(3-dimethylaminopropyl carboiimide HCl (EDC) were purchased from Pierce Biotechnology; Alexa Fluor® 750 succinimidyl ester was purchased from Invitrogen; Matrigel from BD Biosciences(Bedford, MA); SW1222 cells (antigen expressing colorectal cancer cell line) and non-malignant cell lines HT 29 cells were received as a gift from Ludwig Cancer institute of Cancer Research, New York, NY; A33 single chain antibody was expressed in *Pichia pastoris* as previously reported [30]. Six to eight-week old immunocompromised Balb/c nude mice were purchased from Charles River international (Wilmington, Massachusetts).

1.2. Nanoparticle preparation and Conjugation

The dumbbell-like Au-Fe_3O_4 (HNPs) nanoparticles were fabricated as previously described by Yu et *al* [31]. The oleic-capped nanoparticles were encapsulated with carboxy-PEGylated phospholipids (PL-PEG, Avanti Polar lipids), resulting in stabile water-soluble HNPs that we have recently reported [25]. Briefly, the carboxyl-terminated dumbbell-like nanoparticles were covalently attached to single antibody (A33scFv) [30] using EDC-NHS chemistry following the manufacturer's protocols. To study the *in vivo* specific targeting as well as nanoparticle tumor localization, HNPs-A33scFv conjugates were further labeled with amine-reactive Alexa

Fluor® 750, a commonly used near-IR fluorescent dye. Briefly, a 1 mL of purified HNPs-A33scFv conjugates (1mg mL^{-1}, 50 mM PBS) was reacted with 100 µg of Alexa Fluor® 750 in borate buffer (pH 8.5) and allowed to react for 3 h at room temperature. Particle purification to eliminate excess fluorophore was carried out using size exclusion chromatography using FPLC system (Superdex 200 size exclusion column on an AKTA Explorer FPLC, Amersham Biosciences, Piscataway, NJ). HNPs-scFv conjugates were subsequently concentrated to 1 mg mL^{-1} by centrifugation using a 30 kDa microfilter where absorbance measurement (at λ_{600}) was used as a means of monitoring concentration change where absorbance is correlated to particle concentration by beer's law.

The formation of fluorescently-labeled HNPs-scFv conjugates was confirmed by obtaining a fluorescence spectra using SLM Aminco spectrofluorometer (SPF-500C, SLM instruments, Inc.). The fluorescent spectrum was compared to the un-conjugated HNPs or the fluorophore alone. To test the potential applicability of HNPs as thermal heating agents to generate heat and cause cellular hyperthermia, serial dilutions of HNPs-scFv conjugates were tested by irradiation with near-IR 808-nm laser and the change in temperature recorded using a Neoplix thermocouple (Neoptix Corp., Woodland Hills, CA).

1.3. Cell Culture and inoculation of mice with tumor cells

SW 1222 and HT 29 human carcinoma colorectal cells were cultured in Dulbecco's modified Eagle medium (DMEM), supplemented with 10% fetal bovine serum (FBS), 1% penicillin-streptomycin (P/S, 100 units/mL penicillin, and 100 µg/mL streptomycin) in a 5% CO_2 humidified atmosphere. Prior to use, the cells were trypsinized, counted, and resuspended in 100 µL PBS and 100 µL of Matrigel (BD Bioscience, Bedford, MA). Balb/c nude mice 6-10

weeks of age were subcutaneously (s.c.) injected in the hand left and right flanks with 5 x 10^6 cells SW 1222 (200 μL) and HT 29 cells, respectively. Tumors were allowed to grown to about 6-7 mm in diameter before particle injection, imaging, and phothermal therapy treatment. All animal experiments were conducted in accordance with the Guidelines for the Care and Use of Research Animals established by Institutional Animal Care and Use Committee (IACUC) of Cornell University (Ithaca, NY) and in compliance with Federal and New York State regulations.

1.4. Intratumoral nanoparticles accumulation and Imaging

To assess the intratumoral active accumulation of HNPs-scFv conjugates, Balb/c tumor-bearing mice were anaesthetized with isoflurane and injected with fluorescently-labeled HNPs-scFv conjugates (1 mg mL^{-1}, 200 μL) through the tail vein. Particle localization due to active antibody targeting was monitored using Olympus OV100 fluorescence microscope imaging system (Olympus) equipped with a near-infrared CCD camera. At various time intervals, the fluorescence intensity from HNPs-scFv conjugates was acquired up to 72-h post-injection. At specific time points, mice samples with localized fluorescence on the antigen-expressing xenograft were sacrificed and tumors were prepared for histology staining and assessment. The localization of particles in xenograft tumors was confirmed by Prussian blue tissue staining which stains for the presence of iron.

1.5. In vivo near-infrared Photothermal therapy treatment

Nude mice were subcutaneously inoculated with 5 x 10^6 SW 1222 cells in the rear right flanks were allowed to grown for about 21 days before the experiment. When tumors had grown to 6-10 mm in diameter, mice were randomly allocated into three groups I, II, and III (*n* =

3). Each of the mice in group I were systemically injected with 200 µL of HNPs-A33scFv conjugates (1 mg mL^{-1}) and allowed to localize in the tumors before therapy application. Mice in group II were used as control and were untreated with neither laser nor particles whereas group III were injected with saline buffer and treated with laser using the same laser settings as used in group I treatment. Mice were anesthetized with injection of 300 µL of 2.5% tribromoethanol (20 µL/g Avertin, Sigma-Aldrich) solution that kept the animal anesthetized for about 30 min. To explore hematologic effects of laser therapy, each of group were exposed to therapeutic tumor irradiation protocol under anesthesia (~ 5 W/cm^2, 6 mm dia., 30 min) for a total of seven rounds of therapy in the course of a 14-day period. As positive controls(group I), tumor-bearing mice injected with HNPs-scFv conjugates (1 mg mL^{-1}, 200 µL) and allowed 12 h to localize in the tumor prior to laser treatment. Negative control tumor xenografts were injected with 200 µL of saline buffer (PBS) followed by laser treatment (group III) or treated with laser without prior administration of HNPs or PBS (group II). The tumor reduction resulting from application laser over the course of 14-day period was compared to the reduction in tumors where laser only was applied or were untreated.

The laser settings and the duration of treatment were obtained through a set of experiments that involved localized (intratumoral) HNPs injection at tumor site followed by application of incremental laser power over two rounds of laser therapy. These experiments were necessary to determine the power dosage and duration required for effective therapy in tumors with localized HNPs but causes minimal damage to tumors without HNPs. As positive control, 15 µL of HNPs (PBS, pH = 7.4) were injected into tumor bed and irradiated within 2 min of injection with laser powers starting at 3 W cm^{-2} (increments ~ 1.5 W cm^{-2} in 6 mm dia.). Control tumor sites were injected with 15 µL of 50 mM PBS and then irradiated with the same

power settings used in the positive control. Histological analyses and comparison of tumors from positive controls with HNPs versus the tumors injected with saline buffer were used to determine the optimal laser irradiation and settings for therapy following intravenous particle injection and subsequent localization.

1.6. Laser Treatment Protocol

For intravenously injected HNPs, laser treatments were performed ca. 12 hours post-injection to allow particle localization and intratumoral penetration of HNPs-scFv conjugates. Before laser activation the skin at the tumor site was swabbed with polyethylene glycol as an index matching agent to maximize laser penetration. A near-IR 808-nm laser (built in-house) was calibrated before each use. At day 0 the near-IR laser was aimed at the tumor bed for 20 minutes using a 200 x laser fiber passed through a standard focusing lens. The treatment was administrated for a total of seven courses (every 48 h for 14 days) after intravenous injection and localization of HNPs-scFv conjugates or appropriate controls.

1.7. Histological Examination

Histological analyses of xenograft tumors were performed to confirm the presence of HNPs localized in the tumors resulting from the use A33scFv as an active targeting agent and also to analyze the dose-dependent of applied laser therapy. After intratumoral localization, as observed by optimal near-IR fluorescence imaging, xenograft tumors were harvested and prepared for Perl's Prussian blue staining for iron detection. Xenograft tumors harvested before HNPs injection were used as control for Perl's Prussian blue staining. Following tumor resection, the xenograft samples were fixed overnight in 4% paraformaldehyde solution. Tissue

samples were sliced into 5-μm thick sections and then incubated with 2% potassium ferrocyanide in 6% hydrochloric acid for 30 min. For Perl's Prussian blue staining, cells were fixed with 4% paraformaldehyde, followed by incubation in freshly prepared solution of 2% potassium ferrocyanide in 2% HCl for 20 min and counterstaining with 1% neutral red. Images of the tissue sections were acquired using BX60 Olympus microscope.

Histological assessment of tumor samples to assess the efficacy of photothermal therapy was performed by hematoxylin and eosin (H & E) staining. Xenograft tumor tissues were collected from tumor-bearing mice before or at the end of *in vivo* therapy experiments. The samples were sliced into 10 μm sections, fixed in 4% paraformaldehyde, and stained with H & E. The morphological changes resulting from therapy were evaluated by light microscopy using BX60 Olympus microscope. To quantify the level of presence of HNPs in xenograft tumors, three different regions of interest (ROI) with 0.50 mm^2 area were sampled on the acquired microscopy images with Prussian blue staining (**Figure 4-5**) and H &E stained images (**Figure 4-7**). Specific colors (blue for presence of iron in Perl's Prussian staining; blue for endothelium, red for nucleus for H&E stained cells) were extracted and intensities measured using ImageJ 1.41 (NIH).

1.8. MR Imaging of Intravenously-injected HNPs

To demonstrate the potential use of HNPs as MRI T2 contrast agents, 200 μL HNPs-A33scFv (1 mg mL^{-1}) conjugates were intravenously injected allowed for 12 h to circulate and localize at the tumor sites before acquisition of magnetic susceptibility measurements. The mice were euthanized by intraperitoneal injection of 2.5% tribromoethanol (20 μL/g Avertin), trancardially perfused with 50 mM PBS (pH = 7.4), and fixed in 4% paraformaldehyde.

Prepared mice were scanned on a 7T scanner (Bruker BioSpin, Biospec 70/30 USR) with 3D FLASH sequence. Imaging parameters were as follows: TEs (echo time) 5 ms, 6 ms, 30 ms, 35 ms; TR (repetition time) 35 ms; excitation pulse angle 15°; matrix size 150 x 150 x 100; voxel size 200 μm^3 isotropic; NEX 1. A 3D Fourier transform was applied to the raw k-space data to reconstruct the images. The T2 contrast capability of HNPscFv conjugates in xenograft tumors were quantified by comparing the contrast of SW1222 tumors (right flank) and HT-29 (left flank). 3-D tumor segmentation and T2* quantification was performed using (ITK SNAP 2.0) program and the standard error represent (n = 3) for each group.

Statistical Analysis

Three mice per each group were used for comparison using an analysis of variance. Differences between experimental groups were considered to be statistically significant at $p < 0.05$. All values were expressed as arithmetic means ± s.d. (standard deviation). Data were expressed as mean ± standard deviation of n smaller than triplicates, and analyzed for statistical significant. Unpaired student's t-test was used to determine statistical significance (**Figure 4-6**). One-way ANOVA was used to compare variations in the mean tumor sizes at different treatment timepoints in the various treatment groups (**Figure 4-7**).

2. Results and Discussion

2.1. *Nanoparticle Conjugation and Characterization*

We have previously reported the synthesis and functionalization of 6-18 nm gold-iron oxide hybrid nanoparticles (HNPs) resulting in stabile, biocompatible nanoparticles (**Figure 4-1 (a)**). The HNPs showed enhanced optical absorbance in the near-IR region as compared to

homofunctional iron oxide nanoparticles of comparable size which suggests that they can be used for photothermal therapy (**Figure 4-1 (b)**). To prepare nanoprobes for targeted delivery, the carboxylated HNPs were conjugated to A33scFv and were subsequently tested using an *in vitro* human colorectal cancer model for specific targeting and photothermal therapy. We further demonstrated HNPs as potential multifunctional nanoparticle platform for magnetic resonance imaging as well as thermal agent for phototherapy therapy [25]. Here, we have prepared HNPs-scFv conjugates with the goal of testing the probes for localized targeting and photothermal therapy using colorectal cancer xenograft tumors. First, the HNPs were labeled with near-IR fluorophore through the reaction of amino-terminal antibody with Alexa Fluor® 750 succinimidyl ester resulting in stabile nanoparticle-antibody conjugates with good optical fluorescence properties (**Figure 4-2 (a)**). The fluorescently-labeled HNPs-scFv conjugates showed an emission fluorescence peak at (λ_{max} = 750 nm) whereas the un-conjugated HNPs showed no fluorescence.

2.2. Photothermal Conversion of NIR irradiation into heat

Since the ultimate the goal is to use localized HNPs conjugates to cause heat-induced cell death, we have tested the ability of HNPs to convert laser energy into thermal energy by irradiating serial dilutions of HNPs-scFv conjugates with 808-nm continuous-wave diode laser. Solutions of HNPs-scFv conjugates (100 μL of 0, 0.5, 0.2, and 0.1 mg mL^{-1} HNPs) were irradiated and changes in temperature recorded using a thermocouple (Neoplix, Woodland Hills, CA). **Figure 4-2 (b)** shows the temperature change of an aqueous solution containing HNPs as a function of exposure time. It can be seen that the HNPs are various concentrations rapidly converts laser energy into heat, due to electron-phonon and phonon-phonon process [5]. Laser

exposure of 0.5 mg mL^{-1} aqueous solution of HNPs to the NIR laser light (5.0 W/cm^2) for 10 min elevated the temperature of the solution from 25 to 54 °C (an increase of 29 °C). Under the same conditions, minimal temperature change was observed in saline buffer (PBS). The magnitude of the increase in the temperature of the aqueous solution of HNPs decreased with decreasing HNPs concentration (**Figure 4-2 (b)**). This temperature increase suggests HNPs as thermal agents that can be used for selective photothermal therapy to induce cancer cell death via hyperthermia which is attained when the temperature is between 42-45^oC and can cause cell death by direct damage to DNA [32]. In comparison to our recent report on photothermal applications using gold nanorods (NRs) [33], the new HNPs displayed similar photothermal conversion efficiency. For example, the temperature of an aqueous solution of 11 by 66 nm gold NRs increased by 35 °C over a period of 10 min at an output power of 5.1 W/cm^2. Similar nanoparticle-assisted temperature heating has observed for gold nanorods [34], carbon nanotubes [35] as well as for graphene nanoparticles [36].

2.3. Intratumoral particle accumulation

Most nanoparticles between the sizes of 10-200 nm are expected to accumulate in tumors by enhanced permeation and retention (EPR) effect because of leaky tumor vasculature and highly permeable blood vessels of tumors resulting from the rapid growth and porous angiogenesis. This property has been used to passively and preferentially localize nanoparticles and therapeutics with a number of therapeutics based on EPR effect are already been FDA-approved for clinically applications [37]. Additionally, tumors are characterized by dysfunctional lymphatic drainage that helps the retention of nanoparticles in tumor long enough to allow local therapy application and eventual nanoparticle disintegration [38]. Besides using passive targeting

as means of concentrating nanoparticles in the tumor site, active research focuses on using active targeting agents such as antibodies for more efficacious therapeutic delivery systems. In this report, we have used specific A33scFv targeting to achieve preferential in subcutaneous colorectal tumors that express A33 surface antigen. The intratumor accumulation was demonstrated using near-IR fluorescence imaging in live animals. The fluorescence images obtained at different time point after intravenous injection of fluorescently-labeled HNPs-scFv conjugates (200 μg in PBS, pH = 7.4) are presented in **Figure 4-3 (a).** Initially after injection, majority of fluorescence (HNPs) were observed in the liver potentially due of macrophage capture and clearance of these particles. Significant cell surface labeling and particle localization, as evidenced by increased fluorescence intensity, in the antigen-expressing SW 1222 tumor xenograft (right flank) was observed 12-hr post-injection. In contrast, there was minimal fluorescence (particle accumulation) in the non-antigen subcutaneous HT29 tumors (left flank). Gradual particle localization was observed where optimal particle accumulation, as inferred by fluorescence intensity, was achieved at ca. 12 hr post-injection while particle clearance was observed at 36 hr where majority of the excreted particles appeared in the bladder. Whole body imaging of HNPs localized to SW 1222 xenograft over the time course of 30 min to 72 h postinjection showed that the peak accumulation occurred at 12 hr post-injection which was followed by gradual decrease over 36 hours and complete clearance after 72 hours (**Figure 4-3 (b)**).

2.4. MR Imaging of mice

The potential use of HNPs as contrast agent for non-invasive MR imaging was demonstrated by performing MR images of xenograft mice intravenously injected with HNPs-

scFv conjugates. The mice were sacrificed and transcardially perfused with 4% paraformaldehyde solution in preparation for MR imaging. Next, T_2 contrast capability between subcutaneous antigen-expressing SW1222 xenograft tumors (right flank) which was compared to the contrast in a control HT29 xenograft tumor (left flank). **Figure 4-4 (a)** show T2* contrast images of systemically delivered nanoparticles after 12 h post-injection. The SW1222 tumors appeared darker in comparison to the contrast of HT-29 tumor (left flank) or tumor-bearing mice before particle administration. This is attributed to the localization of HNPs in the targeted tumors which reduces the T2* magnitude and can potentially serve as effective *in vivo* MRI agents. In contrast, there was no apparent MRI signal change in the tumors of mice receiving non targeted HNPs. Notably, signal reductions were also seen in the liver and bladder as can be seen on the MR micrographs where they appeared much darker than the other organs (**Figure 4-4**). The presence of HNPs in the liver is due to macrophage particle capture which was particularly notable shortly after systemic injection (fluorescence) while particle clearance led to the deposition of HNPs in the bladder. 3-D quantitative analyses of the T2* tumor volume showed ~50% reduction in the SW1222 xenograft tumor fluorescent brightness as compared to the brightness of HT 29 xenograft (**Figure 4-4 (b)**). The MR results showing the presence of HNPs in positive SW 1222 xenograft further corroborated earlier particle localization data using optical imaging.

Following tumor resection, the presence of HNPs in targeted SW 1222 subcutenous tumors was further confirmed by direct staining of iron with Perl's Prussian blue staining. Prussian blue staining demonstrated iron-containing sites as blue spots in the cytoplasm. Tumors obtained before and after intravenous injection were prepared, stained with Prussian blue and then compared to each other. The presence of blue stains in SW1222 tumors cells would

confirm that the localization of HNPs and fluorescently-labeled HNPs-scFv conjugates previously observed by live animal imaging. **Figure 4-5 (a)** show representative micrographs of s.c. SW1222 tumors where there were visible and notable blue stains for tumors harvested 12 hours post-injection. In comparison, very few blue stains were observed for tumors harvested before nanoparticle intravenous injection. This is potentially due to the presence of endogenous iron in blood. Similar observation was made for subcutaneous (s.c.) HT29 tumors harvested following intravenous particle injection. The amount of blue stains as by quantified with ImageJ program (NIH) showed that over half of the tumor populations were labeled with HNPs as compared to the control (**Figure 4-5 (b)**). Previous reported literature duration for particle accumulation after intravenous injection have ranged from 30 min for rapidly cleared particles to 72 h for particles with longer blood half-life which may vary depending upon particle properties such as size, charge, and functionalization [39].

2.5. Tumor growth suppression: direct intratumor injection

After observing effective particle homing to human colorectal SW1222 tumors using A33scFv targeting, we subsequently investigated photothermal therapy conditions/settings for tumor growth suppression by laser treatment. To inform the development of near-IR radiation doses needed to destroy tumors, groups of three mice were initially used to determine the optimal conditions such as laser power and treatment duration for near infrared nanoparticle-assisted therapy of SW 1222 tumor xenografts. For each group, 15 μL of HNPs-A33scFv conjugates (1 mg mL^{-1}, PBS = 7.4) were directly administered at three sites within the tumor interstitium (bed) and subsequently irradiated with increasing laser power doses with varying time periods. For control experiment, a group injected with 15 μL PBS and exposed to laser treatment. Each of

this group was treated with increasing laser power and time duration over an extended period and before tumors were harvested and histological studies were performed to determine the effective of laser treatment. For these studies, it was determined that ca. 30 min of irradiation at 5 W/cm^2 with seven courses (14 days) of treatment would be needed to cause cell damage to xenograft tumors with injected HNPs with minimal damage to control xenograft tumors.

2.6. Photothermal therapy in mice

A major hurdle, of cancer therapy is to kill cancer cells without injury to normal or cells, tissues, or organs. We have shown that laser irradiation can induce hyperthermic cytotoxicity with following intratumorally injected HNPs while causing limited harm to the xenograft tumors without HNPs conjugates. Further, we have demonstrated the localization of HNPs-scFv conjugates after ca. 12 h post-injection using A33scFv as a targeting agent. Next, once particle localization was confirmed by fluorescence microscopy, photothermal therapy was performed every 48 h for 14 days (seven-course treatment) with xenograft tumors exposed to laser treatment as demonstrated on **Figure 4-6 (a)**. Mice from each group were euthanized and tumor excised for further analyses where the largest tumors from each group are shown. **Figure 4-6 (b)** show representative micrographs of tumors harvested after 14 days from the different groups, (I) tumors treated with targeted HNPs plus laser, (II) tumors from untreated group, and (III) tumors treated with laser only. From the tumor physical appearance, the control group (I) with targeted HNPs laser treated were the smallest in size, while the tumors treated with laser only appeared insignificantly smaller than non-treated tumors (control groups- II or III).

The effectiveness of photothermal therapy was further quantified by measuring the changes in the tumor volumes over the course of laser treatment. Tumor volume was calculated

using the equation, $ab^2/2$, where *a* represents the longer dimension and *b* represents the shorter dimension of the tumor. Mean values of tumor volumes in each group during treatment are shown in **Figure 4-6 (c)**; error bars correspond to 95% confidence intervals (n = 3 mice per group). From these observations, the tumor volumes of the treatment group (I) after seven-course treatment were significantly smaller than either the group treatment with the untreated group (II) or laser only (III). It is also worth noting that in the first four courses of treatment, the tumors in group (III) were a little smaller than those of control group II (untreated). However following subsequent rounds of laser treatment, the tumors of the laser irradiation group (III) grew to almost equal size to those in the control group II. The tumor inhibition effect in the control group (I) is obvious and confirms the efficacious nanoparticle-assisted therapy using 808-nm laser. The smaller tumor size for control group (III) at the on-set of therapy application may be due to nonspecific heat stimulation resulting from laser irradiation.

Histological analyses of tumor tissues harvested before and after laser therapy were conducted to investigate the cellular effect of laser irradiation combined with targeted particle therapy. Tumors excised from representative xenograft mice were prepared and analyzed by H & E staining. Tissue staining showed healthy, well-vascularized tissues with no apparent cell damage. After the first course of laser treatment (day 1), the tissue morphology remained unchanged with no significant cell damage (**Figure 4-7**). It was after four courses of treatment (day 8), when substantial cell damage (nucleus damage) showing necrotized cells, initial stage of cytoplasmic acidophilia and nucleus shrinkage was observed. This cell thermonecrosis of cells was progressively increased until the seventh treatment (day 14) where bundle-like tissues without cells were observed (**Figure 4-7**). After 14-day therapy, histological examination confirmed that the combination of HNPs administered by either intratumoral (i.t.) or i.v.

injection followed by laser treatment caused significantly greater cell necrotic, corruption of cytoplasm and extracellular matrix than did PBS with laser treatment, or untreated group (**Figure 4-7 (a-f)**). In the positive control group (I) treated with HNPs plus the laser, common features of thermonecrosis such as loss of nucleus, cell shrinkage, and coagulation were found in the tumor tissues where ~ 65% of the tumor tissues were necrotized as was quantified by proportional of cells with intact nucleus(ImageJ, NIH). In control group (III) treated with PBS plus laser, there was only a baseline fraction of necrosis in tumor tissue (< 5%) and there was little pyknosis or karyolysis, confirming the benign nature of laser treatment in the absence of heat-inducing HNPs agents (**Figure 4-7**). Tissue extracted from mice with intratumoral HNPs injection plus laser treatment showed that almost all of the tumor tissue was necrotized, exhibiting pyknosis, karyolysis, cytoplasmic acidophilia, and degradation and corruption of tumor extracellular matrix. This set of experiment was critical in establishing the laser required for effective therapy following i.v. HNPs injection. Thus, selective in vivo photothermal destruction of the tumors mediated by HNPs was confirmed.

It has been assumed that, in photothermal therapy, optical irradiation is absorbed and transformed into heat, inducing thermal denaturing of proteins (and DNAs) in the cell and coagulation of tissue and, consequently, causing irreversible damage to the targeted tissue [40]. As can be seen in **Figure 4-7**, in the sample of the treatment group, extensive cellular injury was observed and the vessels were injured. Various mechanisms account for heat-induced cell death. Specifically, heating up to 39 to 45^{o}C may lead to the acceleration of biological reactions accompanied by the production of shock-heating proteins [41]. The heating process influences DNA polymerase, ligation enzyme and non-histone protein, which blocks DNA synthesis or RNA synthesis [42]. Heat also affects the physical properties of the membrane, especially

permeability and fluidity [43]. Heat-induced cell injury was also viewed as a systemic effect, including membrane blebbing, depolymerization of cytoskeletal filaments, thermal inactivation of membrane proteins and mitochondria, or increased production of heat.

3. Conclusion

In this report we have demonstrated targeting and localization of HNPs following intravenous injection where A33scFv has been proven to be an effective agent for active targeting. Next, the localized HNPs were used to demonstrate the photothermal therapy effect of HNPs upon near-IR irradiation to destroy solid subcutaneous colorectal tumors. Histological analyses (H&E) revealed healthy and well-vascularized tumor xenografts before laser therapy. Particle localization was observed by near-IR fluorescence imaging at 12 h post-injection and confirmed by Perl's Prussian tissue staining. Following, laser therapy, ~65% necrotized cells were observed for control group treated with HNPs plus laser. Laser therapy of tumors with were localized, thermal energy was generated from the optically excited HNPs enough to destroy tumors cells in a non-invasive manner. Success of this site-specific cell killing relies on targeted delivery HNPs-A33scFv constructs into tumor xenografts as well as HNPs-mediated photothermal effect. Additionally, we also showed that the HNPs would be an efficient non-invasive MRI imaging in which the HNPs localization were observed in T2* magnitude and resulted in ~ 50% image darkening. In summary, HNPs can act as an efficient photothermal therapy agent capable of inducing cell death and for non-invasive MR imaging. The combination of small size, strong absorption in the NIR region, and integration of the superparamagnetic iron oxide nanoaparticles into a single device makes HNPs ideally suited for theranostic applications (i.e., MR image-guided PTA therapy). HNPs-scFv showed high uptake in SW 1222 human

colorectal xenografts as a result of enhanced permeability and retention effects and active targeting A33cFv.

We believe our findings motivate future investigation into the long-term bio-distribution of HNPs, more extensive analysis of their potential toxicity *in vivo*, and the development of methods for detecting low concentrations of HNPs in whole animals to remotely quantify i.v. tumor targeting. Methods for actively targeting NRs to tumors, particularly to vascular epitopes, could potentially enhance their specificity for tumors or direct their additional accumulation in premalignant lesions and metastatic lymphatics. Finally, we provide clear evidence that the application of quantitative biodistribution-based modeling to the *in vivo* testing of nanomaterials can provide insight into their function and direct procedural optimization.

3.1. Acknowledgments

The authors thank Xiaoyue Chen, department of Biomedical Engineering for assistance and training on animal handling. They also thank the staff and animal care technogists of Weill Hall Animal facilities in the Department of Biomedical engineering. We thank John Grazul (Cornell Center for Material Research) and Carol Bayles (Nanobiotechnology Center) for their assistance in performing TEM and fluorescence microscopy. The authors acknowledge the financial support from Sloan foundation and the Ludwig Institute for Cancer Research. In addition, we acknowledge Dr Tian Li, department of Radiology at Weill Medical College of Cornell University for MR imaging and Richard Wong for help with MR data analysis.

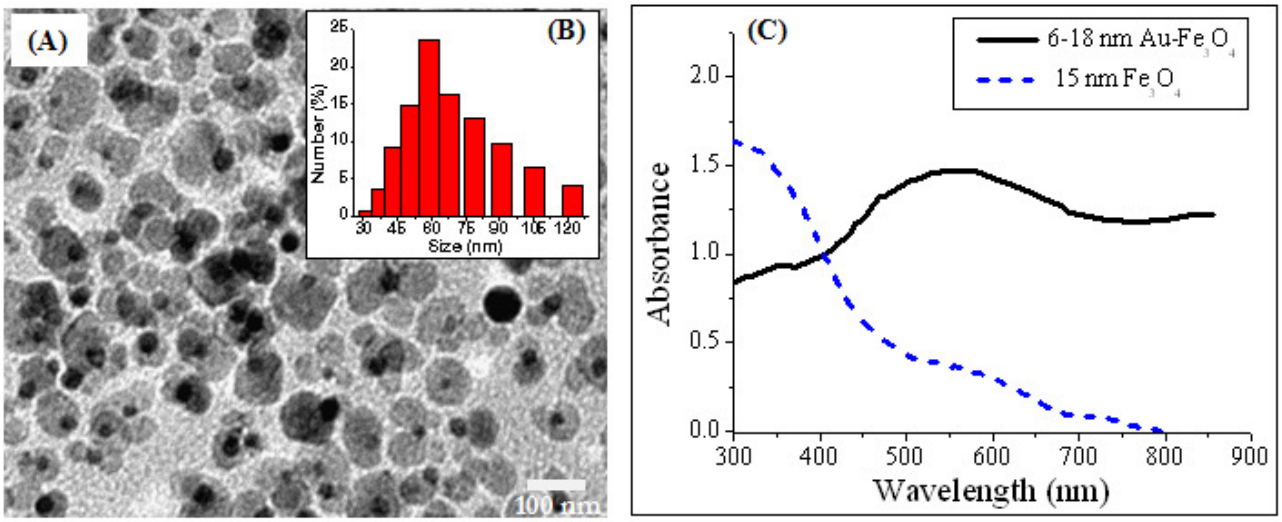

Figure 4-1: Properties of HNPs functionalized with carboxylated phospholipids (DSPEG-COOH). (a) TEM image showing the hybrid nanoparticles (6-18 nm) Au-Fe nanoparticles; (b) Zetasizer measurement showing average hydrodynamic particle size ca. 60 nm after functionalization ; (c) UV-vis-NIR spectra comparing the absorbance of HNPs-PEG to homofunctional Fe_3O_4 nanoparticle.

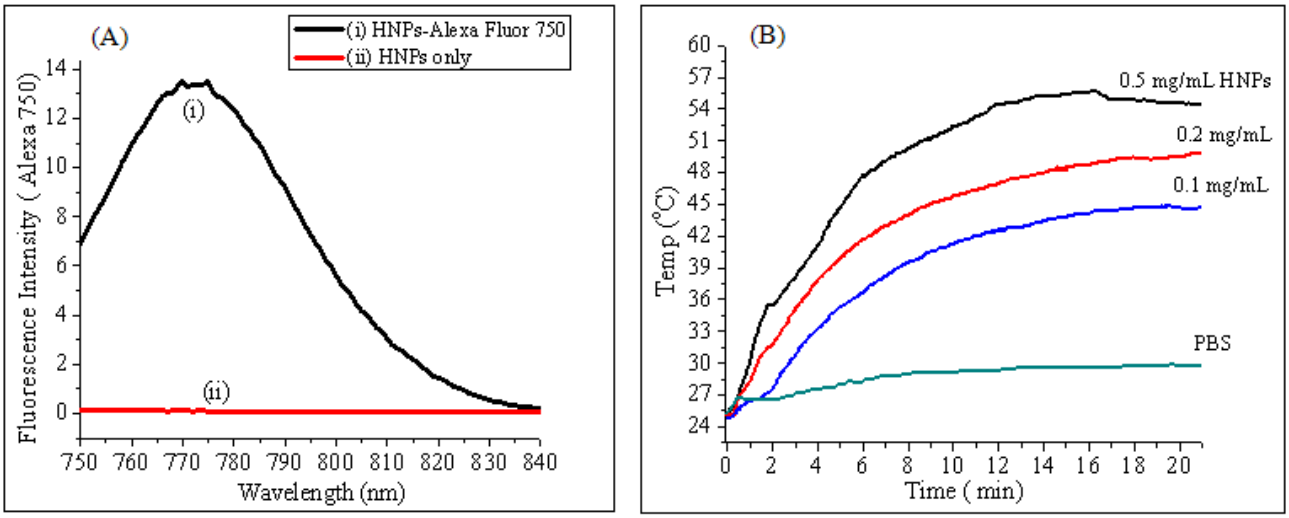

Figure 4-2: HNPs fluorescence and temperature response properties. (a) Fluorescently-labeled HNPs showing appropriate emission at (em= λ_{750})suggesting successful labeling; (b) Temperature change curves of the HNPs solution and the saline buffer exposed to the 808-nm laser at a power density of 5 W/cm^2. Concentration-dependent temperature rise was noted for the HNPs solution, in marked contrast to the PBS temperature which showed little change during the laser irradiation. Temperature change curves of the HNPs-PEG solution and the water exposed to the 808 nm laser at a power density of 5.1 W/cm^2. Rapid raise of temperature was noted for the HNPs-PEG solution, in marked contrast to the water temperature which showed little change during the laser irradiation.

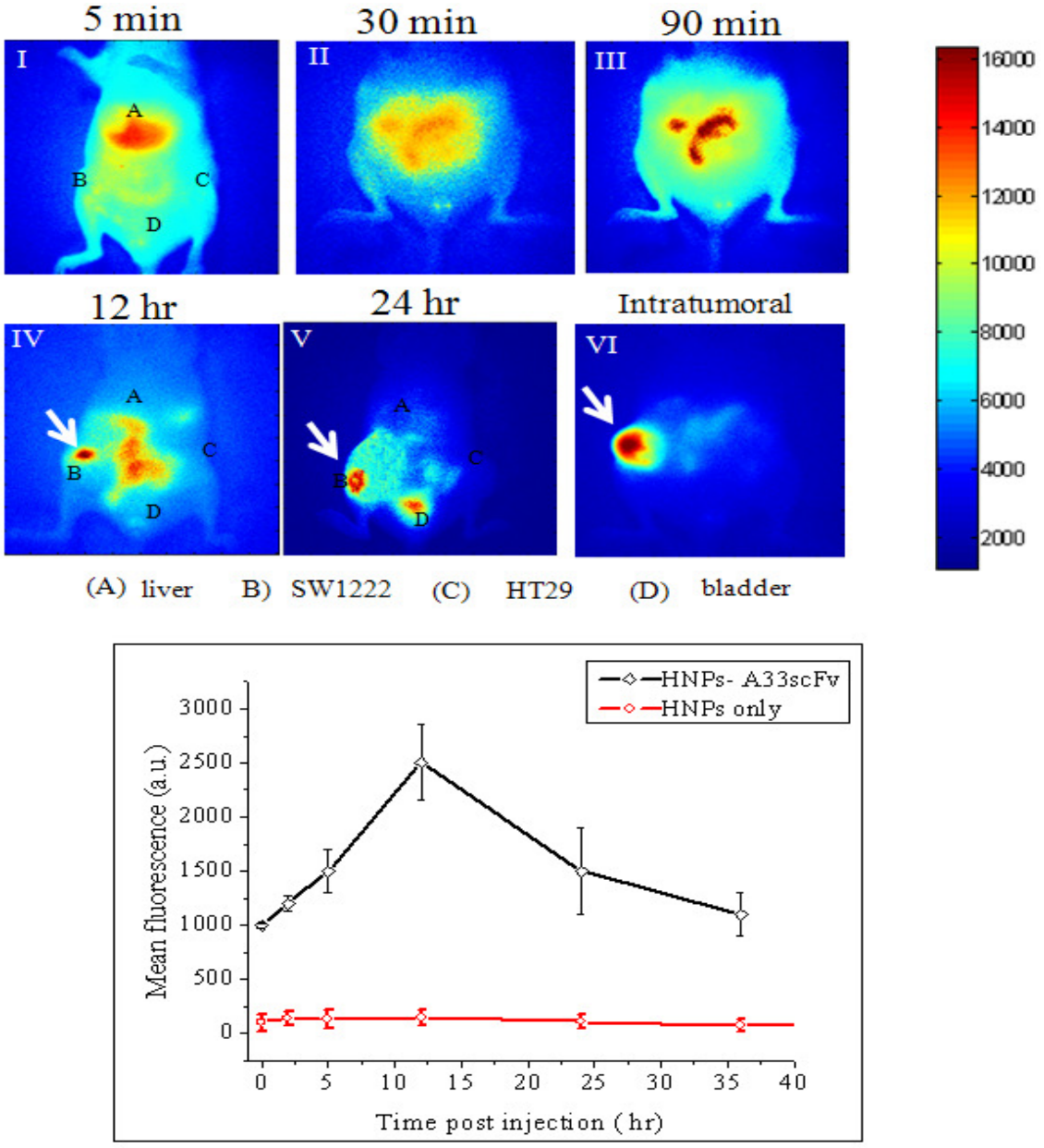

Figure 4-3: Tumor xenograft animal after intravenous injection with Alexa 750-labeled HNPs conjugates. Time dependent images showing near-infrared fluorescence of murine model with subcutaneous tumors with SW 1222 cells (right flank) and HT 29 cells (left flank). Images acquired after systemical injection of fluorescently-labeled HNPs-A33scFv labeled with near- infrared dye, Alexa Fluor 750. Images collected time intervals post injection (A) 5 min, (B) 30 min, (C) 90 min, (D) 24 hr, (E) 36 hr, and (F) intratumoral local injection of 20 µL of HNPs-A33scFv. The intratumoral particle accumulation is evident after 12 h while particles clearance was significant at 36 h post injection.

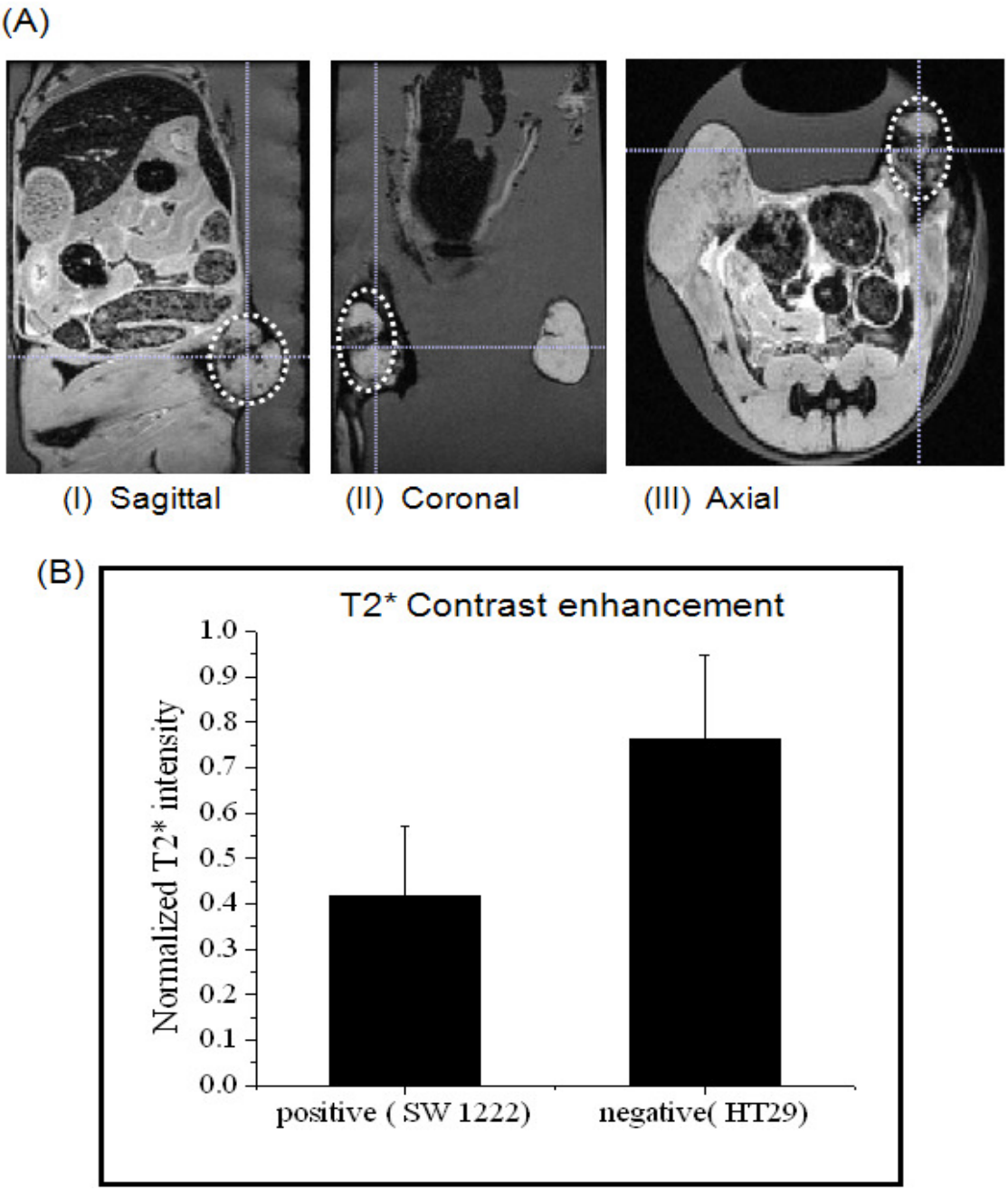

Figure 4-4: *In vivo* T2 magnitude images of HNPs distribution in mice at 12 h after intravenous injection of HNPs-A33scFv conjugates. The contrast enhancement of HNPs is shown on mice- bearing SW 1222 cells (right flank), HT 29 (left flank) colorectal cancer cells. Antigen-expressing tumor (right flank) appears darker due to the T2 enhancement compared to the tumor (hind left flank) as is shown on MR orientations (sagittal (i), coronal (ii), and axial (iii)). Dark spots are identified by T2 mapping as the accumulation of HNPs was indicated with crosshair; (b) tumor brightness as quantified using ITK-SNAP is where positive SW1222 xenograft appeared 50% less bright compared to control (HT29 cells).

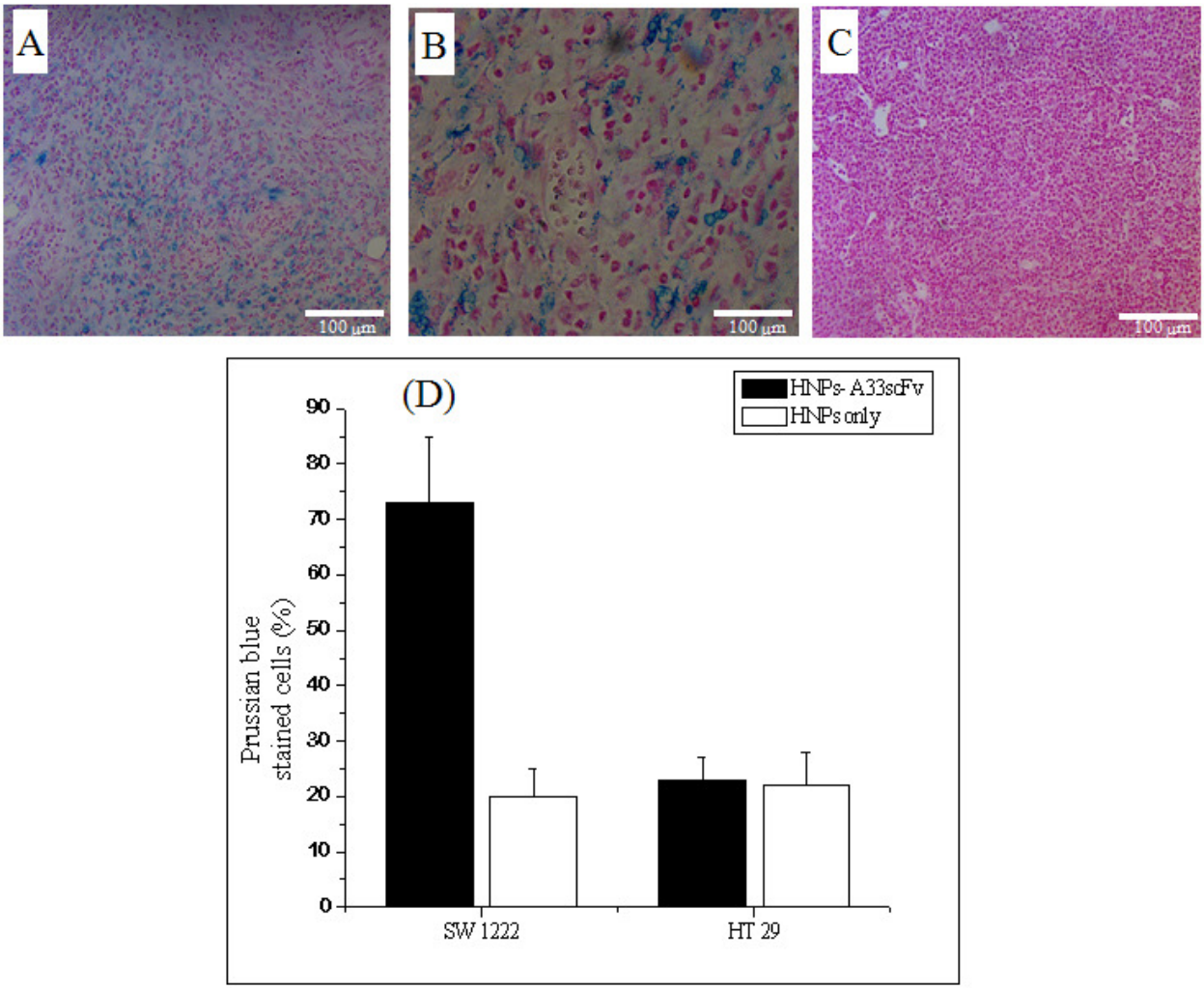

Figure 4-5: Perl's Prussian blue staining and histological analyses of SW1222 tumor xenografts before and after particle-injection. (a) Tissues after injection and localization of HNPs, blue stains signify the presence of HNPs-scFv resulting from active targeting localization (b) Tissues harvested after photothermal therapy, showing the presence of HNPs at reducing levels of iron due to clearance; (c) tissue harvested before systemic injection indicating the absence of blue stain or HNPs in tissue (control); (d) Comparative amounts of iron in the targeted tumor xenografts of SW1222 and HT29 cells as quantified by ImageJ (NIH). Scale bar 100 µm.

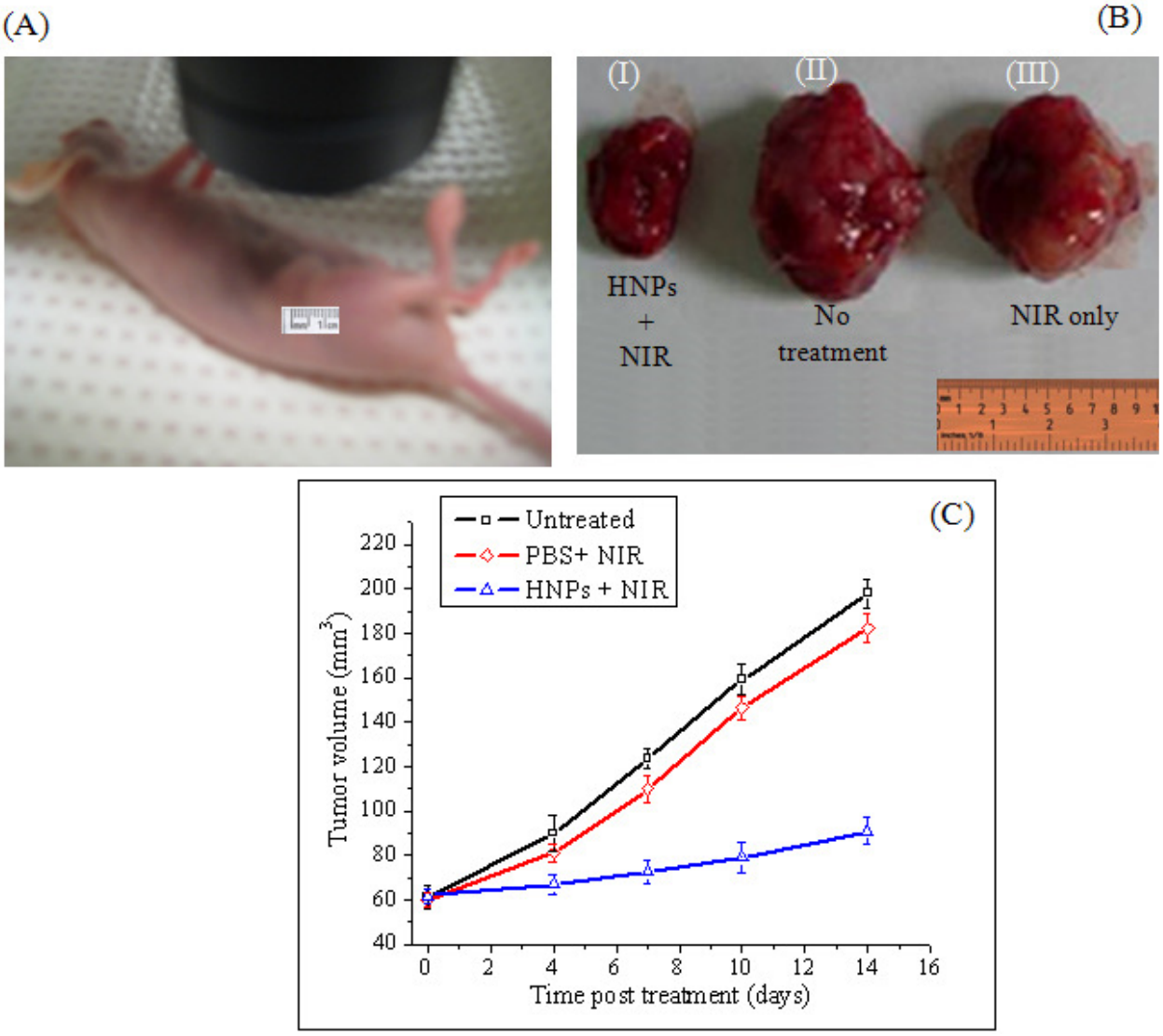

Figure 4-6 : *In vivo* photothermal therapy application and effect of 808-nm laser on subcutaneous tumor xenografts. (a) Tumors on hind flanks treated with 808-nm laser after swapping with index matching polyethylene glycol solution; (b) representative tumor sizes harvested after 14 days post-irradiation of mice treated with HNPs plus NIR laser (group II), or untreated control (group II), or PBS plus NIR laser (group III); (c) time-dependent tumor growth curves of SW1222 tumor cell xenografts. The tumor size was calculated as $ab^2/2$ (a represents the longer dimension and b represents the shorter dimension of the tumor) where they were measured 24 hr after irradiation and continued for the duration of the therapy. The results are presented as the arithmetic means with standard deviations of tumor volumes in each group (n = 3). Error bars represent 95% confidence level (n = 3 mice per group). Asterisks indicate statistical significance relative to the untreated control (p = 0.006). Only HNPs plus NIR treated group (I) shows significant suppression of tumor growth compared with other experimental groups (n = 3). , $p < 0.05$, one-way ANOVA.

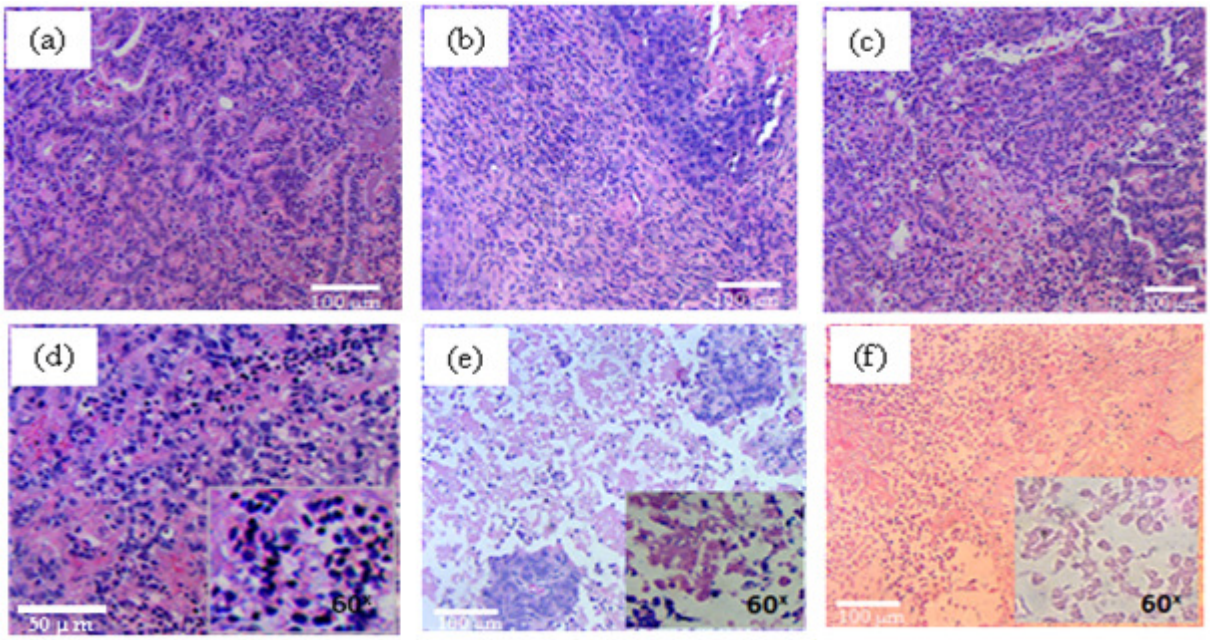

Figure 4-7: Histological assessment of tumor tissues before and after photothermal therapy showing cell damage by H&E staining. (a) tumor harvested before therapy (day 1), showing healthy cells with well-defined nucleus, cytoplasm and extracellular matrix; (b) tissues from control group II (untreated at end of therapy), showing healthy cells with apoptotic/necrotic cells possibly resulting from hypoxia; (c) xenograft samples from group I (HNPs plus laser) after third round of therapy, showing nucleus shrinkage and slight corruption of extracellular matrix; (d) group I tumors after fourth treatment that show necrotized cells, initial stage of cytoplasmic acidophilia and nucleus shrinkage; (e) group I after seven rounds of therapy showing over 65% necrotic cells as compared to untreated group, corruption of extracellular matrix and cytoplasmic acidophilia; (f) tissues from intratumoral plus laser treatment (two rounds), showing almost total cell necrosis, pyknosis, and karyolysis with bundle-like structure left behind. Scale bar: 100 μm.

REFERENCES

1. Wust, P.; Hildebrandt, B.; Sreenivasa, G.; Rau, B.; Gellermann, J.; Riess, H.; Felix, R.; Schlag, P. M., Hyperthermia in combined treatment of cancer. *The Lancet Oncology* **2002,** 3, (8), 487-497.

2. Terentyuk, G. S.; Maslyakova, G. N.; Suleymanova, L. V.; Khlebtsov, N. G.; Khlebtsov, B. N.; Akchurin, G. G.; Maksimova, I. L.; Tuchin, V. V., Laser-induced tissue hyperthermia mediated by gold nanoparticles: toward cancer phototherapy. *J. Biomed. Opt.* **2009,** 14, (2), 021016-9.

3. Link, S.; El-Sayed, M. A., Optical Properties and Ultrafast Dynamics of Metallic Nanocrystals. *Ann. Rev. Phys. Chem.* **2003,** 54, (1), 331-366.

4. Kim, J.; Park, S.; Lee, J. E.; Jin, S. M.; Lee, J. H.; Lee, I. S.; Yang, I.; Kim, J.-S.; Kim, S. K.; Hyeon, T., Designed Fabrication of Multifunctional Magnetic Gold Nanoshells and their Application to Magnetic Resonance Imaging and Photothermal Therapy. *Angew. Chem Int.* **2006,** 45, 7754-7758.

5. Vergoni, A. V.; Tosi, G.; Tacchi, R.; Vandelli, M. A.; Bertolini, A.; Costantino, L., Nanoparticles as drug delivery agents specific for CNS: in vivo biodistribution. *Nanomedicine: Nanotechnology, Biology and Medicine* **2009,** 5, (4), 369-377.

6. Chen, J.; Wang, D.; Jiefeng, X.; Au, L.; Siekkinen, A.; Warsen, A.; Li, Z.-Y.; Zhang, H.; Xia, Y.; Li, X., Immuno Gold Nanocages with Tailored Optical Properties for Targeted Photothermal Destruction of Cancer Cells. *Nano Lett.* **2007,** 5, 1318-1322.

7. Kuo, W. S.; Wu, C. M.; Yang, Z. S.; Chen, S. Y.; Chen, C. Y.; Huang, W. M.; Sun, C. K.; Yeh, C. S., Biocompatible bacteria@Au composites for application in the photothermal destruction of cancer cells. *Chem. Commun.* **2008**, 4430-32.

8. Kam, N. W.; O'Connell, M.; Wisdom, J. A.; Dai, H., Carbon nanotubes as multifunctional biological transporters and near-infrared agents for selective cancer cell destruction. *Proc. Natl. Acad. Sci. USA* **2005**.

9. O'Neal, D. P.; Hirsch, L. R.; Halas, N. J.; Payne, J. D.; West, J. L., Photo-thermal tumor ablation in mice using near-infrared absorbing nanoparticles. *Cancer Lett.* **2004,** 209, 171-6.

10. Wu, P.-C.; Su, C.-H.; Cheng, F.-Y.; Weng, J.-C.; Chen, J.-H.; Tsai, T.-L.; Yeh, C.-S.; Su, W.-C.; Hwu, J. R.; Tzeng, Y.; Shieh, D.-B., Modularly Assembled Magnetite Nanoparticles Enhance in Vivo Targeting for Magnetic Resonance Cancer Imaging. *Bioconjug. Chem.* **2008,** 19, (10), 1972-1979.

11. Jolesz, F. A.; Hynynen, K., Magnetic resonance image guided focused ultrasound surgery. *Cancer J.* **2002,** 8, S100-S112.

12. McCarthy, J. R.; Weissleder, R., Multifunctional magnetic nanoparticles for targeted imaging and therapy. *Adv. Drug Del. Rev.* **2008,** 60, (11), 1241-1251.

13. Maeng, J. H.; Lee, D.-H.; Jung, K. H.; Bae, Y.-H.; Park, I.-S.; Jeong, S.; Jeon, Y.-S.; Shim, C.-K.; Kim, W.; Kim, J.; Lee, J.; Lee, Y.-M.; Kim, J.-H.; Kim, W.-H.; Hong, S.-S., Multifunctional doxorubicin loaded superparamagnetic iron oxide nanoparticles for chemotherapy and magnetic resonance imaging in liver cancer. *Biomaterials* **2010,** 31, (18), 4995-5006.

14. Wang, L.; Bao, J.; Li, Y.; Huang, Y., Multifunctional Nanoparticles Displaying Magnetization anfd Near-IR absorption. *Angew. Chem. Int.* **2008,** 120, (13), 2473-76.

15. Park, H.; Yang, J.; Seo, S.; Kim, K.; Suh, J.; Kim, D.; Haam, S.; Yoo, K.-H., Multifunctional Nanoparticles for photothermally controlled drug delivery and magnetic resonance Imaging Enhancement. *Angew. Chem. Int.* **2008,** 4, (2), 192-96.

16. Park, J. H.; Maltzahn, G. V.; Sangeeta, B. H.; Ruoslahti, E.; Bhatia, S. N.; Sailor, M. J., Micellar Hybrid Nanoparticles for Simultaneous Magnetofluorescent Imaging and Drug Delivery. *Angew. Chem. Int. Ed.* **2008,** 47, 1-6.

17. Drake, P.; Cho, H. J.; Shih, P. S.; Kao, C.-H.; Lee, K.-F.; Kuo, C. H., Gd-doped iron-oxide nanoparticles for tumour therapy via magnetic field hyperthermia. *J. Mater. Chem.* **2007,** 17, 4914-4918.

18. Wang, L.; Park, H. Y.; Lim, S. I.; Schadt, M. J.; Mott, D.; Luo, J.; Wang, X.; Zhong, C., Core@Shell nanomaterials: gold-coates magnetic nanoparticles. *J Mater. Chem.* **2008,** 18, 2629-35.

19. Wang, L.; Maye, M. W.; Fan, Q.; Rendeng, Q.; Zhong, C., Iron oxide-gold core-shell nanoparticles and thin film assembly. *J Mater Chem* **2005,** 15, 1821-32.

20. Josephson, L.; Kircher, M. F.; Mahmood, U.; Tang, Y.; Weissleder, R., Near-Infrared Fluorescent Nanoparticles as Combined MR/Optical Imaging Probes. *Bioconjug. Chem.* **2002,** 13, (3), 554-560.

21. Medorova, Z.; Pham, W.; Kim, Y.; Dai, G.; Moore, A., In vivo imaging of tumor response to therapy using a dual-modality imaging strategy. *Int. J. Cancer* **2006,** 118, 2796-802.

22. Veiseh, O.; Sun, C.; Gunn, J.; Kohler, N.; Gabikian, P.; Lee, D.; Bhattarai, N.; Ellenbogen, R.; Sze, R.; Hallahan, A.; Olson, J.; Zhang, M., Optical and MRI Multifunctional Nanoprobe for Targeting Gliomas. *Nano Lett.* **2005,** 5, (6), 1003-1008.

23. Khemtong, C.; Kessinger, C. W.; Ren, J.; Bey, E. A.; Yang, S.; Guthi, J. S.; Boothman, D. A.; Gao, J., In vivo off-Resonance Saturation Magnetic Resonance Imaging of Targeted Superparamagnetic Nanoparticles. *Cancer Res.* **2009,** 69, (4), 1651-55.

24. Prasad, N. K.; Rathinasamy, K.; Panda, D.; Bahadur, D., Mechanism of cell death induced by magnetic hyperthermia with nanoparticles of Mnx Fe2O3 synthesized by a single step process. *J. Mater. Chem.* **2007,** 17, 5042-5051.

25. Kirui, D.; Rey, D.; Batt, C., Gold hybrid nanoparticles for targeted phototherapy and cancer imaging. *Nanotechnology* **2010,** 21, (10), 105105.

26. Deckert, P. M.; Renner, C.; Cohen, L. S.; Jungbluth, A.; Ritter, G.; Welt, S., A33scFv-cytosine deaminase:a recombinant protein construct for antibody-directed enzyme-pro-drug therapy. *J. Cancer* **2003,** 88, 937-939.

27. Ackerman, M.; Chalouni, C.; Schmidt, M.; Raman, V.; Ritter, G.; Old, L.; Mellman, I.; Wittrup, K., A33 antigen displays persistent surface expression. *Cancer Immunology, Immunotherapy* **2008,** 57, (7), 1017-1027.

28. Damasceno, L.; et al., An optimized fermentation process for high-level production of a single-chain antibody fragment in Pichia pastoris. *Protein Express. Purif.* **2004,** 37, (1), 18.

29. Daghighian, F.; Barendswaard, E.; Welt, S.; Humm, J.; Scott, A.; Willingham, M. C.; McGuffie, E.; Old, L. J.; Larson, S. M., Enhancement of Radiation Dose to the Nucleus by Vesicular Internalization of Iodine-125-Labeled A33 Monoclonal Antibody. *J Nucl Med* **1996,** 37, (6), 1052-1057.

30. Damasceno, L.; Pla, I.; Chang, H. J.; Cohen, L.; Ritter, G.; Old, L. J.; Batt, C. A., An optimized fermentation process for high-level production of a single-chain antibody fragment in Pichia pastoris. *Protein Express. Purif.* **2004,** 37, 18-26.

31. Yu, H.; Chen, M.; Rice, P. M.; Wang, S. X.; White, W. R. L.; Sun, S., Dumbbell-like Bifunctional Au-Fe3O4 Nanoparticles. *Nano Lett.* **2005,** 5, (2), 379-382.

32. Hildebrandt, B. W., P.; Ahlers, O.; Dieing, A.; Sreenivasa, G.; Kerner, T.; Felix R.; Riess, H., The cellular and molecular basis of hyperthermia. *Crit. Rev. Oncology/Hematology* **2002,** 43, 33-56.

33. Kirui, D. K.; Krishnan, S.; Strickland, A. D.; Batt, C. A., PAA-Derived Gold Nanorods for Cellular Targeting and Photothermal Therapy. *Macromol. Biosci.* **2011**, n/a-n/a.

34. Choi, W. I.; Kim, J.-Y.; Kang, C.; Byeon, C. C.; Kim, Y. H.; Tae, G., Tumor Regression In Vivo by Photothermal Therapy Based on Gold-Nanorod-Loaded, Functional Nanocarriers. *ACS Nano* **2011,** 5, (3), 1995-2003.

35. Moon, H. K.; Lee, S. H.; Choi, H. C., In Vivo Near-Infrared Mediated Tumor Destruction by Photothermal Effect of Carbon Nanotubes. *ACS Nano* **2009,** 3, (11), 3707-3713.

36. Yang, K.; Zhang, S.; Zhang, G.; Sun, X.; Lee, S.-T.; Liu, Z., Graphene in Mice: Ultrahigh In Vivo Tumor Uptake and Efficient Photothermal Therapy. *Nano Lett.* **2010,** 10, (9), 3318-3323.

37. Maeda, H., Tumor-Selective Delivery of Macromolecular Drugs via the EPR Effect: Background and Future Prospects. *Bioconjug. Chem.* **2010,** 21, (5), 797-802.

38. Wang, M.; Thanou, M., Targeting nanoparticles to cancer. *Pharmacol. Res.* **2010,** 62, (2), 90-99.

39. Goutayer, M.; Dufort, S.; Josserand, V.; Royère, A.; Heinrich, E.; Vinet, F.; Bibette, J.; Coll, J.-L.; Texier, I., Tumor targeting of functionalized lipid nanoparticles: Assessment by in vivo fluorescence imaging. *Eur. J. Pharm. Biopharm.* **2010,** 75, (2), 137-147.

40. Anderson, R. R.; Parrish, J. A., Selective photothermolysis: precise microsurgery by selective absorption of pulsed radiation. *Science* **1983,** 220, (4596), 524-527.

41. Yang, W.-L.; Nair, D.; Makizumi, R.; Gallos, G.; Ye, X.; Sharma, R.; Ravikumar, T., Heat Shock Protein 70 Is Induced in Mouse Human Colon Tumor Xenografts After Sublethal Radiofrequency Ablation. *Annals of Surgical Oncology* **2004,** 11, (4), 399-406.

42. Thrall, D. E.; LaRue, S. M.; Yu, D.; Samulski, T.; Sanders, L.; Case, B.; Rosner, G.; Azuma, C.; Poulson, J.; Pruitt, A. F.; Stanley, W.; Hauck, M. L.; Williams, L.; Hess, P.; Dewhirst, M. W., Thermal Dose Is Related to Duration of Local Control in Canine Sarcomas Treated with Thermoradiotherapy. *Clin. Cancer Res.* **2005,** 11, (14), 5206-5214.

43. Engin, K., Biological rationale and clinical experience with hyperthermia. *Control. Clin. Tri.* **1996,** 17, (4), 316-342.

Chapter 5

Future Outlook

In summary, the thesis has demonstrated rational design and utility of iron oxide and gold nanostructures for therapy and diagnostics (theranostic) applications. We have shown the rational design of hybrid nanoparticles with both strong magnetic as well as optical properties that can be used to make a single device with multiple applications. The most upstream research effort in this thesis, thus far, touched on investigation that ensured that the molecular targeting capabilities of colorectal cancer cells using A33 single chain antibody. Cell culture experiments were initially used to validate A33scFv targeting capabilities which were followed by *in vitro* demonstration of photothermal therapy (**Chapter 2**). More recently, we have also shown effective photothermal treatment in nude mice using subcutaneously grown colorectal cancer xenografts following successful particle localization after systemic injection (**Chapter 4**). While these are significant results by their own, here are some further thoughts/ideas that would make this novel technology viable for future translational research. In **Chapter 4**, particle localization in antigen-expressing SW 1222 xenograft tumors was confirmed by live-animal fluorescence imaging and by histological assessment of stained tissue samples after euthanizing the animal and tumor resection. To fully understand the fate of particles and the potential *in vivo* toxicity, more studies are needed.

To understand the fate of particles *in vivo*, bio-distribution studies are needed to investigate the time-dependent particle duration and half-life in blood and in the various organs. This study would be critical in addressing dosage and toxicity issues associated with the use of HNPs for therapy and diagnostics. In a typical experiment, xenograft mice tumors that are systemically injected with HNPs are sacrificed and the tissues samples of the following organs: kidney, liver, and bladder, spleen, and tumor samples are recovered and prepared for analyses. The organs are digested and appropriately prepared in order to extract embedded nanoparticles

whose concentration may be subsequently be determined by inductively coupled plasma mass spectrometry (ICP Mass Spec). For example *Vergoni al* and coworkers [1] determined the concentration of nanoparticles following targeted and systemic injection of nanoparticles in murine models.Similar preparatory protocol would be used to characterize the bio-distribution properties of HNPs. One major drawback to using ICP Mass Spec as analytical method to determine the amount of HNPs is that physiological in *vivo* systems (e.g. mice) already have high iron (Iron-56) content, the most naturally-occuring abundant iron isotope. Consequently, the detection of localized or systemically-injected HNPs would be made more difficult because of a larger background noise from the endogenous Iron-56 already in blood and would introduce experimental error to the bio-distribution experiments. This problem would be circumvented by synthesizing HNPs from a precursor of Iron-58, which is one of least abundant isotope also absent in the *in vivo* system. The quantification of Iron-58 isotope recovered from blood samples or tissue samples can be performed using ICP-Mass Spec with detection limits as low as part per billion (ppb).

Another facile method that can used to study *in vivo* bio-distribution is positron emission tomography (PET) nuclear imaging technique. Both the hybrid particles as well as gold nanorods possess peripheral carboxyl functional groups that can be used to attach radiolabeled with a positron-emitting tracer. Similar PET-based methods have been used to study bio-distribution of quantum dots (QDs) in mice where dextran-coated QDs were labeled with ^{64}Cu and subsequently used for *in vivo* PET imaging [2]. Other nuclear radiolabels such as Yttrium-90 and Indium-111 labeled biomolecules have been frequently used for various bio-distribution and bio-stability studies [3-5]. For instance, McDevitt *et al.* recently reported on the preparation of soluble Yttrium-86-labeled carbon nanotubes (CNTs) and subsequent PET imaging [6]. The ^{86}Y-

CNT constructs were synthesized from amine-functionalized, water-soluble CNT by covalently attaching multiple choices of DOTA chelates and then radiolabeling with the positron-emitting metal-ion, yttrium-86. Using similar preparatory protocol, the carboxyl-terminated nanoparticles can be attached the PET tracers and used to study biodistribution *in vivo*.

We have reported our work in the rational design and the eventual *in vivo* hybrid nanoparticles (HNPs) application in **Chapters 2** and **4**. In **Chapter 3**, we have begun the rational design of gold nanorods for potential *in vivo* photothermal therapy. The one advantage of moving towards the use of gold nanorods for photothermal therapy is their strong near-IR absorption which would be ideal for *in vivo* phototherapy application. We have shown effective photothermal therapy in targeted colorectal carcinoma cells *in vitro*. Going forward, establishing xenograft models that can be used to validate their application in vivo is a rational next step. Once, in vivo localization as well as therapy application is validated, an interesting course of experimentation is making hybrid gold nanorods-iron oxide nanoparticles for potential theranostic applications. In this work, gold nanorods can be designed to allow the attachment of smaller iron oxide nanoparticles, resulting in nanorods coated with small beads of iron oxide, forming multifunctional platforms. These hybrid gold and iron nanostructures would be more efficient in photothermal therapy uses (higher NIR absorption) as well as stronger MR capabilities (owing to aggregation of iron oxide NPs around the gold NR structure). In vivo particles localization as well as biodistribution studies can be performed in nude mice where the gold nanorod-iron oxide attached to targeting agents and/or radioisotopes used to study effects effects of targeting and the associated cytotoxicity.

Iron oxide nanoparticles and gold nanostructures (NPs and NRs) have been implicated for a myriad of other biomedical applications. Beyond the scope of what have been discussed above, the nanostructures hold great potential for research and applications in the following areas

I. Particle-assisted heat induced therapeutic release

We have demonstrated the use of hybrid nanoparticles as well as the use of gold nanorods for laser-assisted for photothermal therapy. These nanostructures act as local heating agents where near-IR irradiation (suitable for *in vivo* penetration) is used to induce cell death by hyperthermia. Similar concept could be extended to the use of these nanostructures as a means for controllable or time-dependent drug release. In this case, temperature release would result in the degradation of temperature-sensitive drug capsule, resulting in controlled release of its content. For example, a recent study showed the use of phothermal laser irradiation to controllably release a model drug (rhodamine) from a temperature-sensitive poly (lactic-co-glycolic acid) (PLGA). The polymer was conjugated to hybrid nanoparticles (Manganese/gold nanoparticles) and used for photothermal-triggered drug release as well for non-invasive MR imaging [7]. In much the same way, it is envisioned that the hybrid nanoparticles (HNPs) we have reported in this thesis can be conjugated to polymeric drug delivery system that disintegrates at higher temperature. Once the hybrid nanoparticles have been targeted to select cells, laser irradiation can be used as an external remote to trigger drug release.

II. Magnetic-driven Therapeutic Delivery and release

Another potential application of hybrid nanoparticles is for externally-guided therapeutic delivery to treatment of disease such as lung cancer. We have demonstrated the superparamagnetic character of HNPs (**Chapters 2** and **3**) and this means that they respond to a magnetic field. Superparamagnetic nanoparticles have recently been suggested and incorporated into drug delivery systems (DDS) to make 'nanomagnetosols' that can be remotely-guided using strong magnetic field [8]. For example, this DSS have become valuable tool in the delivery of aerosolized therapeutics. One example where this strategy has become prevalent in the delivery of aerosol used to treat lung cancer. In this particular application, aerosols encapsulated along with magnetic nanoparticles are targeted by an external magnetic before they are releasing its content where the DSS are disintegrated by heating with alternating magnetic field. We envision that the hybrid particles reported in this thesis may also form valuable tool for a similar therapeutic application. Again, using the hybrid particles provides an added advantage because they can also be used for diagnosis or imaging (MRI or CT imaging) following therapeutic delivery.

III. Magnetic thermotherapy and Imaging applications

While we have reported the use of hybrid nanoparticles for multimodal laser-assisted cell therapy and as well for non-invasive MR imaging, these particles can be adapted for applications using other therapy and imaging modalities. Depending on the availability of the therapy and imaging modality, the gold- iron oxide hybrid nanoparticles can potentially be used to induce cell death using external magnetic field. In this case, iron oxide nanoparticle is used to generate heat using external magnetic fields [9]. The localized temperature causes hyperthermia and the

leads to cell death. Magnetic thermotherapy using iron oxide nanoparticles has been investigated for the treatment of prostate cancer [10], multiple sclerosis [9], for multimodal treatment of multiforme glioblastoma [11]. Once therapy applications are completed, the particles can be used for non-invasive visualization or MR imaging to monitor the efficacy of therapy applications. We envisioned that the hybrid nanoparticles, due to their strong magnetic properties, may be adapted for uses in thermotherapy applications. It may involve modifying the particle corona to allow attachment of targeting moieties that would increase cell-specific selectivity.

IV. Thermotherapy and X-ray (CT) Imaging Applications

The other imaging modality that has gained more interest for biomedical imaging is X-ray based computed tomography (CT) imaging. CT imaging is one of the most useful diagnostic tools in hospitals today in terms of availability, efficiency, and cost. Hybrid nanoparticles are partly composed of gold nanoparticle cores which are an ideal material for CT contrast agents because they possess high electron density. In cases where MR imaging modality is too costly, the hybrid nanoparticles can be alternatively used as CT imaging agents due to presence of gold nanoparticle core. CT distinguishes between different tissues based on the fact that different tissues provide different degrees of X-ray attenuation, where the attenuation coefficient is determined by the atomic number and electron density of the tissue; the higher the atomic number and electron density, the higher the attenuation coefficient. Currently, it is not molecular imaging modality since relevant targeted and molecular specific contrast agents have yet to be approved for clinical use. Present CT contrast agents are predominantly based on iodine containing molecules, which are effective in absorbing X-rays; however they are nonspecific

because they cannot be conjugated to biological components or cancer markers and allow only very short imaging times due to rapid clearance by the kidneys [12].

V. Tissue regeneration Applications

Due to the magnetic properties, hybrid nanoparticles can potentially be used for tissue regeneration applications. Magnetic-based nanoparticles have garnered as potential interest materials to enhance tissue regeneration of various types of cells. For instance, iron oxide nanoparticles have been investigation for the treatment of osteoporosis which caused by reduction of bone mass and increases risk of bone fractures. Osteoporosis affects approximately 44 million Americans and osteoporosis-related bone fracture cost over $19 million yearly [13]. As a novel therapy method, recent research efforts have involved using magnetic nanoparticles coated with hydroxyapatite (HA) and to concentrate/ localize HA which is essential for bone regeneration [14]. The magnetic NPs are used for magnetic-driven concentration in which an external magnetic field is placed in close proximity to the osteoporositic tissue.

VI. Particle-assisted Photodynamic therapy

Nanostructures such as hybrid nanoparticles (HNPs) can also be used for photodynamic therapy (PDT) of diseased cells or tissues. Photodynamic therapy (PDT) is a method of clinical treatment whereby diseased cells and tissues are destroyed by a combination of light and special drugs called photosensitizers (PS). Additionally, the presence of adequate molecular oxygen in the tissue is also required [15]. In this thesis, we have demonstrated the use of both iron oxide-gold

nanoparticles for laser assisted photothermal therapy in which hybrid particles act as local heating agents. In future research, the use particles may be extended to include uses for a novel therapy application - photodynamic therapy application. Photodynamic therapy [16].

REFERENCES

1. Vergoni, A. V.; Tosi, G.; Tacchi, R.; Vandelli, M. A.; Bertolini, A.; Costantino, L., Nanoparticles as drug delivery agents specific for CNS: in vivo biodistribution. *Nanomedicine: Nanotech. Biol. Med.* **2009,** 5, (4), 369-377.

2. Tu, C.; Ma, X.; House, A.; Kauzlarich, S. M.; Louie, A. Y., PET Imaging and Biodistribution of Silicon Quantum Dots in Mice. *ACS Med. Chem. Lett.* **2011,** 2, (4), 285-288.

3. Liu, S.; Pietryka, J.; Ellars, C. E.; Edwards, D. S., Comparison of Yttrium and Indium Complexes of DOTA-BA and DOTA-MBA: Models for 90Y- and 111In-Labeled DOTA-Biomolecule Conjugates. *Bioconjug. Chem.* **2002,** 13, (4), 902-913.

4. Giblin, M. F.; Gali, H.; Sieckman, G. L.; Owen, N. K.; Hoffman, T. J.; Forte, L. R.; Volkert, W. A., In Vitro and in Vivo Comparison of Human Escherichia coli Heat-Stable Peptide Analogues Incorporating the 111In-DOTA Group and Distinct Linker Moieties. *Bioconjug. Chem.* **2004,** 15, (4), 872-880.

5. Tsai, S. W.; Li, L.; Williams, L. E.; Anderson, A. L.; Raubitschek, A. A.; Shively, J. E., Metabolism and Renal Clearance of 111In-Labeled DOTA-Conjugated Antibody Fragments. *Bioconjug. Chem.* **2001,** 12, (2), 264-270.

6. McDevitt, M. R.; Chattopadhyay, D.; Jaggi, J. S.; Finn, R. D.; Zanzonico, P. B.; Villa, C.; Rey, D.; Mendenhall, J.; Batt, C. A.; Njardarson, J. T.; Scheinberg, D. A., PET Imaging of Soluble Yttrium-86-Labeled Carbon Nanotubes in Mice. *PLoS ONE* **2007,** 2, (9), e907.

7. Park, H.; Yang, J.; Seo, S.; Kim, K.; Suh, J.; Kim, D.; Haam, S.; Yoo, K.-H., Multifunctional Nanoparticles for Photothermally Controlled Drug Delivery and Magnetic Resonance Imaging Enhancement. *Small* **2008,** 4, (2), 192-196.

8. Plank, C., Nanomagnetosols: magnetism opens up new perspectives for targeted aerosol delivery to the lung. *Trends Biotech.* **2008,** 26, (2), 59-63.

9. Mahmoudi, M.; Sahraian, M. A.; Shokrgozar, M. A.; Laurent, S., Superparamagnetic Iron Oxide Nanoparticles: Promises for Diagnosis and Treatment of Multiple Sclerosis. *ACS Chem. Neurosci.* **2011,** 2, (3), 118-140.

10. Johannsen, M.; Gneveckow, U.; Thiesen, B.; Taymoorian, K.; Cho, C. H.; Waldöfner, N.; Scholz, R.; Jordan, A.; Loening, S. A.; Wust, P., Thermotherapy of Prostate Cancer Using Magnetic Nanoparticles: Feasibility, Imaging, and Three-Dimensional Temperature Distribution. *Eur. Urol.* **2007,** 52, (6), 1653-1662.

11. van Landeghem, F. K. H.; Maier-Hauff, K.; Jordan, A.; Hoffmann, K.-T.; Gneveckow, U.; Scholz, R.; Thiesen, B.; Brück, W.; von Deimling, A., Post-mortem studies in glioblastoma patients treated with thermotherapy using magnetic nanoparticles. *Biomaterials* **2009,** 30, (1), 52-57.

12. Popovtzer, R.; Agrawal, A.; Kotov, N. A.; Popovtzer, A.; Balter, J.; Carey, T. E.; Kopelman, R., Targeted Gold Nanoparticles Enable Molecular CT Imaging of Cancer. *Nano Lett.* **2008,** 8, (12), 4593-4596.

13. National_Osteoporosis_Foundation, http://www.nof.org/home. In 2011.

14. Tran, N.; Webster, T. J., Increased osteoblast functions in the presence of hydroxyapatite-coated iron oxide nanoparticles. *Acta Biomaterialia* **2011,** 7, (3), 1298-1306.

15. Triesscheijn, M.; Baas, P.; Schellens, J. H.; Stewart, F. A., Photodynamic Therapy in Oncology. *Radiation Oncology* **2006,** 11, (9), 1034-1044.

16. Chatterjee, D. K.; Fong, L. S.; Zhang, Y., Nanoparticles in photodynamic therapy: An emerging paradigm. *Adv. Drug Del. Rev.* **2008,** 60, (15), 1627-1637.

APPENDIX 1

ADDITIONAL MOLECULAR STRUCTURES AND TEM MICROGRAPHS

A.1. Molecular Structures of molecules for conjugation

In order to make water-soluble nanoparticles that are suitable for in *vivo* applications, we have used functionalized poly (glycol ethylene) PEG phospholipids, which are amphiphilic in nature, to coat oleic acid-stabilized nanoparticles. The formation of these water-soluble particles involves hydrophobic-hydrophobic interaction between the oleic acid stabilizing the particle and the phospholipid moiety on the amphiphilic copolymer which ultimately lead to the formation of the reverse-phase micelles, which contain the hydrophilic layer on the peripheral ends. In subsequent text, the molecular structures a number of PEG phospholipids and the formation of water-soluble will be shown. We prepared water-soluble nanoparticles by reverse-phase micelle formation using PEG-carboxyl phospholipid (DSPE-PEG (2000) carboxylic Acid, Avanti Polar lipids) as the capping agent. **Figure A1.1** shows a representative molecular structure of a PEG2000 phospholipid that was used to fabricate carboxyl-terminated nanoparticles described in

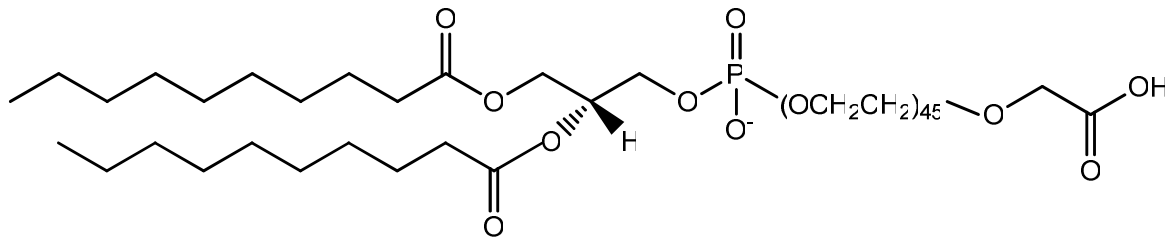

Figure A1.1: Functionalized PEG-carboxyl phosphopholipid (1,2-distearoyl-*sn*-glycero-3-phosphoethanolamine-N-[carboxy(polyethylene glycol)-2000] (ammonium salt)) . Molecular Formula $C_{134}H_{267}N_2O_{57}P$, Molecular weight = 2847.779 g mol^{-1}.

Chapters 2 and **4**. By using this functionalization strategy, the resulting particles were aggregate-free, stable, and contain amine-reactive moieties which allowed facile attachment of biomolecules through lysine residues.

There are other derivatives of functionalized phospholipids that are commercially available that allows facile attachment of molecules using simple chemistries. For example, we have used amine-terminated PEG phospholipid (DSPE-PEG (2000) Amine, Avanti lipids) instead of carboxyl-terminated to prepare aminated nanoparticles that are reactive to carboxylic acid moieties (**Figure A1.2**). Other functionalities that are available through Avanti lipids include: Maleimide, biotin, folate, and cyanur-terminated PEG phospholipids [1].

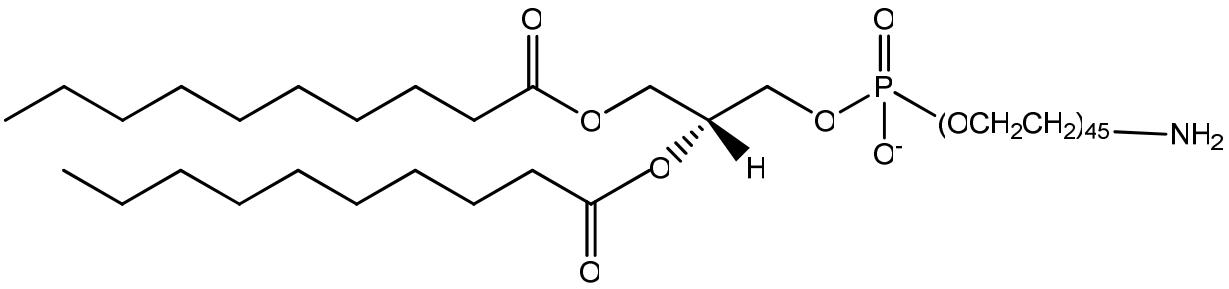

Figure A1.2: Functionalized PEG- amino phospholipid (1,2-distearoyl-*sn*-glycero-3-phosphoethanolamine -N-[amino(polyethylene glycol)-2000] (ammonium salt)). Molecular Formula $C_{132}H_{266}N_3O_{54}P$; Molecular weight 2788.790 g mol^{-1}.

The surface charge on the nanoparticles is one of the critical consideration that affect particle bio-distribution, cellular uptake, circulation, and blood half-life. To modulate the zeta potential or surface charge, we have used mPEG2000 (PEG 2000 PE, Avanti Lipids) as a component in mixture of functionalized phospholipids (**Figure A1.3**). Compared to PEG-COOH (negatively charge) and PEG-NH_2 (positively charged), mPEG2000 are neutrally charged and can be used as mixtures of functionalized phospholipids to control surface charge. For instance,

we have prepared particles with negligible surface charge by mixing mPEG and PEG-COOH phospholipids in the mol ratios of 7:3 where 1: 2.5 mol ratios of particles to total phospholipid concentrations were used.

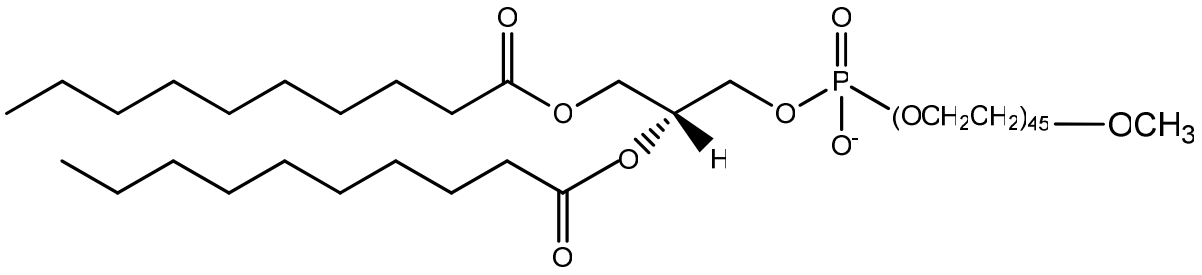

Figure A1.3: PEG phospholipid (1,2-distearoyl-*sn*-glycero-3-phosphoethanolamine-N-[amino(polyethylene glycol)-2000] (ammonium salt)). Molecular formula = $C_{133}H_{267}N_2O_{55}P$; Molecular weight = 2803.789 g mol^{-1}.

A.1.2. Reverse-phase Encapsulation of Oleic acid-coated Nanoparticles

The preparation of micelle-like particles using the phospholipids which has been described previously involved reverse-phase encapsulation of oleic acid-coated nanoparticles (suspended in chloroform). The particles were mixed with phospholipid PEG-COOH, and the mixture was sonicated, dried by evaporation, and eventually rehydrated in water.

Figure A1.4 shows schematic representation of this process. Additionally, the Figure depicts the interactions and forces that stabilize the particles and the peripheral functional groups that are used for the attachment of other molecules e.g. antibodies, fluorophores, and chemotherapeutics.

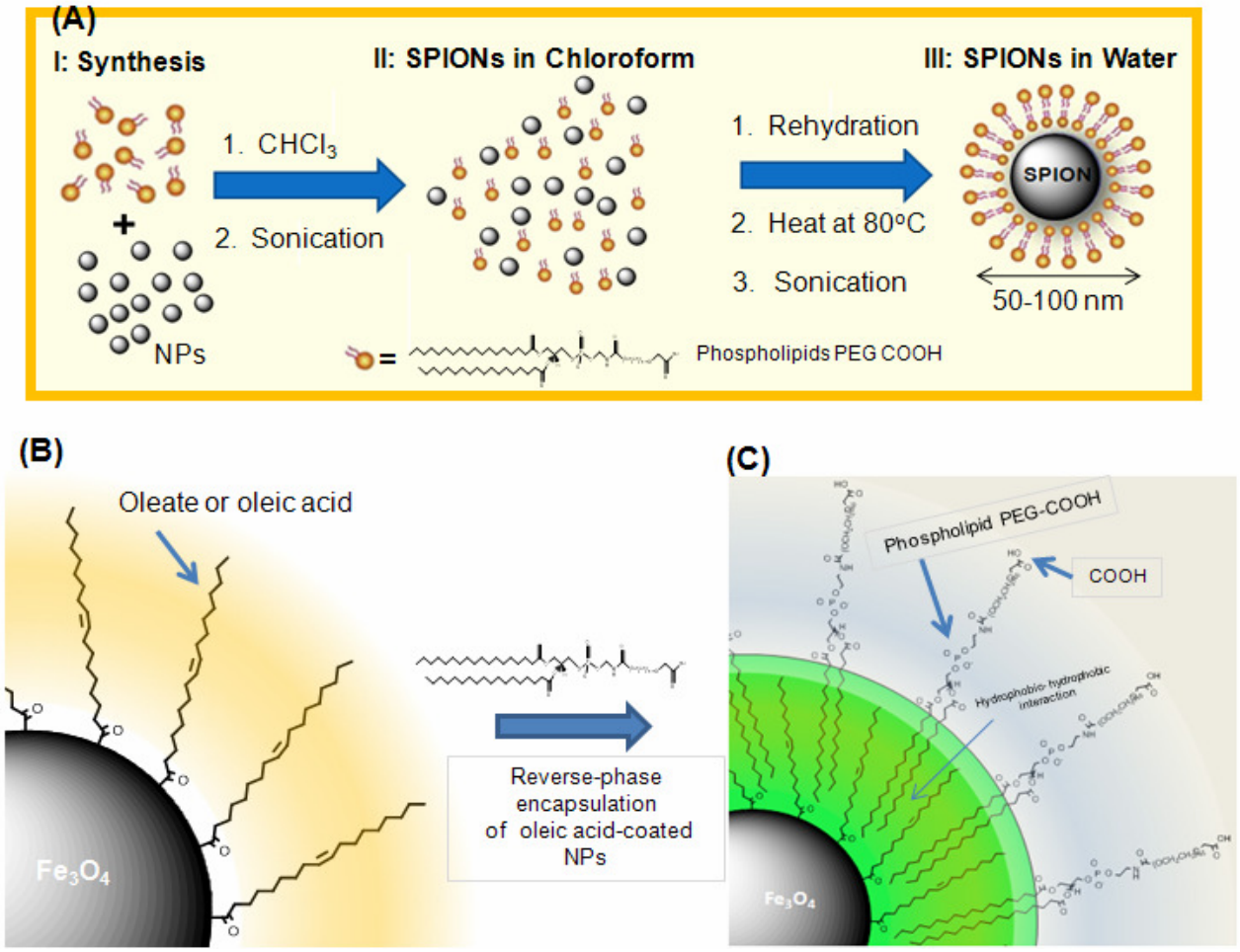

Figure A1.4: Encapsulation of nanoparticles using phospholipids PEG-COOH to form stabile, water soluble particles. (A) Schematic showing reverse-phase encapsulation of Fe3O4 in amphiphilic copolymers to form micelle-like particles, (B) Fe_3O_4-stabilized by oleic acid or oleate which form hydrophobic particles soluble in chloroform ($CHCl_3$), (C) Water-soluble NPs with carboxyl groups which allows facile attachment of biomolecules.

A.1.3. Transmission Electron Microscopy Images of Hybrid Nanoparticles

We have prepared hybrid Au-Fe_3O_4 nanoparticles for potential uses in therapy and imaging (theranostics) applications. We have demonstrated *in vitro* therapy and imaging applications (**Chapter 2**) and more recently we have further demonstrated their *in vivo* theranostic applications (**Chapter 4**). Below are TEM and high resolution (HR-TEM) that revealed the formation of peanut-shaped as well as dumbbell-like particles with dual magnetic as well as optical properties.

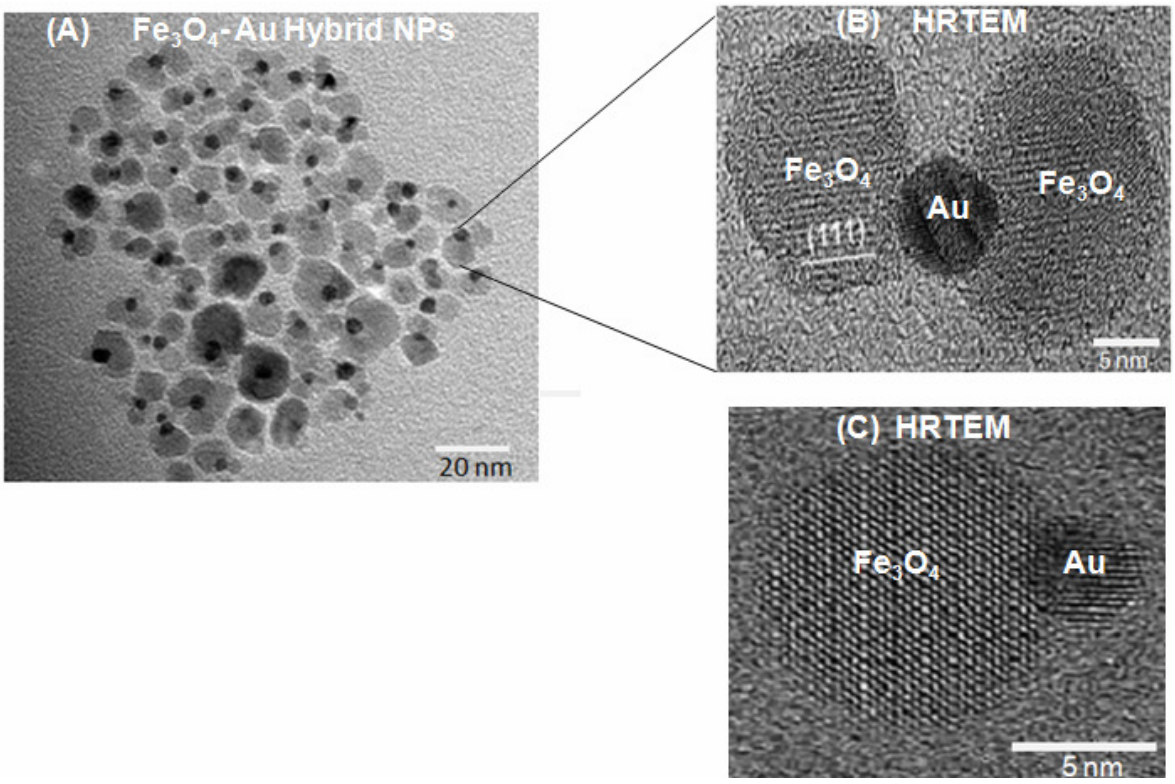

Figure A1.5: Transmission electron microscopy (TEM) images of dumbbell-like particles. Particles preparation was reported previously in Chapters 3 and 4. (A) TEM micrographs showing monodispersed Au-Fe_3O_4 NPs; (B), (C) High resolution(HR) TEM micrographs showing variations of Au: Fe_3O_4 ratios.

REFERENCES

1. Avanti Lipids http://avantilipids.com/index.php?option=com_content&view=article&id=145&Itemid=153, **2011.**